Università degli Studi di Napoli
"Federico II"

Scuola Politecnica e delle Scienze di Base

Dipartimento di Ingegneria Industriale

Tesi di Laurea in Ingegneria Aerospaziale

CLASSE DELLE LAUREE MAGISTRALI IN INGEGNERIA AEROSPAZIALE E ASTRONAUTICA (LM 20)

DESIGN EXPLORATION ON THE AERODYNAMICS AND STATIC STABILITY OF THE BLENDED WING BODY AIRCRAFT

Relatore
Prof. Fabrizio Nicolosi
Correlatore
Prof. Danilo Ciliberti

Candidato
Rocco Michele Pettorone
Matricola
M53000902

Anno Accademico 2020/2021

Acknowledgements

Un sentito ringraziamento al Prof. Fabrizio Nicolosi e Danilo Ciliberti, rispettivamente relatore e correlatore di questa tesi, grazie per le oppurtunità proposte, il vostro costante sostegno e la crescita umana e professionale.

Alla mia famiglia, mia madre e mio padre, che con il loro amore mi hanno sempre sostenuto e guidato, pure quando la mia insicurezza e le mie paure avevano creato una barriera quasi insormontabile. Tutto questo è anche merito vostro.

A Valerio, tu che nel percorso universitario e nella vita sei stato uno dei miei più grandi punti di riferimento.

A Olindo, che mi ha preso e accompagnato attraverso i momenti di più grande gioia e dolore della mia vita.

A Luigi, un fratello, il mio più grande braccio destro e colonna portante.

A Denise, che in così poco tempo si è riuscita a ritagliare uno spazio così importante nella mia vita.

Un sentito ringraziamento a tutti gli amici che non sono riuscito a lodare esplicitamente, avete tutti una parte importante del mio cuore.

Grazie anche a chi non c'è più nella mia vita, vi ringrazio per la persona che sono diventato.

Contents

List of Symbols

Symbol	Units (SI)	Description
Æ_{in}	-	Aspect Ratio of the inner wing part.
Æ_{out}	-	Aspect Ratio of the outer wing part.
b	m	Span.
BLD	-	Boundary-Layer Diverter.
BLI	-	Boundary-Layer Ingestion.
BWB	-	Blended Wing Body.
c	m	Chord.
C_{D}	-	Wing Drag coefficient.
C_{D_0}	-	Wing Parasite Drag coefficient.
C_{D_i}	-	Wing Induced Drag coefficient.
C_{D_w}	-	Wing Wave Drag coefficient.
CFD	-	Computational Fluid Dynamics.
C_{l}	-	Wing Lift section coefficient.
$C_{l_{max}}$	-	Maximum Wing Lift section coefficient.
C_{L}	-	Wing Lift coefficient.
$C_{L_{max}}$	-	Maximum Wing Lift coefficient.
C_{L_α}	deg^{-1}	Wing Lift Slope coefficient.
c_{root}	m	Chord of the root section.
$\bar{c}$	m	Mean Aerodynamic Chord.
$C_{\mathcal{M}_y}$	-	Pitching Moment Coefficient.
$C_{\mathcal{M}_0}$	-	Pitching Moment Coefficient at zero lift angle of attack.
$C_{\mathcal{M}_\alpha}$	deg^{-1}	Pitching Moment Coefficient gradient respect angle of attack.

Continued on next page

Continued from previous page

Symbol	Units (SI)	Description
$C_{\mathcal{N}_\beta}$	deg^{-1}	Yaw Moment Coefficient gradient respect angle of sideslip.
$C_{\mathcal{L}_\beta}$	deg^{-1}	Roll Moment Coefficient gradient respect angle of sideslip.
DOC	-	Direct Operative Cost.
DoE	-	Design of Experiments.
e	-	Oswald Number.
E	-	Aerodynamic Efficiency.
E_{MAX}	-	Maximum Aerodynamic Efficiency.
FEM	-	Finite Element Method.
h	m	Altitude.
$\left(\frac{L}{D}\right)$	-	Lift to Drag Ratio.
$\left(\frac{L}{D}\right)_{MAX}$	-	Maximum Lift to Drag Ratio.
LFC	-	Laminar Flow Control.
M	-	Flight Mach number.
mac	-	Mean Aerodynamic Chord.
M_{crit}	-	Critical Mach number.
M_{DD}	-	Drag Divergence Mach number.
MDO	-	Multidisciplinary Design Optimization.
PAX	-	Passengers.
Re	-	Reynolds number.
S	m^2	Wing Area.
S_{ref}	m^2	Reference Wing Area.
S_{strip}	m^2	Strip Wing Area.
S_{wet}	m^2	Wing wetted area.
SSM	-	Static Stability Margin.
TAW	-	Tube and Wing.
$(t/c)_{\text{root}}$	-	Thickness-to-chord ratio of the root section.

Continued on next page

Continued from previous page

Symbol	**Units (SI)**	**Description**
$(t/c)_{\text{kink}}$	-	Thickness-to-chord ratio of the kink section.
$(t/c)_{\text{max}}$	-	Maximum thickness-to-chord ratio .
$(t/c)_{\text{tip}}$	-	Thickness-to-chord ratio of the tip section.
$VELA$	-	Very Efficient Large Aircraft.
VLM	-	Vortex Lattice Method.
W_{OE}	kg	Operative Empty Weight.
X_{ac}	m	Location of the mean aerodynamic center along the chord.
X_{cg}	m	Location of The center of gravity along the chord.
Y_{SP}	m	Stall Path Section Location along the span.
α	deg	Angle of Attack.
α_0	deg	Zero lift angle of attack.
β	deg	Angle of Sideslip.
$\varepsilon_{\text{kink}}$	deg	Twist angle at the kink region.
ε_{tip}	deg	Twist angle at the tip.
η_{SP}	-	Normalized Stall Path Section Location along the span.
Γ	deg	Dihedral angle.
Γ_{n}	-	Horseshoe vortices strength.
κ_{A}	-	Airfoil technology factor.
λ_{in}	-	Inner taper ratio.
λ_{out}	-	Outer taper ratio.
$\Lambda_{\text{inner,LE}}$	deg	Inner sweep angle at leading edge.
Λ_{LE}	deg	Sweep angle at leading edge.
$\Lambda_{\text{outer,LE}}$	deg	Inner sweep angle at leading edge.

1

An Overview of the Blended Wing Body

1.1 Introduction to the BWB concept

1.1.1 General definitions

Since the birth of modern aviation, the most predominant aircraft concept has always been a *tube-and-wing* (TAW) configuration with a horizontal and vertical tail in order to obtain a certain degree of stability and control, meeting all the necessary safety requirements. As years go by, margins of improvement on this kind of configuration continuously restricted, while the prognosticated increase of the number of passengers, the rising fuel costs, and the necessity for a lower environmental footprint created a demand for more efficient aircraft and engines, as well as the need to utilize alternative fuels [1]. These challenges have sparked the interest of all the aviation industry in unconventional aircraft configurations. One of the concepts that has attracted a lot of attention is the *blended-wing body* aircraft (BWB).

The BWB configuration is characterized by an airfoil-shaped centre-body that integrates payload, propulsion, and control surfaces. Fuselage, seen as a *tube-like* body, is no longer a key part. In contrast, this configuration offers enough room in the wings to place passengers, cargo, fuel, and system units, which are distributed along the span. Greater aerodynamic efficiency can be traced as the most important

benefit, as the *airfoil-shaped body* allows the entire aircraft to generate lift and minimize drag due to a lower *wetted area*. This first benefit means a significant fuel-burn reduction that not only allows a reduction of the *Direct Operative Cost* (DOC) but also focuses on a reduction of noise and emission levels, an increasingly important topic of this century. The all-lifting design reduces the wing loading and improves the spanwise lift distribution, allowing a reduction in the empty weight W_{OE} of the aircraft. The smooth blended *wing-centre-body* intersection reduces the interference drag and the area-ruled shape of the BWB reduces the wave drag at high transonic speed.

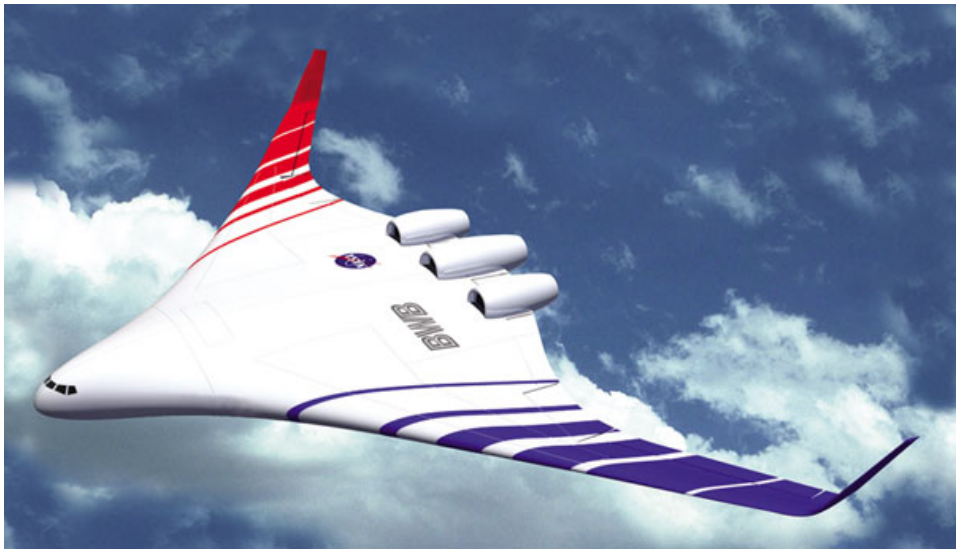

Figure 1.1: Artistic render of a BWB aircraft concept [2].

Safety must be a priority and many are also the problems that the BWB configuration must face. The main problem is that, since the BWB does not have an horizontal tail, the pressure distributions over the centre-body and wings must be carefully designed to maintain trim and the desired stability static margin. The thick airfoil shape of the centre-body also makes it a challenge for the BWB to achieve low drag while generating sufficient lift at a reasonable deck angle. Thus, there are critical trade-offs between aerodynamic performance, trim and stability. The main structural challenge for the BWB is to efficiently carry the pressurization loads during high-altitude cruise flight. The non-circular nature of the cabin cross section requires alternatives to the highly efficient circular shell structure of conventional TAW aircraft. Also is necessary a rethink on how cargo and passengers can be loaded and unloaded on the aircraft and on a new positioning and routes of the

emergency exits. These are a number of critical questions that researchers must address before a BWB can be commercially certified.

1.1.2 Aerodynamic Efficiency

As previously said, the main aerodynamic advantage of the new BWB design is its lower wetted area to volume ratio and lower interference drag compared to the conventional aircraft. Indeed, an increase in $(L/D)_{\mathrm{MAX}}$ of about 20% over the conventional design has been estimated for the blended wing body aircraft [1]. However, these benefits can only be realised as an improved aerodynamic performance through careful and detailed aerodynamic shape design. Unfortunately, little is known regarding the best aerodynamic shape for BWB due to a large number of extra design variables and stronger coupling with the other disciplines such as structures and flight dynamics.

The maximum lift-to-drag ratio $(L/D)_{\mathrm{MAX}}$ depends on the ratio of the aircraft span to the square root of the product of the induced drag factor and the wetted area of the aircraft

$$E_{\mathrm{MAX}} = \left(\frac{L}{D}\right)_{\mathrm{MAX}} = \frac{1}{2}\sqrt{\frac{\pi e}{C_{f,\mathrm{eq}}}}\,\frac{b}{\sqrt{S_{\mathrm{wet}}}} \tag{1.1}$$

From this relation, one can see that larger span, smaller wetted area, lower skin friction (e.g. laminar flow technology), or less induced drag can all potentially provide substantial improvement in aerodynamic performance [3]. One idea could be incorporate an increase from the conventional 70-80 m of span up to 100 m, nevertheless designers still take into account the current airport capability and so the 80 m box rule. The BWB fuselage has a low aspect ratio, this results in a rapid increase in induced drag with lift coefficient thus generating a very low optimum lift coefficient. Also equation (1.1) states that the elliptic lift distribution provides the best (L/D) in cruise. In this regard the BWB generates a near perfect elliptic span-wise lift distribution by combining reflexed centre-body airfoil for pitch-trim stability with outboard supercritical airfoils in wash-out arrangement [1]. However, the elliptic lift distribution, which provides the least induced drag factor in subsonic cruise, might be less attractive in transonic flight condition where the BWB is suited for operation, because it generates strong shock waves at the outer wing due to high local lift. This provides wave drag diminishing the aerodynamic performance.

An optimized choice of wing loading, together with sweep and twist angles, allows to find the optimal value of aerodynamic efficiency.

1.1.3 Flight Control and Stability

The tailless nature of BWB emphasises the need to research new ways of handling the longitudinal stability, trim drag in cruise condition, control effectiveness and allocation. Tailless aircraft represent a distinct challenge when trying to predict their static and dynamic stability performance, since most of the literature that has been written on this subject is geared towards conventional planes.

Aircraft stability can be divided in static stability and dynamic stability. An airplane is considered to be statically stable if: *the forces and moments on the body caused by a disturbance tend initially to return the body toward its equilibrium position.* An airplane is dynamically stable if: *out of its own accord, it eventually returns to and remains at its equilibrium position over a period of time.* The necessary criteria for longitudinal balance and static stability is that $C_{\mathcal{M}_0}$, the pitching moment coefficient at $C_L = 0$, must be positive, so after a disturbance the initial tendency of the airplane will be to return to its equilibrium position. The second criteria is that the pitching moment gradient coefficient of the airplane with respect to its angle of attack $C_{\mathcal{M}_\alpha}$ must be negative such that an equilibrium or trim angle of attack at which the moments about the center of gravity are zero can be achieved. After a wind disturbance on a conventional aircraft, the horizontal tail counteracts the moment generated by the wing. The result is that, after the airplane is disturbed by a wind gust producing a pitching upward moment, the tail creates a negative moment about the center of gravity tending to pitch the nose downward. When the wind disturbance produces a pitching downward moment, the tail produces a positive moment that tends to pitch the nose up. However, the BWB has no tail to provide longitudinal static stability, and hence the means for static stability must be within the wing alone. Therefore the choice of the airfoil to be used is of critical importance. For most flying wings, longitudinal stability is achieved through aerodynamic means such as reflex airfoils, which have a trailing edge camber line lifted upward, generating a positive $C_{\mathcal{M}_0}$, and/or geometric twist (changing of local incidence angle with span). Also wing sweep plays a role on the stability of the aircraft. The static stability margin (SSM) is defined as the distance between the aircraft aerodynamic center lies and the center of gravity, expressed in mean aerodynamic chord $\bar{c}$ fraction

$$\text{SSM} = \frac{(X_{cg} - X_{ac})}{\bar{c}} \tag{1.2}$$

For a statically stable airplane, the static margin needs to be negative, which means that for flying wings the center of gravity needs to be ahead of the wing aerodynamic center, with the wing sweep significantly affecting the location of the latter, X_{ac}, and to a smaller extent the location of the center of gravity, X_{cg}.

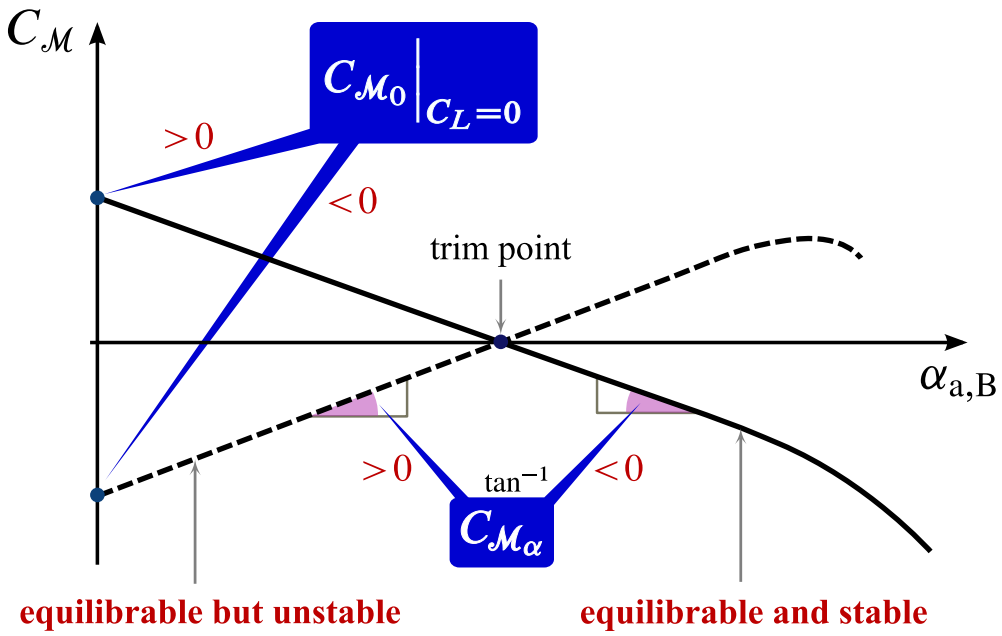

Figure 1.2: Equilibrium and stability criteria: $C_{\mathcal{M}_0} > 0$ and $C_{\mathcal{M}_\alpha} < 0$.

The BWB layout significantly complicates the control system design, due to the assignment of multiple functions to control surfaces and the increasing number of control surfaces for accurate control in all flight regimes. For example, the deflection of an aileron will cause a change in the local lift and drag contributions, thus causing a roll, pitch, and yaw moments to change about the aircraft body axes. Control based on drag can be used for yaw control by deflecting control surfaces on the outer section of the wing. This can be a useful solution to compensate for the absence of a conventional vertical tail plane or a small moment arm of the vertical tail plane. There are two main regimes of control of interest for BWB designs:

- The high speed regime, in which aircraft trim with low drag is important;
- The low speed regime, in which aircraft controllability is important.

A BWB configuration is considered trimmed (at the nominal cruise condition) when the aerodynamic center of pressure is coincident with the center of gravity, and all of the trailing-edge control surfaces are faired. Negative static stability requires that the nosedown pitching moment be minimized. This limits the use of positive aft camber and conflicts with the deck angle requirement, which says that the centre-body airfoils, where the passenger cabin is located, must be designed to generate the necessary lift at an angle of attack consistent with cabin deck angle requirements (typically less than 3°). Taken alone, this requirement suggests the use of positive aft camber on the centre-body airfoils but this can't be overused as previously stated.

Tailless configurations have short moment arms for pitch and directional control, and, therefore, multiple, large, rapidly moving control surfaces are required. Trailing-edge devices and winglet rudders are called on to perform a host of duties, including basic trim, control, pitch stability augmentation, and wing load alleviation. Because some of the control surfaces can perform multiple functions (e.g. outboard elevon/drag rudder offers pitch, roll, and yaw authority), control surface allocation becomes a critical issue. BWB trailing-edge control surfaces cannot be used as flaps because the airplane has no tail to trim the resulting pitching moments. Trailing-edge surface deflection is set by trim requirements, rather than maximum lift. Therefore, the maximum lift coefficient of a BWB will be lower than that of a conventional configuration, and, hence, the wing loading of a BWB will be lower. Low wing loading reduces take-off and landing speeds thus decreasing the required field lengths. Also, low wing loading enables superior climb performance due to increased rate of climb. Similarly, low wing loading enhances the BWB sustained turn performance as it enables it to generate more lift for a given engine thrust compared to a conventional TAW aircraft. However, the BWB will obtain maximum lift coefficient at a relatively higher angle of attack than a conventional aircraft. The high approach flight attitude coupled with the wing surface area increases the sensitivity of the BWB to gust loads. This further increases the local angle of attack to near stall conditions, thereby decreasing control surface effectiveness [1, 4].

The mere size of the inboard control surfaces implies a constraint on the airfoil design to minimize hinge moments. Hinge moments are related to the scale of the control surface as follows: the area increases as the square of the scale and in turn the moment increases with the cube of the scale. Once the hydraulic system is sized to meet the maximum hinge moment, the power requirement becomes a function of rate at which a control surface is moved. If the BWB is designed with a positive static margin (unstable), it will require active flight control with a high bandwidth,

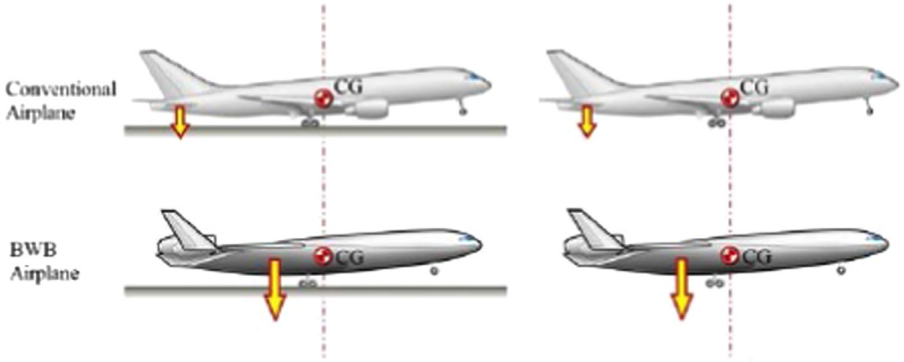

Figure 1.3: Comparison of moment arms between a TAW and BWB configuration [1].

and the control system power required may be prohibitive [1, 4].

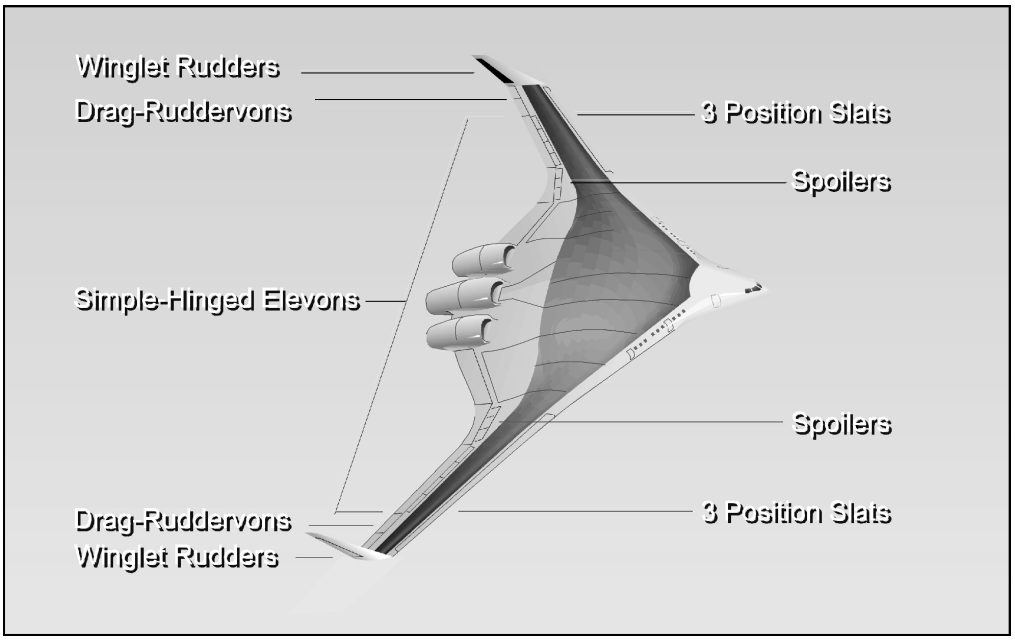

Figure 1.4: Example of a BWB flight control systems configuration [1].

Several concepts have been applied to improve the stability and control of the BWB, one of these is the thrust vectoring. Thrust vectoring generates the same pitching moment as a 10° elevon deflection. However, while elevons unload the outer wings causing an increase in angle of attack, thrust vectoring will maintain the cruise deck angle below 3°. Nevertheless, thrust vectoring adds extra weight and complexity to the design as well as reduce the net axial thrust. Additionally, thrust vectoring increases specific fuel consumption. Other control device that could be used for pitch control is the belly flap. The effect of belly flaps on lift coefficient and pitching moment of the BWB is that using them near the CG of the BWB

increases the static pressure ahead of the CG and decreases it aft (Figure 1.5), producing a pitch-up moment that helps to rotate the BWB during take off and landing. Belly flap deployed to 90° should increase the lift-off lift coefficient and enhances pitching moment by 35% and 10% respectively with only 10% increase in lift-off drag and an negligible loss in lift. Trimming the generated pitching moment could be a major issue though [4–7].

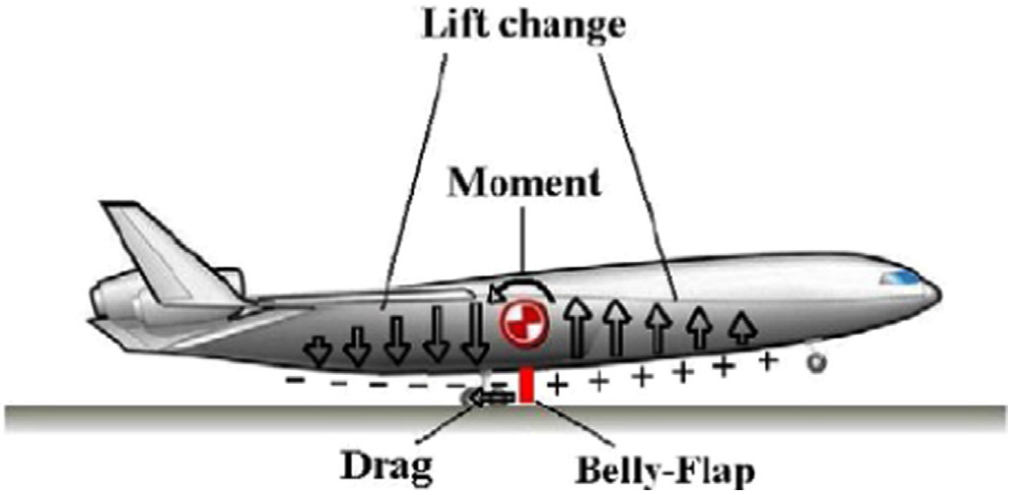

Figure 1.5: Pressure fields induced by a belly flap on a BWB [4].

1.1.4 Aero-Structure

The cabin structure is the most challenging aspect in designing the BWB: it must carry passengers (and eventually payload) and sustain both pressurization and aerodynamic loads. The BWB provides efficient payload distribution and permits over the wing engine placement. Additionally, the BWB centre-body generates lift due to its low aspect ratio thereby reducing the wing load. These features minimise wing bending moment and shear force, thus creating favourable inertia relief (Figure 1.6) and hence reduced structural weight. Additionally, by blending the fuselage and outer wings, lower wetted surface area is obtained. This translates to a higher wetted aspect ratio and hence a structurally more efficient wing [8, 9].

Pressurization is necessary to offer a comfortable atmosphere at optimum cruising altitude. The classic tubular fuselage offers a structurally very efficient shape for a pressurized vessel. In case of the BWB, the integration of the payload section could follow two different paths [8, 9]:

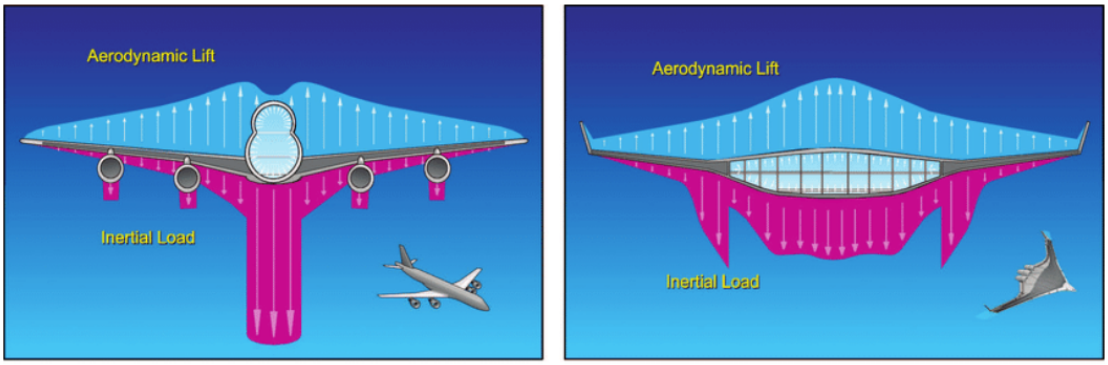

Figure 1.6: Comparison of aerodynamic and inertia load distribution between a conventional configuration and a BWB configuration [1].

Integral Concept The entire section of the center wing containing the payload is built-up as an integral pressurized vessel, hence the shape of the pressurized section is the one of the outer aerodynamic shape. In this the integrated payload compartment offers a lower efficiency with respect to pressurization loads, when compared to the tubular shape. Also the pressure cabin is interrupted by structural elements which impact negatively the passengers comfort. At the same time the aerodynamic shape should be kept unaffected by pressurization. This may lead to a substantial increase of the structural weight. This configuration is very simple and mimics conventional fuselages, both for the integrating vessel and the passengers' evacuation.

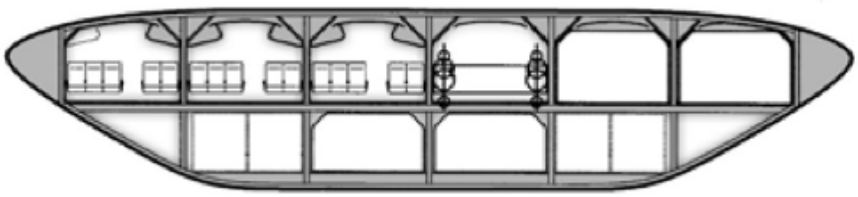

Figure 1.7: Example of Integral Cabin Concept on a BWB aircraft.

Segregated Concept The pressure vessel is mostly independent on the outer shape and can be optimized for minimal structural weight, when subject to the only pressurization loads. However, additional structural components need to be provided to sustain the aerodynamic loads on the external shape. The structure is formed with two skins: the external skin which carries out the aerodynamics and the load transferring; and the internal one which only carries out the pressure load. This solution is very efficient both aerodynamically

and structurally, and it increases passengers comfort, but the double shell adds complexity in the overall design, with consequently penalties in weight. Also, the evacuation can be an issue, since the exit has to penetrate both the shells, a stiffener may be needed.

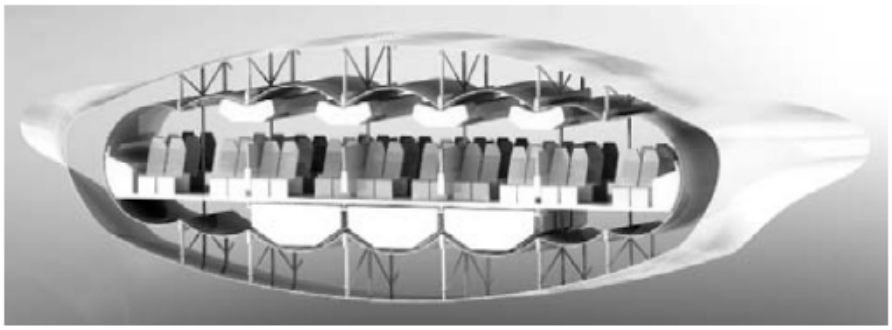

Figure 1.8: Example of Separated Cabin Concept on a BWB aircraft.

Beyond these two configuration also an *Oval Cabin* concept has been researched. It focuses on the passenger comfort: they have an uninterrupted view in the pressure cabin which enhances their orientation and acceptance; it also allows natural light throughout the cabin. The evacuation is done in the same way as in the integrating concept, with cutaways in the outer shell. This concept mostly resembles the cabin of a conventional configuration. On the other side this configuration is the more complex: in every design phase a compromise between structural, aerodynamic efficiency, and payload integration has to be found. It has shown the largest amount of pressurized space, introducing penalties in weight and in the aerodynamics design, which is compromised by structural requirements [8, 9].

The BWB provides a lot of space underneath the cabin for the center tank. This can be used to efficiently trim the aircraft in cruise flight. However, this makes the fuel system safety critical, because it must always be operational to keep the aircraft center of gravity within an acceptable range. Additionally, fuel transfer between the central and outboard fuel tanks could be used, in approach, to shift the center of gravity aft in order to align it with the center of pressure without deflecting the elevon, minimising trim drag. Therefore, it is crucial to ensure that the fuel system is designed to cope with the centre of gravity variation resulting from different payload level (baggage and passengers) and variation of fuel volume on-board along the flight.

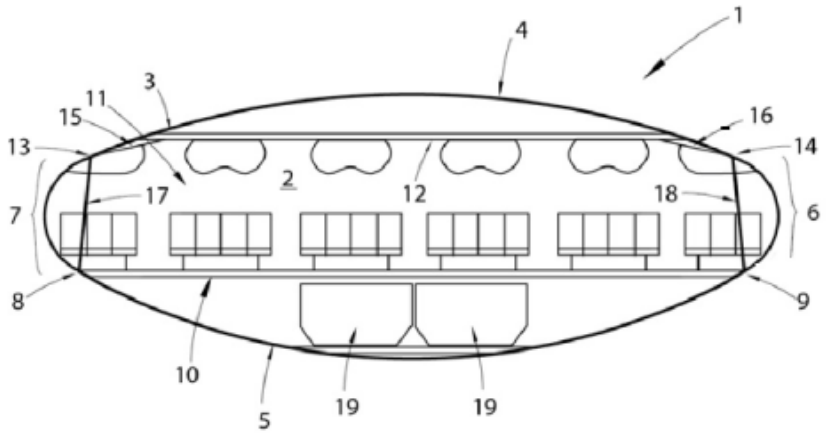

Figure 1.9: Example of Oval Cabin Concept on a BWB aircraft.

1.1.5 Propulsion

The engines on the BWB aircraft are often located over the wing, aft of the aircraft centre-body. This arrangement helps to offset the weight of the payload, furnishing, and other systems, thus ensuring a balanced airplane. Over-the-wing mounting allows higher by-pass ratio engines to be installed without the risk of violating ground clearance limits. Furthermore, mounting jet engines above the wings takes advantage of the Coanda effect to increase lift and improve short-field take-off and landing performance. Over-the-wing engine placement also reduces the risk of foreign object damage as they are less prone to sucking debris. However, over-the-wing engine mounting distorts lift distribution creating poor cruise aerodynamics. Distortion could be minimised through careful centre-body design to obtain a synergy between aero-structural and propulsion airframe. Positioning the engine aft of the aircraft centre-body moves the centre of gravity aft to coincide with the centre of lift there by minimising pitching moment and reducing trim requirement. Location of the engine aft of the centre-body also enhances laminar flow thus reducing surface friction drag. Also, it can take advantage of boundary-layer ingestion (BLI) because boundary layer is fully developed in the aft region of the centre-body. BLI can improve the propulsive efficiency by reducing ram drag. This assumes that an inlet can be designed that provides proper pressure recovery and uniform flow at the fan face of the engine. Alternatively, the boundary layer can be diverted (BLD) around the sides of the inlets, but this implies dumping low-energy air into an already transonically stressed pressure recovery region. Simply mounting the engines on pylons is another option, but increased wetted area and weight

plus nose down thrust moment are detractors from this installation. Additionally, embedded engines brings the thrust line closer to the centre of gravity thereby reducing nose down pitching moment. This also minimises trim problem together with control surface size and power requirements. Embedded engines brings along the complexity of accessing the engine for maintenance, thermal insulation, system routing etc. In order to provide access to the various parts of the engine, a lot of access cutouts need to be placed in a highly stressed structure, adding complexity and weight of the structure design. On the other hand, podded engines are kept separated from each other and from the aircraft in the event of fire and no need of detachable skin panels guarantees easy accessibility. In order to mount larger engines it is sufficient to redesign only the pylon.

The distribution of a large number of small BLI engines along the trailing edge to force sufficient boundary layer into engine intakes has also been advanced. Distributed propulsion reduces engine-out over-sizing requirements and provides synergy between air craft aerodynamics, structures, controls, and high lift devices. Additionally, distributed propulsion replaces separated trailing edge flow with exhaust jet thus reducing induced drag and improving propulsive efficiency. Distributed propulsion can be used with thrust vectoring for control or as high lift devices. Thrust vectoring decreases low speed airframe noise due to reduced trim drag. Distributed propulsion engine arrangement decreases the amount of directional control power required in critical engine out conditions due to much reduced asymmetric thrust moment. Further to this, it redistributes engine weight over the airframe providing passive load alleviation and reduced wing weight. Consequently, distributed propulsion allows for a lighter wing and increase the L/D ratio compared to pylon-mounted engines. They are however heavier with a higher specific fuel consumption due to the scale effects of small engines used in distributed propulsion system. Scale effects refers to decreasing engine performance with reduced engine size. Smaller engines are subject to increased pressure and heat losses due to lower Reynolds number and a relative increase of leakage flow [10–12].

1.1.6 Environmental Footprint and Marketing Potential

The BWB could reduce pollutants emission and provide a lower noise signature due to lower installed thrust, reduced fuel burn, efficient aerodynamic configuration, use of simple trailing edge devices, and a lighter airframe. The high aerodynamic efficiency achievable by the BWB translates to about 20-30% savings in fuel burn

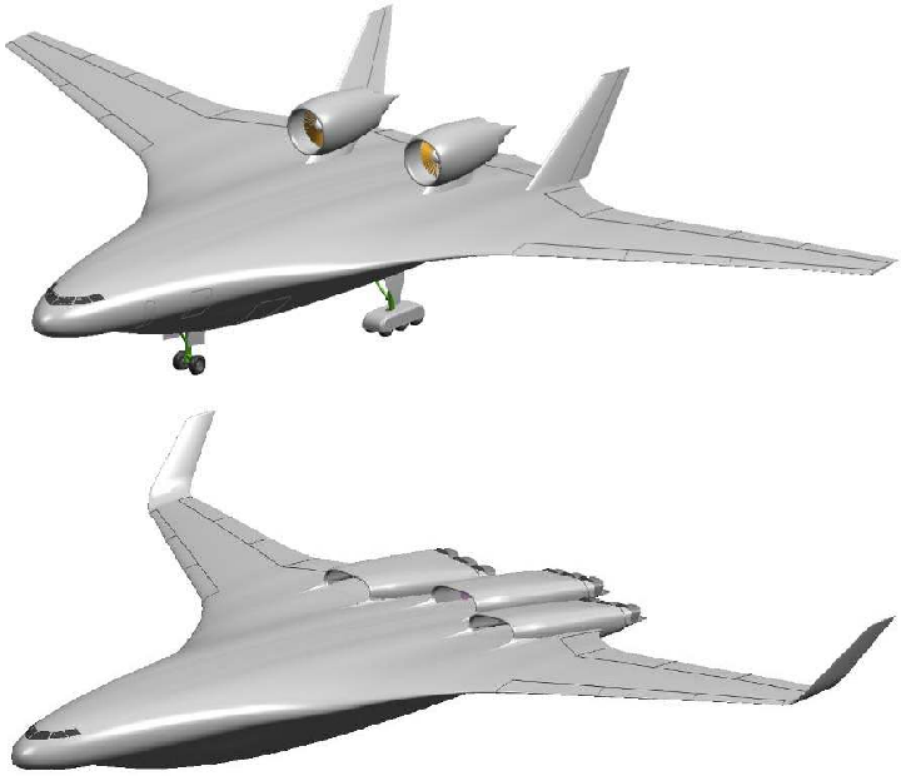

Figure 1.10: Example of a podded and embedded with distributed propulsion engine for a BWB aircraft.

when compared with a conventional aircraft of the same weight. BWB aircraft permits the use of laminar flow control (LFC) technologies over the wing with correspondingly higher fuel savings, this could decrease of about 40% the emission of CO_2 compared to a conventional aircraft. The BWB naturally offers a low acoustic signature, before any specific acoustic treatment. The centre-body shields forward radiated fan nose, and engine exhaust noise is not reflected from the lower surface of the wing. Airframe noise is reduced by the absence of a slotted flap trailing-edge high-lift system.

Reduction in fuel burn translates in a reduction of about 10-12% in DOC with a corresponding increase in revenue yielding payload. A typical BWB concept leads to 30% fewer parts counts, reduced manufacturing difficulties and lower manufacturing costs. The BWB has a short centre-body, therefore loading and unloading could be accomplished in a shorter time. Furthermore, the BWB can take off from a shorter runway without the need for complicated high lift devices. The thick center-body section required to accommodate passengers and payload creates a manufacturing challenge: while the outer wing panels and nose sections are of identical geometry for all family members, the dimension of the center-body

(and also the transition section aft of the nose and engines) vary with payload capacity, therefore commonality, a crucial topic for the fleet demand of an airline company, would have an impact on manufacturing costs. Nose gear and outer main gear could be common for all family members, with a center main gear of varying capacity added where required. Commonality extends naturally to the interior, once the commitment to the centre-body growth concept is made. Consideration needs to be given to the requirement to ensure that the resulting aircraft fit into the 80 m box specified for Class VI airports.

1.1.7 BWB Design Prospects

Despite potentially high aerodynamic and possible structural efficiencies, the BWB concept has not yet been embraced by aircraft manufacturers. One argument is that BWB have some inherent disadvantages/challenges that can partially offset its advantages. Large leaps in aircraft efficiency, coupled with reductions in noise and harmful emissions, are critical to the aviation community's resolutions of achieving environmental sustainability. It cannot be excluded that the arguments in favor of or against the BWB are often based on the superficial suspicion against the introduction of new technology. Instead, a satisfactory decision must be based on a rational investigation of a class of vehicles with various degrees of integration of configurations using multi-disciplines. All the advantages and disadvantages are summarized below.

Advantages Reduction of the skin friction drag due to wetted area reduction. Trim drag during cruise can be avoided by adopting relaxed stability in pitch. Interference drag reduction by smooth transition of centre-body and wing. Reduction of lift-induced drag due to lifting body and improved spanwise lift distribution. Wave drag reduction at high transonic speed due to better area-ruled shape. Simplified high-lift devices, wing weight reduction and better high-altitude buffet margin can be realized due to reduced wing loading. Engine integration on the aft-upper centre-body has the potential to provide greater noise shielding outside cabin than conventional aircraft. Local relieving of aerodynamic loading by local inertia loading can reduce bending and shear loads on the structure. The simplicity of the configuration suggests a reduction in part count with a corresponding reduction in manufacturing costs.

Disadvantages Weight penalty due to non-circular pressurized body. Inferior flying and handling qualities due to relaxed stability, limited control authority

and complex flight control system. Recovery capability for potential tumbling for tailless aircraft. Degraded comfort due to windowless cabin. Difficulties on satisfying the requirement of evacuation and on airworthiness certification. Sensitive to gust due to low wing loading. Degraded repairability comparing with TAW that indicating further infrastructure investment. Limitations on large size BWB due to taxiway and runway width limits, gate limits and strong wake vortices. Potential problems of family development.

1.2 BWB Design Mission

1.2.1 Designers Choices on BWB Specifications

The design of the BWB starts having a special consideration on long haul transport with large aerodynamic advantages over conventional TAW configuration. One of the first project conducted by NASA in 1994 was given to a NASA/industry/university team led by McDonnell Douglas/ Boeing company on BWB technology study, which resulted in the second generation BWB (BWB-800-II). This study demonstrated the feasibility and performance potential of the BWB and one of the design mission was a 800 passengers (PAX) aircraft [13, 14]. Also commonality was considered a huge benefit for the BWB concept, so the design was also adapted in a 450 passenger configuration: this specification allowed for some comparison of the resulting BWB with the B747, A340, and the then-pending A3XX, so it was considered nominal, and the final passenger count would be established as the airplane was configured and sized [1]. With the VELA project (*Very Efficient Large Aircraft*), ran from 2002 to 2005, number of passenger came back to a larger amount as the earliest projects. This project investigated two extremes of a BWB configuration: this gave rise to the concepts of VELA 1 and VELA 2, from them the VELA 3 configuration was derived with a 750 passenger capacity [15]. So most of the modern projects and researches settles the very large BWB concept with a 800 passengers specification [16].

McDonnell Douglas/Boeing company initial project proposed a 7000 nm range and a cruise Mach number of $M = 0.85$ [13, 14]. The VELA3 is designed to cruise at $M = 0.85$ to a range of 7200 nm [15]. Most BWB designs have used $M = 0.85$ as a cruise design point as this is consistent with current large transport aircraft operation. BWB should achieve best efficiency at a cruise Mach number of 0.85 and acceptable efficiency at $M \leq 0.95$. Long range specification, somewhere around 7000 nm, is considered predominant due the economy demand.

Liebeck [1] compared the effect of reduced wetted surface area on the lift coefficient of an 800-passenger BWB and a conventional tube and wing aircraft of same capacity. This phenomenon was investigated by transforming a 650 m^2 ball into a cylinder and a lifting body and then sizing the streamlined options to accommodate 800 passengers. Subsequently, following the integration of the wing, empennage and engines, Liebeck [1] showed that a conventional aircraft with 4 under the wing engines has a wetted surface area of 4100 m^2 while the BWB with trailing edge BLI engines has only 2800 m^2 for the same passenger capacity, a 33% reduction

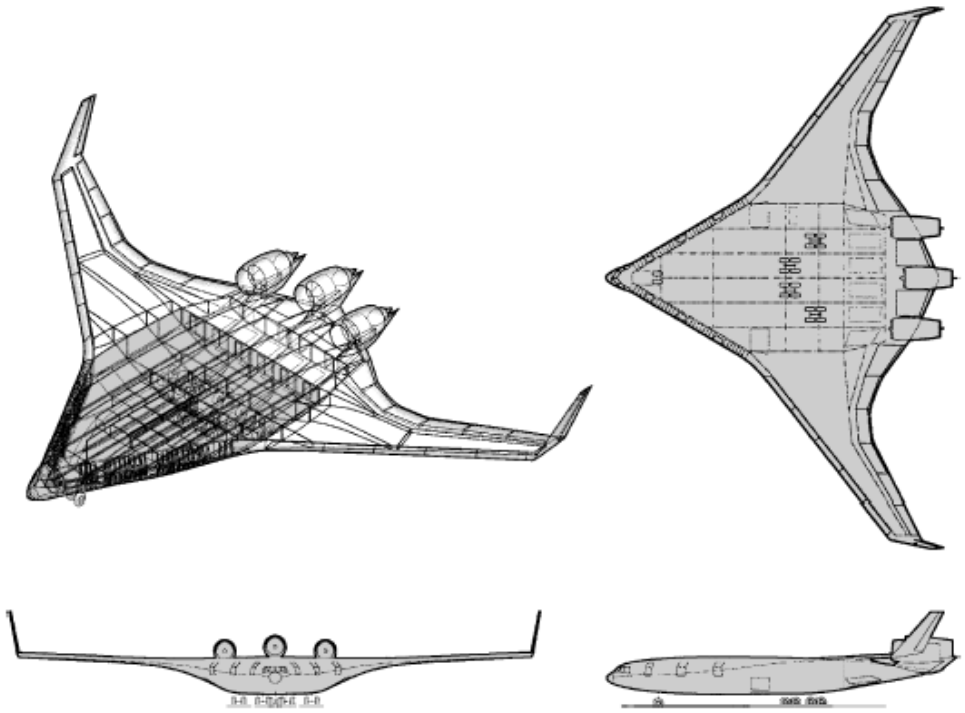

Figure 1.11: BOEING BWB-450 baseline [1].

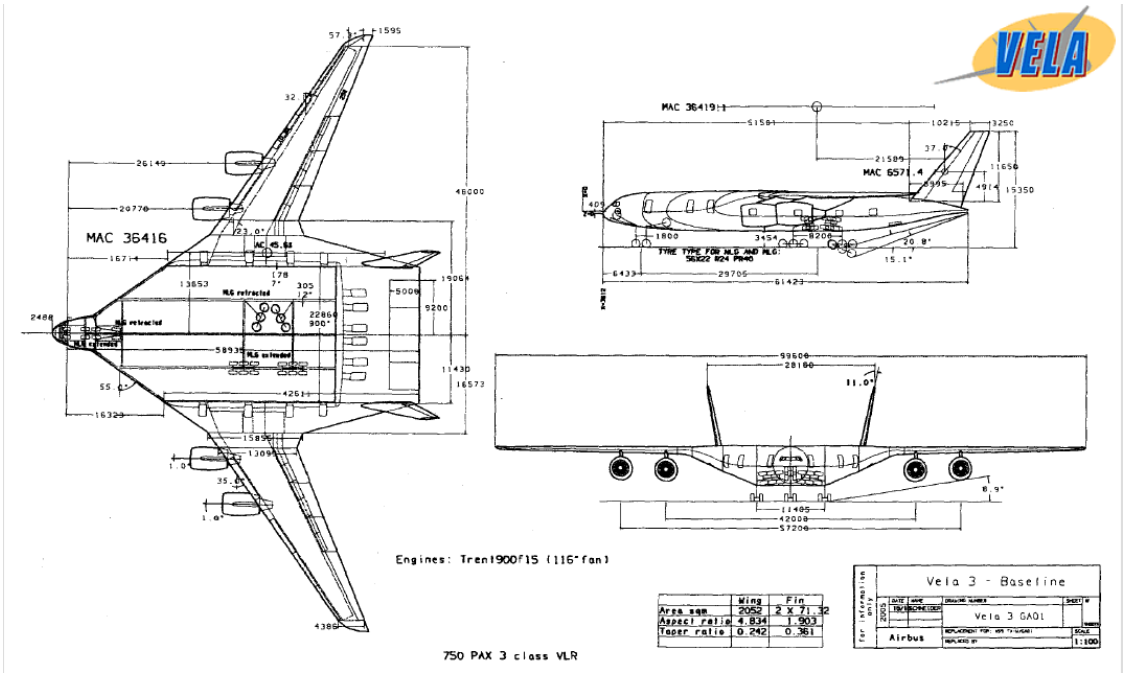

Figure 1.12: VELA 3 baseline [15].

in wetted surface S_w area (Figure 1.13). From statistics we could assume that the ratio between the wetted surface S_w and the reference surface S area is around a value of 2.4. VELA 3 [15] has a wing surface area of $S = 2052\,\mathrm{m}^2$ while the second AEROPP airframe [16] has a wetted surface area of $S_w = 2756\,\mathrm{m}^2$.

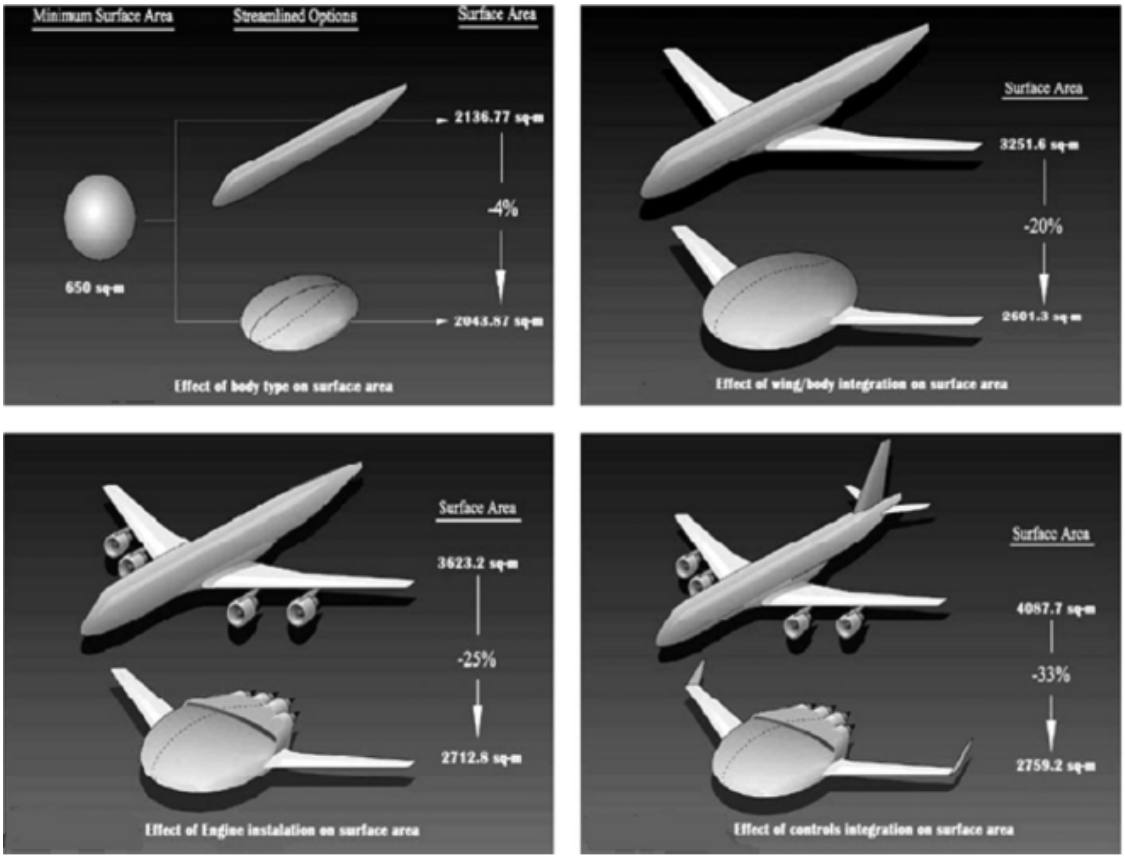

Figure 1.13: Genesis of the BWB concept from a sphere [1].

The centre-body, with its very large chord, calls for correspondingly lower section lift coefficients to maintain an elliptic spanload. The low section lift requirement allows the very thick airfoils for packaging the passenger compartment and trailing-edge reflex for pitch trim, while modern supercritical airfoils with aft camber and divergent trailing edges are assumed for the outer wing. The thick central body hold major load over the airframe allowing outboard wing to be thinned adequately and preventing wave drag development over the wings. Using a reflex airfoil could compromise the transonic behaviour: due to three-dimensionality, most of the centre-body lift is generated at the front. For a reflex airfoil, this zone needs more curvature to counteract the lose of lift in the afterward part. As such, the critical and drag divergence Mach numbers are lower than that of a conventional

Figure 1.14: Rendering of the second AEROPP configuration [16].

airfoil, with potentially issue in the transonic regime. To limit the contribution to compressibility, as general rule, the thickness-to-chord ratio for the centre-body must not exceed $(t/c)_{\max} = 18\%$.

The length of the centre-body is normally less than the span width b. As pointed out in Section 1.1.2 for the BWB the span can be increase to 100 m, such as for the VELA 3 project [15]. The BWB-800-II evolves from 106 m span and a trapezoidal aspect ratio of 12 to 85 m span and a trapezoidal aspect ratio of 10, indicating a significant difference in potential aerodynamic performance, nevertheless other designers choose to limit the span to a slightly larger one such as 85 m or within an 80 m box requirement in order to accommodate airport capability [1, 16]. All the BWB concepts could be divided in two parts: an inner wing part, where the centre-body lies and the thickness-to-chord ratio is higher, that blends with an outer wing part that behaves like a traditional wing. Therefore we could differentiate the aspect ratio of the aircraft for the inner (AR_{inner}) and outer (AR_{outer}) wing part.

As for the aspect ratio definition we could also define a sweep angle for the inner and for the outer part, in which the first has a higher value than the latter. Values in the order of 60° at leading edge (Λ_{LE}) are found in the inner part, where the nose of the BWB lies, while in outer part more conventional values of 30-35° up

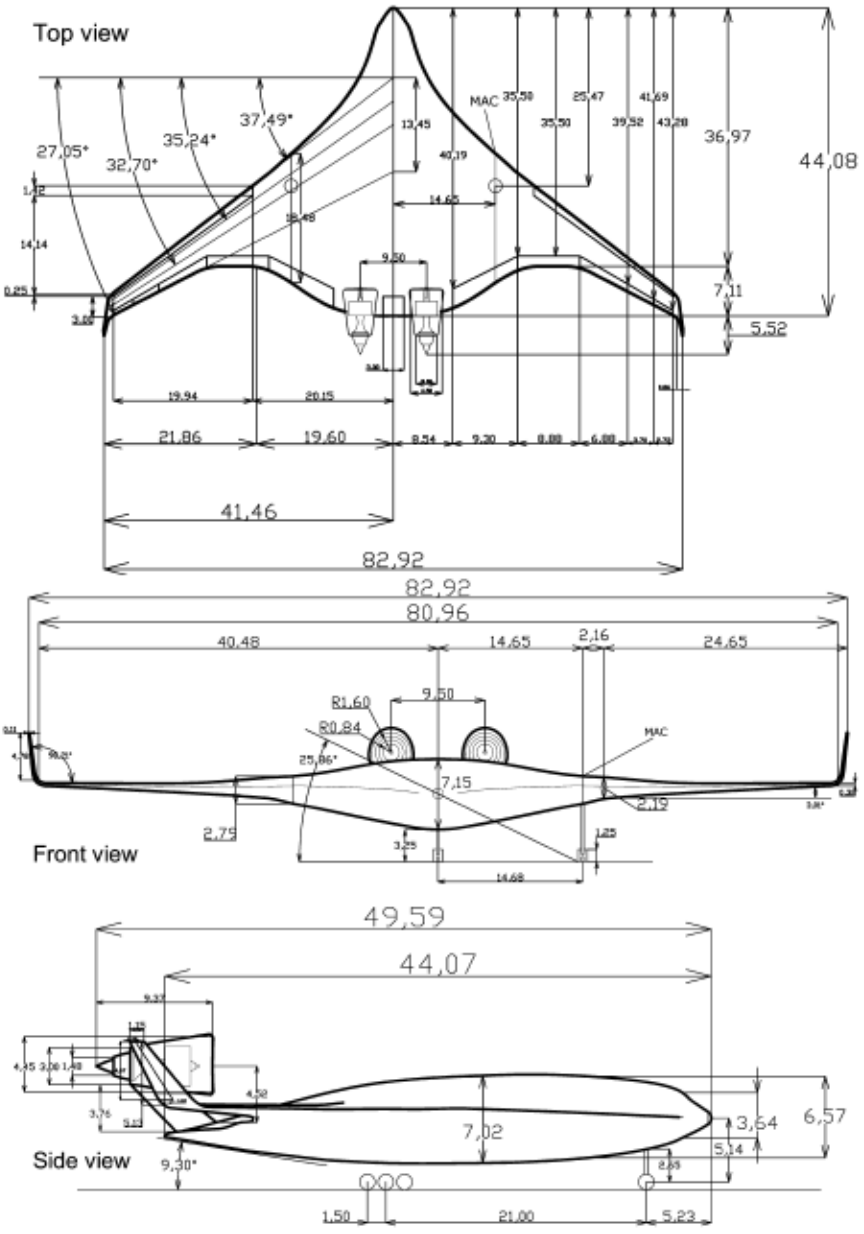

Figure 1.15: Technical drawing of the second AEROPP configuration [16].

to 40° are found [1, 13–16]. As a swept flying wing, the outboard wing may be highly loaded if not properly twisted. The typical shock on the outboard wing is smeared into a compression wave on the centre-body. The flow pattern on the centre-body remained essentially invariant with angle of attack, and flow separation is initiated in the kink region between the outboard wing and the centre-body, where the chord length is lower. Small section chords are an issue for stall due to the low Reynolds number. This is a requirement for a slat system extending from the kink, which is the section between the central body and the outer wing, to the wing tip. The kink region however is the ideal spanwise location for the stall to begin, from a flight mechanics point of view: the ailerons remain effective, and pitch-up is avoided. Outer wing flow remains attached, providing lateral control into the stall regime. Similarly, the flow over the centre-body remains attached and provides a nearly constant flow environment for the engine inlets. This flow behavior is a consequence of significant lateral flow on the centre-body that provides a three-dimensional relief of compressibility effects.

1.3 Structure of the thesis

Chapter 1 has given a general overview on the BWB project pointing out the most important goals of it.

Chapter 2 will outline a selection of data for the design sweep analysis. A methodology will be developed consisting of an algorithm which will make use of OpenVSP and VSPAERO software [17] in order to achieve the desired results. A briefly theoretical explanation on the software and the *Design of Process* methodology will be made.

Chapter 3 will display those results. Thanks to the *Design of Process* methodology and a post-process algorithm, the most important specification for each designed responses will be shown.

2

Design Methodology

2.1 BWB Aerodynamic Analysis

2.1.1 Introduction

The current BWB investigations mainly focus on conceptual design, have a feature of inherent-multidisciplinary integration, and appear as a Multidisciplinary Design Optimization (MDO) problem. Trade-offs between different disciplines cannot be avoided. As pointed out in Chapter 1 the BWB has a strong synergy between aerodynamic efficiency and stability, integration of structure aerodynamic behaviour, comfort and safety, special consideration on lower emissions and noise pollution. Each of these topics strongly resembles the economic and social trends of this century, therefore all the aviation companies are increasingly encouraging researches on the BWB.

The hybrid nature of the BWB and the fact that this kind of innovation is so recent and in an early stage translates in a lack of adequate information on the topic, information that we could find on research papers or studies. In this Chapter, data and information are gathered in order to achieve a first design of a BWB aircraft. A Design of Experiments will be implemented through an algorithm designed in a MATLAB [18] workspace that will make use of the OpenVSP [17] software in order to achieve an aerodynamic analysis of the BWB.

2.1.2 Data Gathering

In Chapter 1.2.1 a general overview of the choices and the purposes of different designers on BWB specifications has been pointed out. In this section a selection on the most significant data will be made in order to perform an aerodynamic analysis on different BWB designs.

A collection of specification was integrated on a Excel [19] spreadsheet. A trend line between a specific data and the year of publication of the paper, where the data was derived, was made: by doing so it is possible to point out a clear view on how the specification evolves with the technology evolution. After that, a minimum and maximum rounded value for all the specifications have been imposed.

As the BWB planform geometry was defined in Section 1.2.1 in an inner and outer wing part that blends together in a kink region, specifications are also defined for the inner and the outer wing part. The first specification imposed is the Aspect Ratios $\mathit{Æ}_{\text{in}}$ and $\mathit{Æ}_{\text{out}}$, while the span will be derived from it by the algorithm. Only one value of the root section chord c_{root} and thickness-to-chord ratio $(t/c)_{\text{root}}$ are chosen while the choice of taper ratios λ_{in} and λ_{out} are preferred in order to derive kink and tip chords in the algorithm. Finally sweep angles $\Lambda_{\text{inner,LE}}$ and $\Lambda_{\text{outer,LE}}$ measured at leading edge, twist angles $\varepsilon_{\text{kink}}$ and ε_{tip}, and thickness-to-chord ratios $(t/c)_{\text{kink}}$ and $(t/c)_{\text{tip}}$ are imposed. All the data are summarized in Table 2.1.

All the values in Table 2.1 well represent actual values for a BWB concept. In order to achieve a Design of Experiments with a greater variation in aerodynamic responses, a second set of data where the gaps between minimum and maximum value are increased, is imposed. All the data are summarized in Table 2.2.

Table 2.1: Specification and Values for first Design of Experiments.

Specification	Levels	Values
$\mathcal{R}_{\text{in}}$	2	[0.5 , 2]
$\mathcal{R}_{\text{out}}$	2	[3.5 , 5.5]
c_{root}	1	40
λ_{in}	2	[0.2 , 0.35]
λ_{out}	2	[0.15 , 0.5]
$\Lambda_{\text{inner,LE}}$	2	[61 , 64]
$\Lambda_{\text{outer,LE}}$	2	[37 , 41]
$(t/c)_{\text{root}}$	1	0.18
$(t/c)_{\text{kink}}$	2	[0.10 , 0.12]
$(t/c)_{\text{tip}}$	2	[0.08 , 0.10]
$\varepsilon_{\text{kink}}$	2	[1 , 2]
ε_{tip}	2	[−4 , −5]

Table 2.2: Specification and Values for second Design of Experiments.

Specification	**Levels**	**Values**
AR_{in}	2	[0.5 , 2]
AR_{out}	2	[3.5 , 5.5]
c_{root}	1	40
λ_{in}	2	[0.2 , 0.4]
λ_{out}	2	[0.15 , 0.5]
$\Lambda_{\text{inner,LE}}$	2	[55 , 65]
$\Lambda_{\text{outer,LE}}$	2	[35 , 45]
$(t/c)_{\text{root}}$	1	0.18
$(t/c)_{\text{kink}}$	2	[0.10 , 0.12]
$(t/c)_{\text{tip}}$	2	[0.08 , 0.10]
$\varepsilon_{\text{kink}}$	2	[−2 , 4]
ε_{tip}	2	[−2 , −7]

2.2 Geometric modellization

2.2.1 BWB planform geometry

The starting point of the BWB geometric modelisation begins with the planform choice. As we defined the inner and outer wing specification in Tables 2.1 and 2.2, actually the BWB planform can be divided in a multiple number of sections. For the scope of this thesis all the BWB designs generated by the Design of Experiments will have two wing regions, an inner and outer part, blended together. For each wing part a 6° dihedral angle Γ is chosen. As we chose two wing sections, three airfoils are chosen.

For a first airfoil selection, the choice lies on:

Root Section Liebeck Airfoil

Kink Section NASA Supercritical Airfoil

Tip Section NASA Supercritical Airfoil

While for a second airfoil selection, the choice lies on:

Root Section Liebeck Airfoil

Kink Section Liebeck Airfoil

Tip Section NASA Supercritical Airfoil

The Liebeck airfoil is a reflex profile used in the inner sections in order to improve the trimmability of the BWB as described in Chapter 1.1.3. NASA supercritical airfoil is chosen for its good transonic behavior while retaining acceptable low-speed characteristics. Thickness-to-chord ratio for the kink and tip sections changes according to the Design of Experiments (Table 2.1 and 2.2).

2.2.2 The geometric modeller OpenVSP

OpenVSP (Vehicle Sketch Pad) is a parametric aircraft modeling tool for conceptual aircraft design. The software allows the user to create a 3D model of an aircraft defined by common engineering parameters without expending the expertise required

for traditional Computer Aided Design (CAD) packages. This model can be processed into formats suitable for engineering analysis. The predecessors to OpenVSP have been developed by J.R. Gloudemans and others for NASA since the early 1990's. On January 10 2012, OpenVSP was released as an open source project under the NASA Open Source Agreement (NOSA) version 1.3 [17]. An aircraft shape is the natural starting point for multidisciplinary analysis and optimization (MDAO). The outer mold lines and structural layout are the drivers for and interface between aerodynamics, structures, mass properties, and all the physics that impact a vehicle's performance. Parameterisation facilitates design and optimization by reducing the problem dimensionality and improving descriptive expressiveness. The aerospace industry and designers in particular have long described aircraft geometry parametrically: familiar quantities such as aspect ratio, taper ratio, sweep angle, and thickness to chord construct a common vocabulary for aircraft shape.

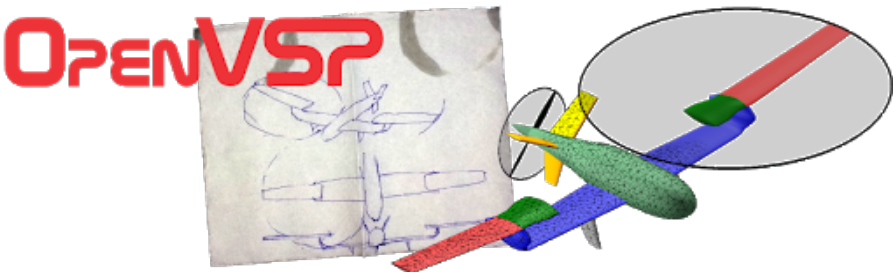

Figure 2.1: OpenVSP Logo [17].

The first part of the user interface allows the parameterisation of the geometry planform of the aircraft. In order to obtain a BWB planform only a `WING` geometry part can be added, because the fuselage is modeled like a part of the wing (Figure 2.2 and 2.3). In this thesis work aerodynamic behaviour with propeller and control surface will not be considered, so each of this part are not considered for parameterisation. Once the `WING` geometry has been generated, the `WingGeom` option can be opened (Figure 2.3). Name, color, and number of tessellation defining the wing can be modified. The `XForm` option shows that the wing geometry is generated only on one axial plane, the other part is considered symmetric: the axial plane symmetry and the axial system can be modified (Figure 2.4). Specification values for the total planform are selected in the `Plan` option, where either span or area planform can be selected in order to obtain the desired value for aspect ratio (Figure 2.5). The total wing planform can be divided in two or more wing sections, in the `Sect` option values for span, root and tip chord, sweep, twist and

dihedral angles are chosen (Figure 2.6). Also, in `Airfoil` section an airfoil from the OpenVSP library or an uploaded one can be chosen (Figure 2.7). In the `Blending` option all the sections leading and trailing edges are blended together in order to achieve a typical BWB planform (Figure 2.8). A typical BWB planform is presented in Figure 2.9. OpenVSP selects a *construction* reference axis: the origin axis is fixated at the anterior end of the aircraft, *x-axis* is positive towards tail, *y-axis* towards right semi-wing and *z-axis* towards the foot-head of the pilot.

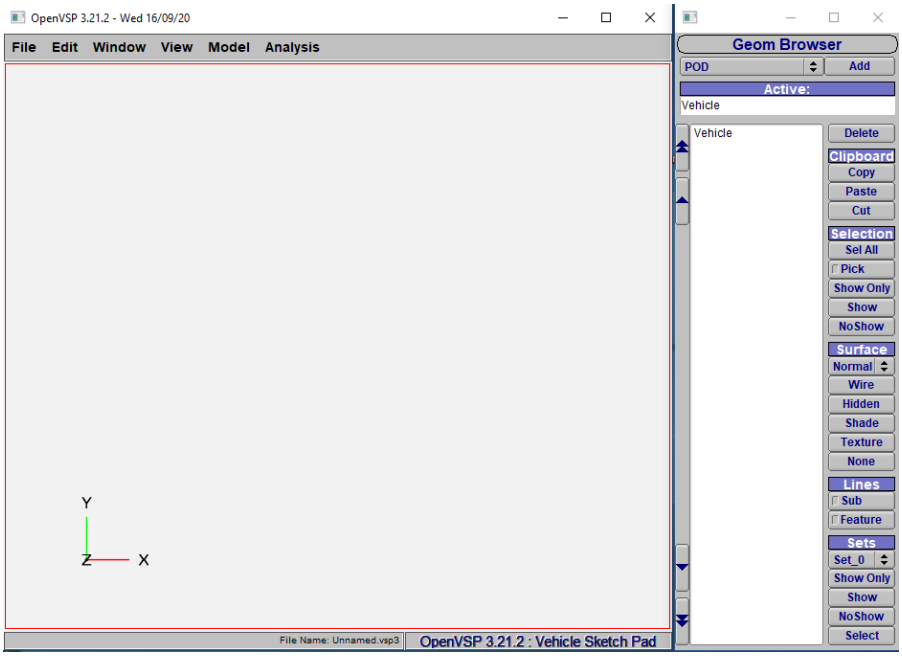

Figure 2.2: OpenVSP user interface.

Once we have an appropriately defined model to analyse, we need to provide a degenerated geometry file if running the vortex lattice method or a Cart3D surface triangulation file if running the panel method. A highly detailed model may look nice, but in general there is no need of having a very fine resolution to solve for aerodynamic characteristics. Usually, a much lower resolution will converge to a solution around the expected value. In Figure 2.10, taken from [20], a comparison of two models is provided: the low resolution model has around 4100 cells and will run to completion in a matter of 5-10 minutes, while the high resolution model has 19200 cells and would take hours. The difference between the results of these two would be less than 5% which is much less than the error typically created in model geometry assumptions. Optimizing meshes for numerical solvers is an area of active research and generally follows the following logic: areas with large gradients get a

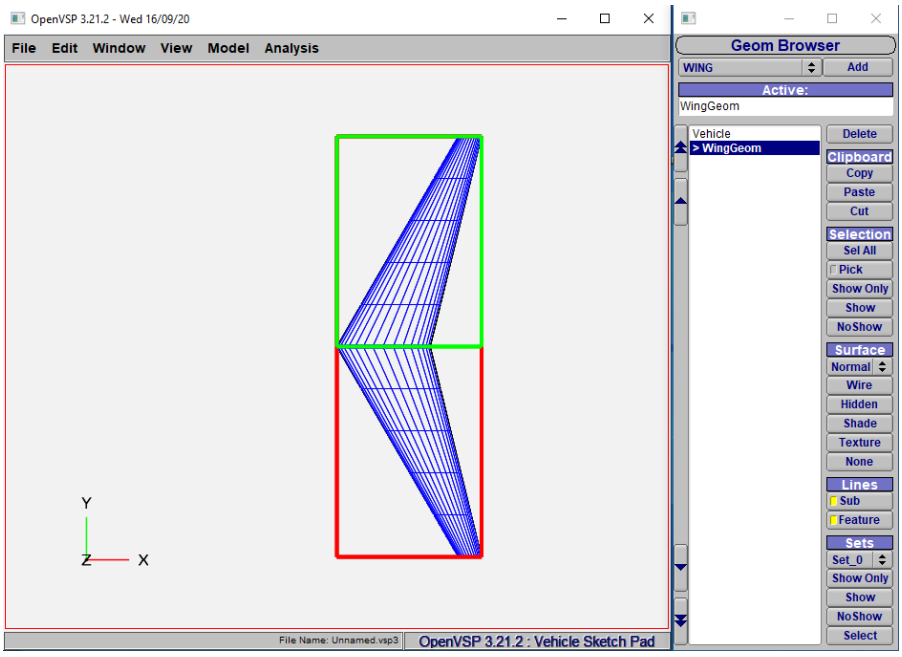

Figure 2.3: OpenVSP wing part.

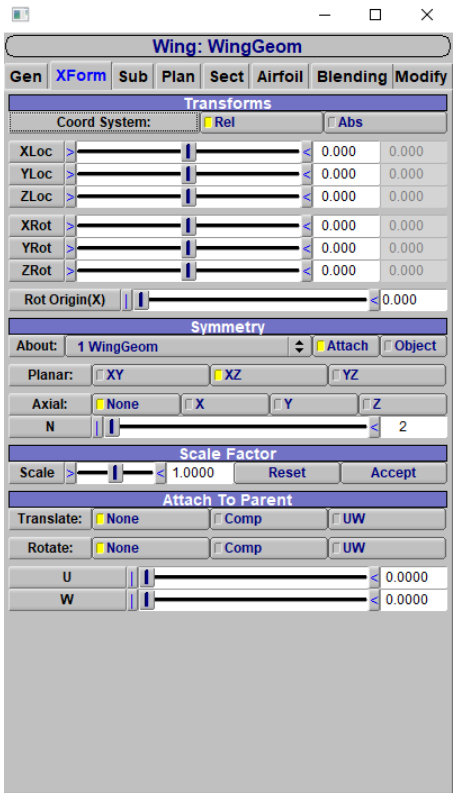

Figure 2.4: OpenVSP XForm option.

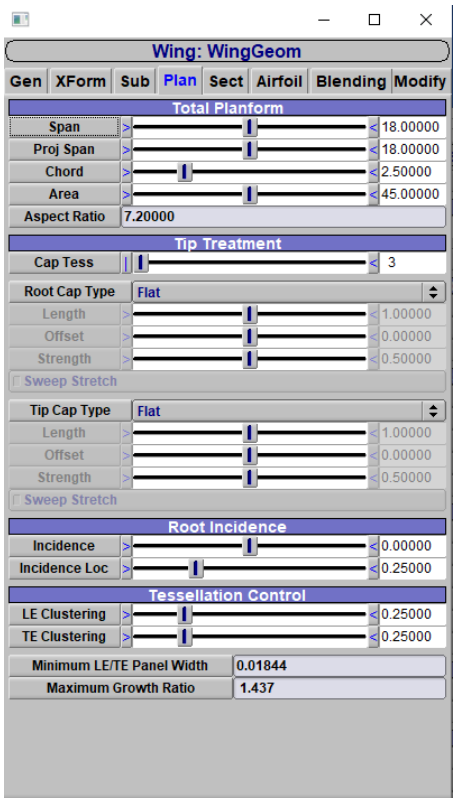

Figure 2.5: OpenVSP Plan option.

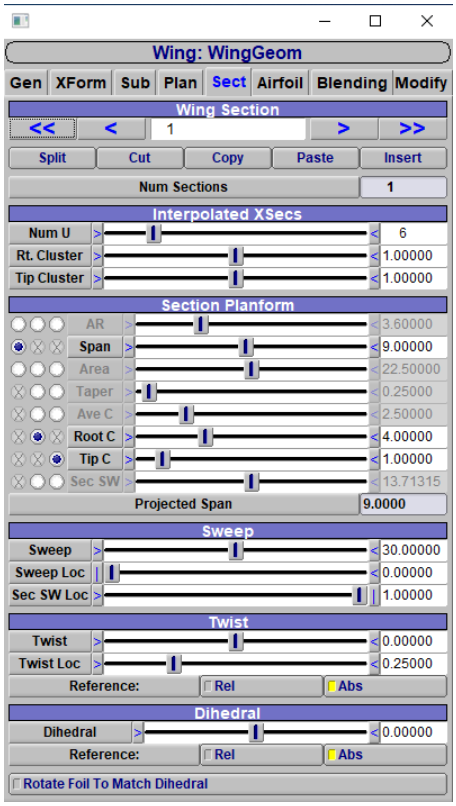

Figure 2.6: OpenVSP Sect option.

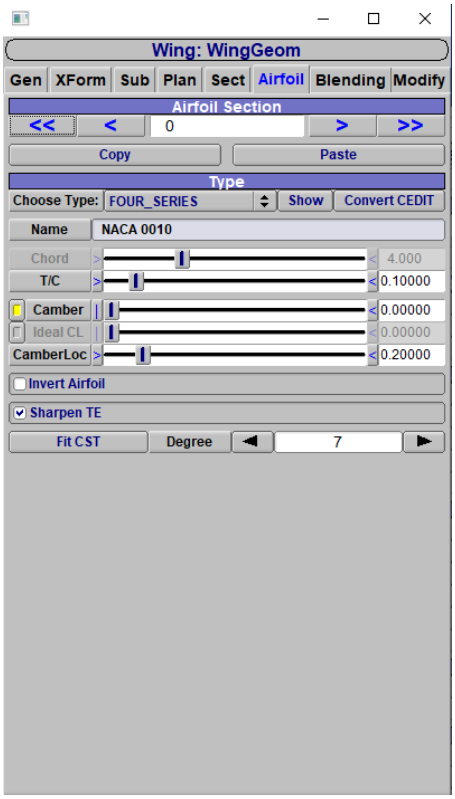

Figure 2.7: OpenVSP Airfoil option.

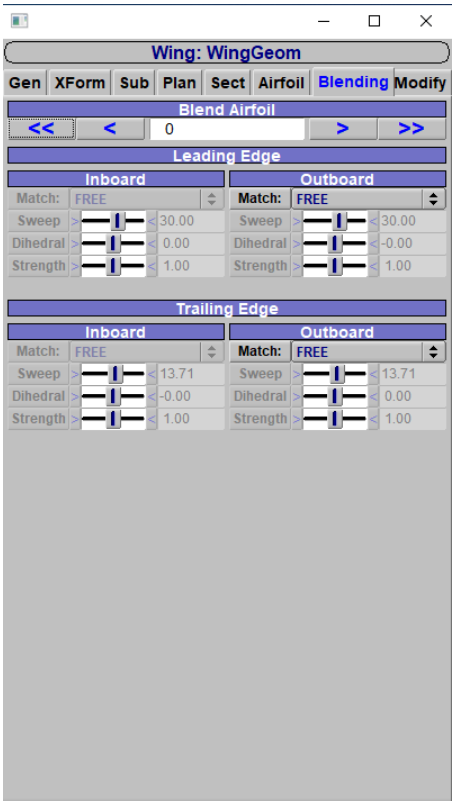

Figure 2.8: OpenVSP Blending option.

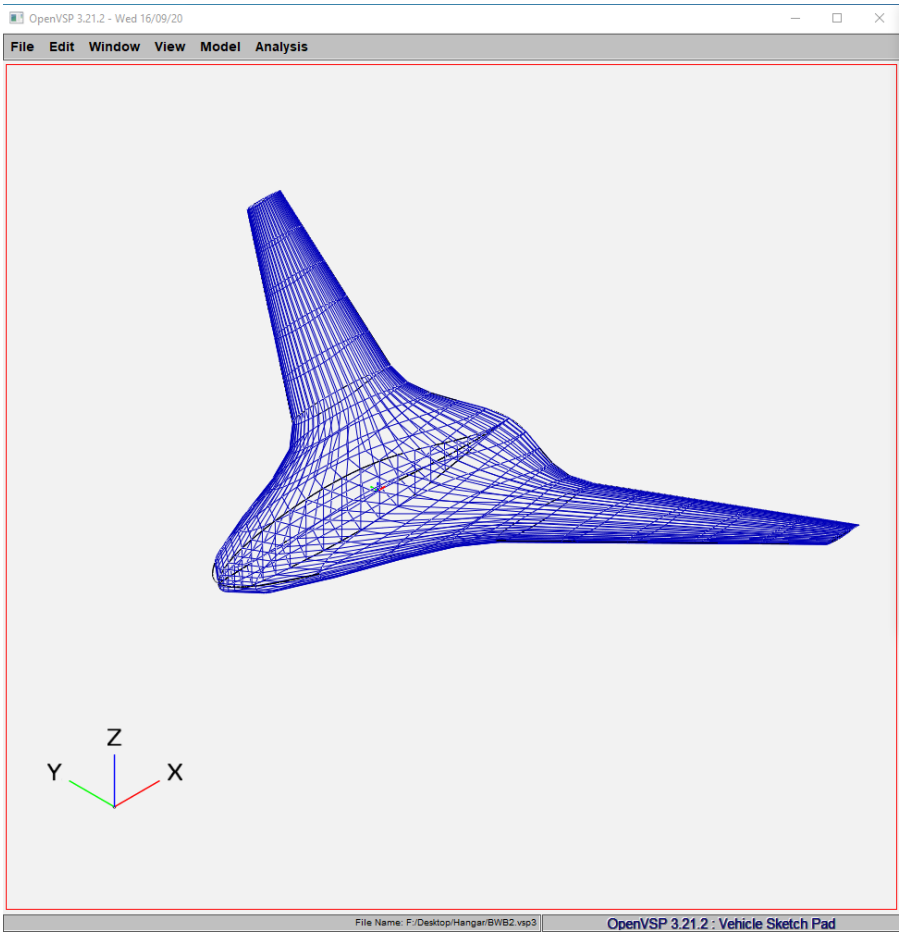

Figure 2.9: Typical BWB planform generated on OpenVSP.

finer mesh and ignore sections that do not significantly contribute. For example, a fuselage will not significantly contribute to lift or induced drag, so for initial design steps it can generally be left out of most of the analyses. Also, the wing sections can be finely defined to capture effects of downwash or propeller slipstream while leaving most of the wing coarsely defined. This is particularly useful when observing low speed conditions where the local C_l is much higher than at cruise.

The degenerated geometry file is required if running VSPAERO's vortex lattice solver (see Section 2.3.2). Degenerated geometry files are representations of three dimensional models in progressively simple frames. For example, a three dimensional model is represented in its entirety, followed by a flat-plate representation, followed by a stick representation. The process of degeneration is represented in Figure 2.11.

The characteristics of each of the representation are described below [21].

Surface Surface node location

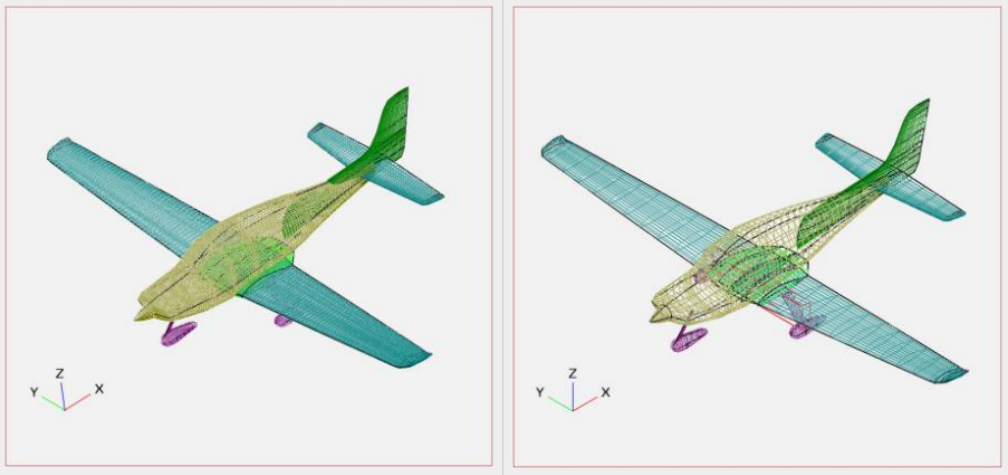

Figure 2.10: Degenerated Geometry.

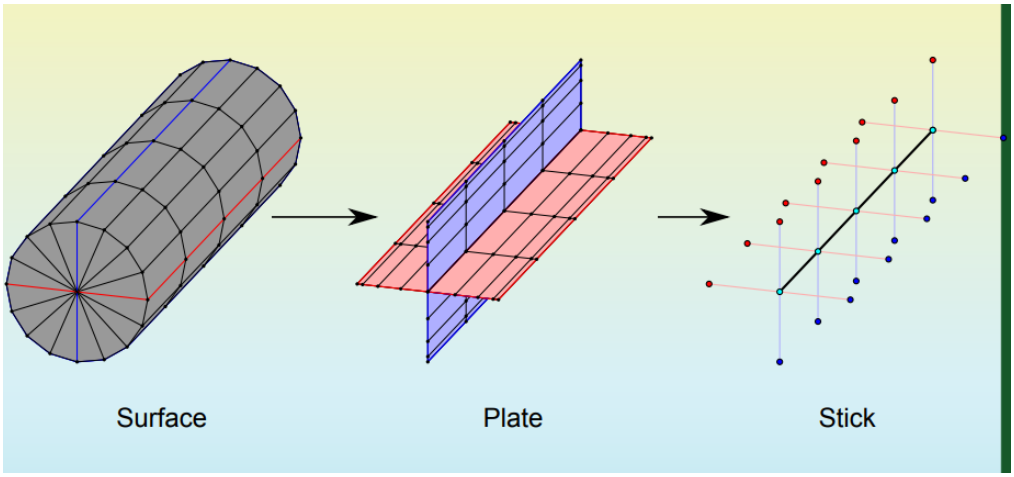

Figure 2.11: Degeneration of the geometry [21].

Parametric u & w
Surface normal vector

Plate Plate node location
Parametric u & w_{top}, w_{bot}
Plate normal vector

Stick LE & TE node location
Parametric u
Thicknesses

Point Surface area & volume
Wetted area & volume
Sweep

Applying the *DegenGeom* command will write a comma separated value (`.csv`) file and a MATLAB (`.m`) file. The `.csv` will be used once VSPAERO is launched [21].

CSV Ready-made MS Excel File
Easily human-readable
Easily parsed (C, Fortran)

MATLAB Information direct to data structure
Remove parsing barrier
Design students in mind

Nodes of degenerated models are consistent with the geometric abstraction of the analysis method, therefore they could also serve as repositories for the resulting analysis data. Make stored data available to subsequent higher-order and lower-order analyses in whatever level of abstraction they require, regardless of the degenerated model on which the original analysis was based.

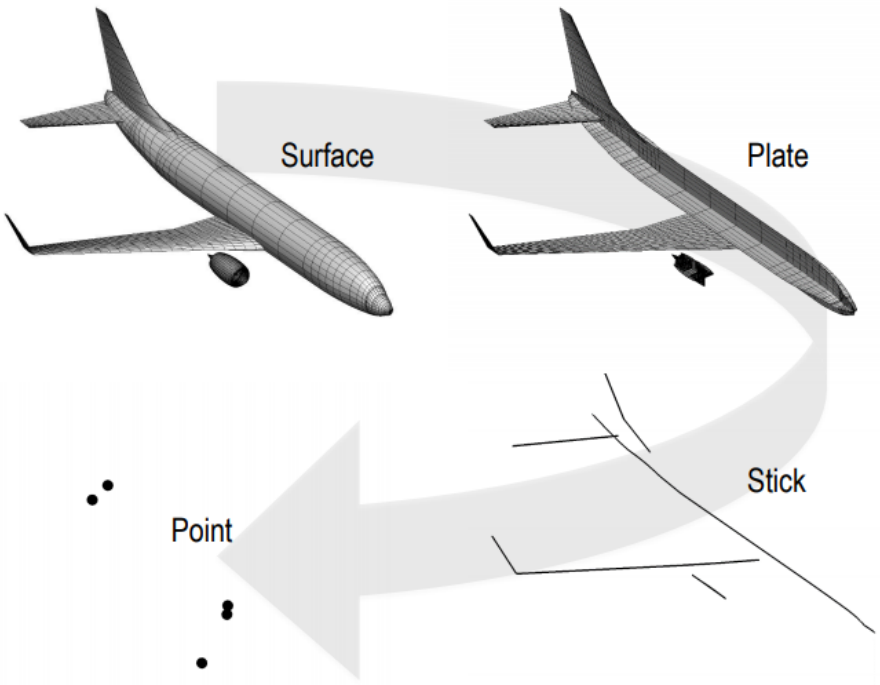

Figure 2.12: Degeneration of an aircraft geometry [22].

OpenVSP is also integrated with an aerodynamic analysis toolbox called VSPAERO. Once the geometry planform has been defined all the reference area and lengths,

mandatory for an aerodynamic analysis, can be derived from the planform model. Also from the toolbox a centre of gravity calculation is achieved (Figure 2.13). In addition to the analysis implemented by VSPAERO there are also other tools, like the Parasite Drag toolbox that includes semi-empirical methods for the calculation of the parasite drag (Figure 2.14).

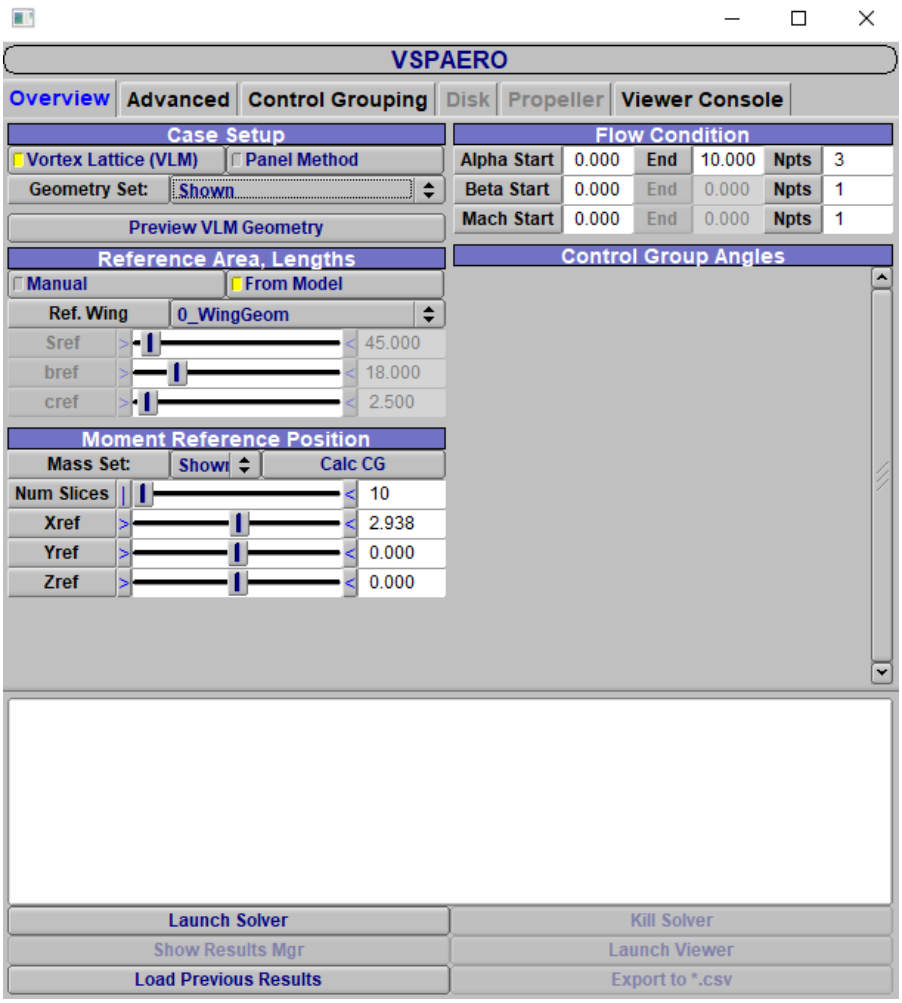

Figure 2.13: VSPAERO aerodynamic analysis toolbox.

In Figure 2.15 a description of the typical work-flow in OpenVSP is provided.

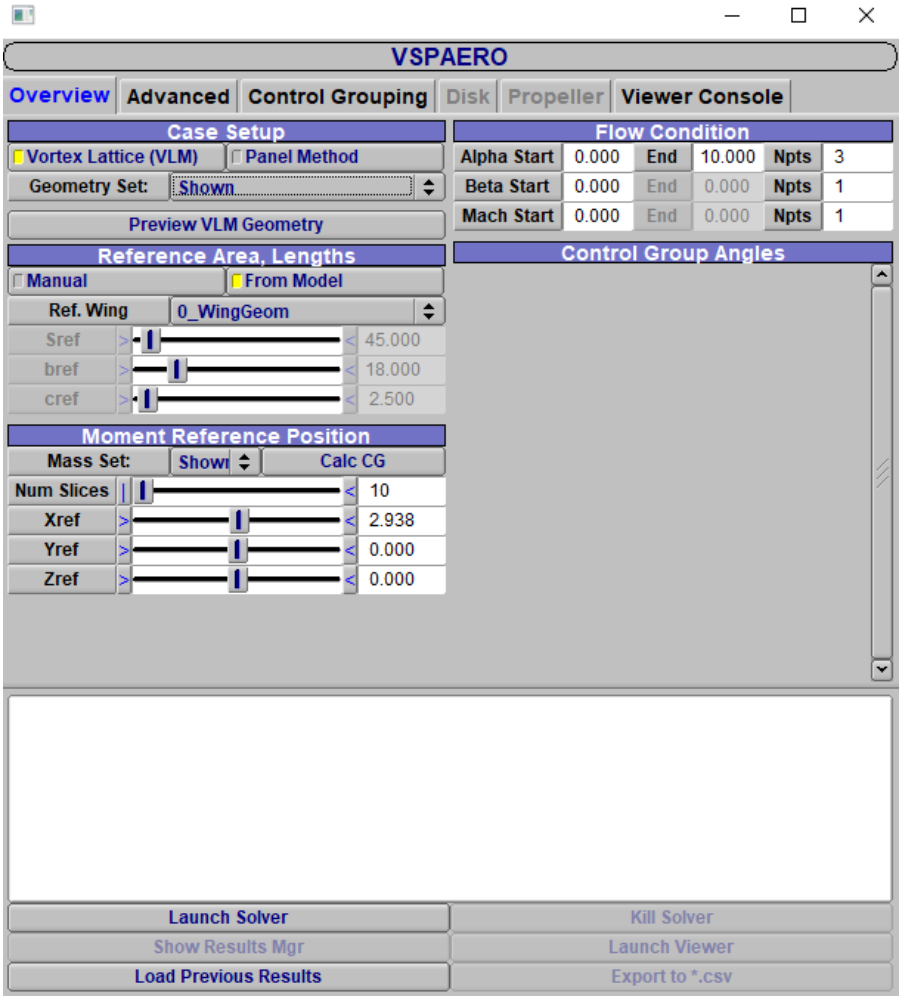

Figure 2.14: Parasite Drag analysis toolbox.

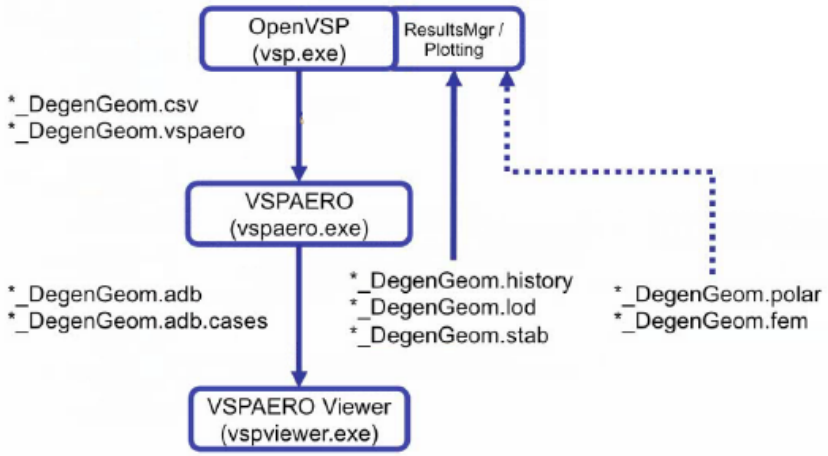

Figure 2.15: OpenVSP workflow.

2.3 Design exploration algorithm

2.3.1 MATLAB code

Once the choices implemented by the Design of Experiments are defined (see Section 2.1.2), a MATLAB script is employed in order to generate all the possible combinations of BWB planform. The scope of MATLAB script is to create all the needed input files in order to run OpenVSP and VSPAERO (see Section 2.3.2 for the theory on which is based and how can perform), the first for creating the required geometry and the second for the aerodynamic evaluation of the BWB planform. The main and all the functions scripts are designed to recreate the OpenVSP commands format following the API Documentation (see [23]). A schematic flow chart of the algorithm is provided by Figure 2.16.

The algorithm starts with the definition of the Design of Experiments chosen for the case, the specification values seen in Table 2.1 and 2.2 will be the needed inputs for the algorithm. Once the inputs are established, the algorithm enters in a series of `for` cycles that sweep across all the specifications and their values, creating 1024 different combinations of a BWB planform. Also other variables are derived from the input specification, such as the chord and the span values that are not user-defined.

In the `Set OpenVSP Input file` part of the algorithm a MATLAB structure is defined with the values that have been established in the previous part, also this structure carries information on which blending options we want to set for the planform. After that a `MakeVspscript` function acquires these data and creates a `.vspscript` file in order to run OpenVSP and obtain a `DegenGeom` output file.

Next is the VSPAERO setup, where another MATLAB structure is defined with the aerodynamic inputs required by VSPAERO for the analysis. In particular the centre of gravity global coordinate X_{cg} is set as a percentage of the mean aerodynamic chord, previously calculated by an external function, while the Y_{cg} and Z_{cg} coordinates are set as 0. With the function `MakeVspaero` a `.vspaero` file is created and with `DegenGeom` file VSPAERO can be launched for the aerodynamic analysis. At this point a flag named `ex`, initially equal to 0, warns if the analysis has met a convergence point, if not `ex` will be different from 0. In parallel, with the `.vspaero`, file a parasite drag calculation is written with the API functions of the Parasite Drag Toolbox (Figure 2.14). Once the aerodynamic analysis has been performed and the convergence is achieved, a `.polar` file is acquired, with the

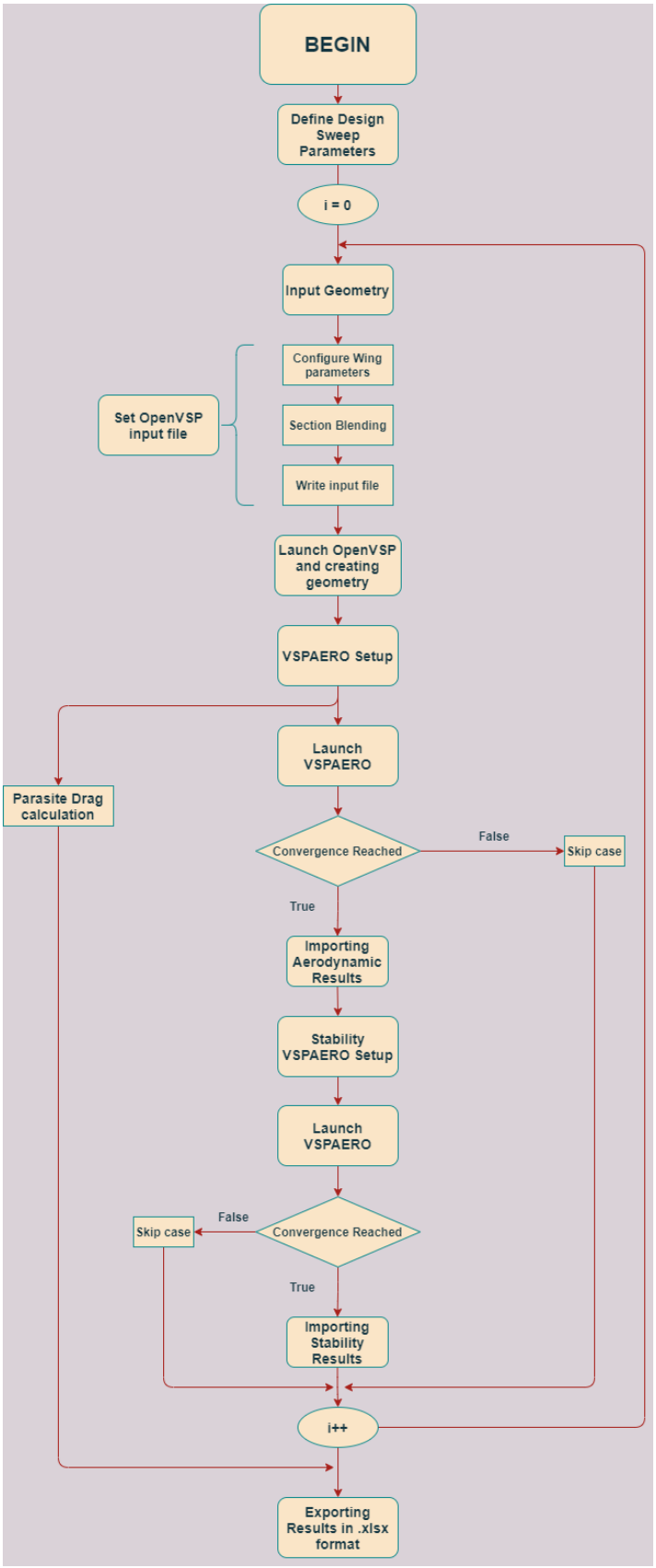

Figure 2.16: MATLAB algorithm flow chart.

`ImportResults` function the desired data from the file are imported in the MATLAB workspace in order to fill the `Results` structure, and with the `MoveResults` function all the generated files are moved in the designated output folders. If the convergence has not been achieved, the case is skipped and can be analysed later.

Similar to the previous part, a Stability analysis is made with another VSPAERO setup, the difference lies in setting the angle of attack equal to 0. Indeed stability calculation relies in small changes of the responses around the initial value. The `ex_stab` flag will warn if the convergence has been achieved, if not the stability case is skipped and can be later analysed. All the data for a converged case are imported from a `.stab` file into the MATLAB workspace with the `ImportResultsStab` function, filling the `Results` structure.

At this point the cycle is finished, the cycle counter increases and all the calculations are repeated for another combination. When all the combinations are analysed the algorithm exits from the cycle. In the final part of the algorithm, the data acquired for all the combinations, stored in the `Results` structure, is re-arranged in arrays in order to be exported in a spreadsheet `.xlsx` file, to be easily read by the operator.

2.3.2 The aerodynamic software VSPAERO

VSPAERO is a fast, vortex lattice analysis solver used in the open source OpenVSP suite. It is a linear solver based on linear potential flow theory and it can use either vortex lattice method or panel method, therefore will not model stall characteristics or, in fact, separation of any kind. In this thesis work only the vortex lattice method will be implemented, which theory is summarized below.

Vortex Lattice Methods (VLM) is based on the following assumptions:

- The flow field is incompressible, inviscid and non rotational.
- The lifting surfaces are thin. The influence of thickness on aerodynamic forces are neglected.
- The angle of attack and the angle of sideslip are both small (small angle approximation).

Although their region of application and absolute accuracy is limited, VLM are still widely used for estimating aircraft aerodynamic characteristics. The VLM is a numerical method used in computational fluid dynamics, mainly in the early stages

of aircraft design. The VLM models the lifting surfaces of an aircraft, such as a wing, as an infinitely thin sheet of discrete vortices to compute lift and induced drag. The influence of the thickness and viscosity are neglected. By simulating the flow field, one can extract the pressure distribution or as in the case of the VLM, the force distribution, around the simulated body. Starting from this knowledge is possible to evaluate the aerodynamic coefficients that are useful for assessing the aircraft's handling qualities in the conceptual design phase. What is important to underline is that at this kind of level is not possible to evaluate the viscous drag, while is possible to compute the induce drag starting from the production of lift. Since the VLM is based on potential flow theory, its validity is restricted to the linear aerodynamic region, and hence it is principally only valid in the low-angle of attack flight regime (cruise). Further, Mach number effects in subcritical flow can be accounted for using Prandtl-Glauert correction. The VLM is the extension of Prandtl lifting line theory, where the wing of an aircraft can be modelled as an infinite number of Horseshoe vortices. Instead of only one horseshoe vortex per wing, as in the lifting line theory, the VLM utilizes a lattice of horseshoe vortices. First of all, the surface is approximated, for example a wing can be approximated with its average surface, and then it's partitioned into flat quadrilateral panels. Thus we have a superimposition of a finite number of horseshoe vortices of different strengths Γ_n on the wing surface. In Figure 2.17 we can see the representation of a single panel on the wing.

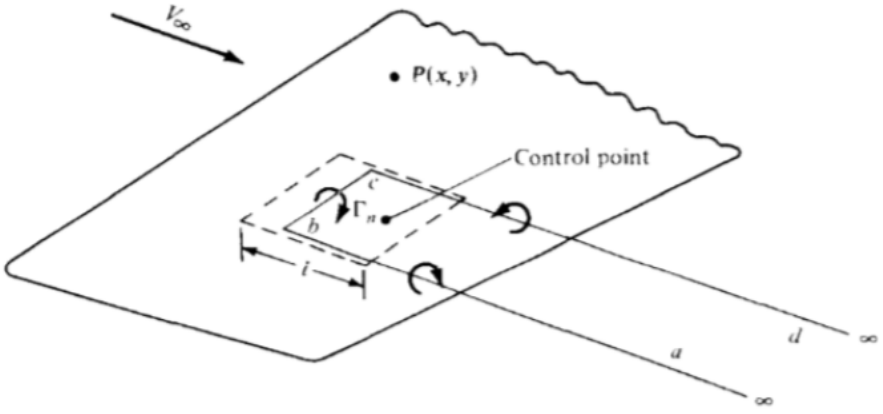

Figure 2.17: Representation of a single horseshoe vortex, which is a part of a vortex system.

The dashed lines define a panel on the wing planform, where l is the length of the panel in the flow direction. A horseshoe vortex, *abcd*, of strength Γ_n is placed

on the panel such that the segment bc (adherent part of a horseshoe vortex) is a distance $l/4$ from the front of the panel. A control point is placed on the centerline of the panel at a distance $3l/4$ from the front.

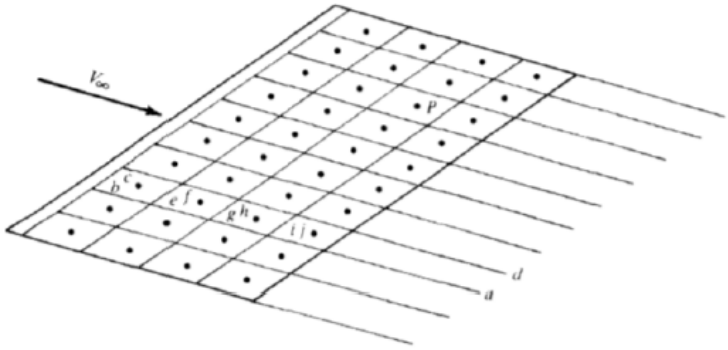

Figure 2.18: Representation of a Lattice of horseshoe vortex.

In Figure 2.18 it is represented the entire wing covered by a finite number of panels. In order to obtain the aerodynamic coefficients, the strengths of each of the horseshoe vortices must be found considering that vector sum of their induced velocity and the freestream contribution at each control point satisfies the boundary condition of a zero normal velocity component. The induced velocity at a point due to a straight line segment of a vortex filament is given by the Biot-Savart Law. After solving a system of equations for the vortex strengths they can then be integrated over the surface to obtain the forces and moments. One of the major problem to consider for the VLM is that it fails near the wing leading edge and the tip where the thickness effect are very important. The problem is in fact the inability of the method to reasonably calculate the local pressure distribution; the total (and local) forces, however, are predicted to a quite acceptable level. An important assumption for the further analysis of the vortex induced velocities at the control point is the fact that the wake is assumed to be flat and lying in the plane of the wing at $z = 0$. Numerical investigations, however, have shown that this restriction in general leads to satisfactory lift and induced drag values for wig having moderate to high aspect ratios (e.g. $\mathcal{AR} > 6$). The number of vortices used vary with the required pressure distribution resolution, and with required accuracy in the computed aerodynamic coefficients. A typical number of vortices would be around 100 for an entire aircraft wing. The finite number of horseshoe vortices that are placed in trapezoidal panels, approximate the continuous distribution of vorticity that leaves the wing surface. One thing that should be noted is that

the VSPAERO solver is not based on the classic VLM where horseshoe vortices are distributed along the wing, but is characterized by vortex rings. The trailing vortices are simulated as an infinite distribution of vortex rings. Figure 2.19 shows this kind of discretization of the wing and ring elements.

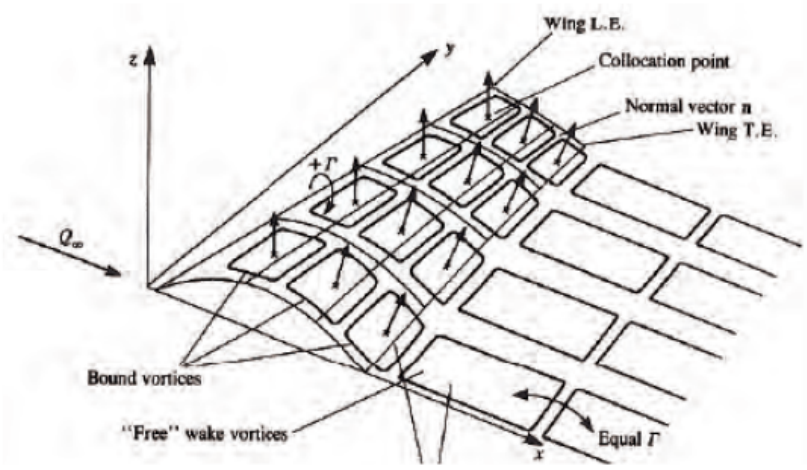

Figure 2.19: Representation of a Lattice of horseshoe vortex with ring elements.

VSPAERO analyses the `DegenGeom` file generated by OpenVSP. In order to start the analysis an input file with the operating conditions must be defined. The drag output provided, only contains information on the induced part. Use of components in the `DegenGeom` build file that do not affect lift will cause excessive operating times with no valuable return, as for example nacelle and fuselage. So when using VSPAERO, the main components which control the output values are the lifting surfaces such as the wing and horizontal stabilizer. While the other body components will have some small effect on the profile drag of the vehicle, the induced drag which VSPAERO determines is based primarily on the lift coefficient. It comes with Viewer app which displays wakes and ΔC_p (pressure coefficient change) gradient. VSPAERO has a number of processes that are related to convergence. The GMRES solver is an approximate iterative matrix solver. Very important parameters are 'Reduction' and 'Maximum'. These are measures of the error of the matrix solution at that point in the iteration. In particular Reduction is $\log(\rho/\rho_0)$ and Maximum is $\log(\rho)$, where ρ_0 is the residual on the first iteration. Convergence is set to $\rho < 1 \times 10^{-3}$, so that $\log(\rho) = -3$. Second, it uses time stepping wake filaments that update their shape in response to the flow, and it is possible to set the number of wake iterations.

Once our model has an associated `DegenGeom` file, we can begin writing our setup

file. VSPAERO recognizes this file by the name `modelname_DegenGeom.vspaero` if running the vortex lattice method. An example of a setup file is provided by Figure 2.20.

```
Sref = 720.1532
Cref = 23.0313
Bref = 56.2
X_cg = 7.9985
Y_cg = 0
Z_cg = 0
Mach = 0.15
AoA = -4,0,4,8,10
Beta = 0
Vinf = 51.0441
Rho = 1.225
ReCref = 80481806.9033
ClMax = -1
MaxTurningAngle = -1
Symmetry = Y
FarDist = -1
NumWakeNodes = -1
WakeIters = 3
NumberOfRotors = 0
Preconditioner = Matrix
Vortex Lift = Y
LE Suction = Y
Karman-Tsien Correction = Y
```

Figure 2.20: Example of a VSPAERO setup file.

A thing that has to be noted is that the value of X_{cg}, Y_{cg}, and Z_{cg} are the coordinates of the pole of the moment coefficient. The value of the Mach number is only used for compressibility correction. VSPAERO has two options for compressibility corrections: a 2nd order Karman-Tsien correction and a 1st order Prandlt Glauert correction, the first is the default one.

The `LOD` file is a spanwise representation of the local lift, drag, and side force coefficients. It is useful for plotting the distribution of forces along a wing or body component to locate problem areas, drag sources, peak lifting sections, and slipstream effects. This file will also aid in the refinement of wing planforms if you are trying to find a particular wing loading curve. In Figure 2.21 is provided an example of a load file given by VSPAERO.

```
# Name                  Value      Units
Sref_                 720.1532000 Lunit^2
Cref_                  23.0313000 Lunit
Bref_                  56.2000000 Lunit
Xcg_                    7.9985000 Lunit
Ycg_                    0.0000000 Lunit
Zcg_                    0.0000000 Lunit
Mach_                   0.1500000 no_unit
AoA_                   -4.0000000 deg
Beta_                   0.0000000 deg
Rho_                    1.2250000 Munit/Lunit^3
Vinf_                  51.0441000 Lunit/Tunit
Roll__Rate              0.0000000 rad/Tunit
Pitch_Rate              0.0000000 rad/Tunit
Yaw___Rate              0.0000000 rad/Tunit

   Wing      S       Yavg     Chord     V/Vref     Cl        Cd        Cs        Cx        Cy        Cz        Cmx       Cmy       Cmz
      1   0.11738   0.43272  39.65783   1.00000  -0.14219   0.00994   0.00489  -0.00577   0.00489  -0.14213  -0.00155   0.03956   0.00261
      1   0.24519   1.29139  38.50083   1.00000  -0.14744   0.00896   0.01135  -0.00614   0.01135  -0.14737  -0.00486   0.04174   0.00619
      1   0.26687   2.13869  36.56883   1.00000  -0.15015   0.00753   0.01549  -0.00674   0.01549  -0.15005  -0.00871   0.04248   0.00852
      1   0.29006   2.98054  34.19124   1.00000  -0.15458   0.00638   0.01763  -0.00731   0.01763  -0.15444  -0.01345   0.04463   0.00988
      1   0.31439   3.82165  31.61870   1.00000  -0.16015   0.00512   0.01866  -0.00777   0.01866  -0.16000  -0.01941   0.04826   0.01083
      1   0.33949   4.66494  28.94967   1.00000  -0.16779   0.00464   0.01977  -0.00841   0.01977  -0.16761  -0.02719   0.05384   0.01207
      1   0.36524   5.51265  26.20325   1.00000  -0.17765   0.00399   0.02088  -0.00929   0.02088  -0.17744  -0.03766   0.06197   0.01378
      1   0.39167   6.36650  23.39674   1.00000  -0.19108   0.00396   0.02247  -0.01022   0.02247  -0.19083  -0.05247   0.07458   0.01628
      1   0.41872   7.22580  20.55497   1.00000  -0.20829   0.00334   0.02420  -0.01146   0.02420  -0.20800  -0.07396   0.09342   0.01982
      1   0.44628   8.08736  17.71035   1.00000  -0.23222   0.00336   0.02640  -0.01308   0.02640  -0.23187  -0.10719   0.12379   0.02536
      1   0.47415   8.94751  14.90005   1.00000  -0.26438   0.00242   0.02890  -0.01528   0.02890  -0.26396  -0.16056   0.17252   0.03383
      1   0.50203   9.80397  12.23972   1.00000  -0.31009   0.00312   0.03199  -0.01806   0.03199  -0.30959  -0.25122   0.25686   0.04734
      1   0.52933  10.65650   9.99521   1.00000  -0.36326   0.00160   0.03370  -0.02152   0.03370  -0.36264  -0.39132   0.38401   0.06663
      1   0.55518  11.50574   8.50977   1.00000  -0.41188   0.00345   0.03475  -0.02477   0.03475  -0.41115  -0.56157   0.53536   0.08248
      1   0.58133  12.50014   7.75721   1.00000  -0.44391   0.00370   0.03526  -0.02688   0.03526  -0.44312  -0.72041   0.65965   0.09710
      1   0.61062  13.64345   7.27149   1.00000  -0.46180   0.00683   0.03672  -0.02799   0.03672  -0.46097  -0.87262   0.77394   0.11557
      1   0.64177  14.78669   6.78577   1.00000  -0.47682   0.00680   0.03795  -0.02920   0.03795  -0.47594  -1.04634   0.90106   0.13701
      1   0.67292  15.92986   6.30005   1.00000  -0.49171   0.00772   0.03914  -0.03024   0.03914  -0.49079  -1.25203   1.05046   0.16189
      1   0.70407  17.07295   5.81434   1.00000  -0.50231   0.00610   0.03999  -0.03168   0.03999  -0.50132  -1.48514   1.21627   0.19184
      1   0.73522  18.21593   5.32862   1.00000  -0.51583   0.00644   0.04110  -0.03279   0.04110  -0.51480  -1.77550   1.42581   0.22787
      1   0.76637  19.35875   4.84290   1.00000  -0.52900   0.00623   0.04225  -0.03512   0.04225  -0.52784  -2.12879   1.67955   0.27702
      1   0.79752  20.50139   4.35719   1.00000  -0.54155   0.00589   0.04327  -0.03652   0.04327  -0.54032  -2.56508   1.99058   0.33371
      1   0.82867  21.64376   3.87147   1.00000  -0.55198   0.00480   0.04420  -0.03860   0.04420  -0.55063  -3.10607   2.37570   0.40933
      1   0.85982  22.78574   3.38575   1.00000  -0.56229   0.00383   0.04505  -0.04080   0.04505  -0.56081  -3.80839   2.87253   0.50865
      1   0.89097  23.92715   2.90003   1.00000  -0.57573   0.00450   0.04629  -0.04378   0.04629  -0.57408  -4.77984   3.56530   0.65275
      1   0.92212  25.06765   2.41432   1.00000  -0.57700   0.00300   0.04642  -0.04499   0.04642  -0.57526  -6.02812   4.44385   0.83061
      1   0.95327  26.20653   1.92860   1.00000  -0.56555   0.00238   0.04561  -0.04563   0.04561  -0.56374  -7.73245   5.64267   1.08265
      1   0.98442  27.34219   1.44288   1.00000  -0.50320   0.00205   0.04054  -0.04167   0.04054  -0.50151  -9.59687   6.92935   1.35653


Comp      Component-Name                    Mach      AoA       Beta      CL        CDi       CS        CFx       CFy       CFz       Cmx       Cmy       Cmz
1         wing                              0.15000  -4.00000   0.00000  -0.12891   0.00292   0.01185  -0.00735   0.01185  -0.12871  -0.02453   0.06666   0.00478
```

Figure 2.21: Example of a VSPAERO `LOD` file.

In the `STAB` file relies the responses after a stability calculation. After the angle of attack is set to 0, the responses are calculated when a delta of one unit is imposed. Also the stability derivative can be found. In Figure 2.22 is provided an example of a stab file given by VSPAERO.

```
# Name                  Value      Units
Sref_                 720.1532000 Lunit^2
Cref_                  23.0313000 Lunit
Bref_                  56.2000000 Lunit
Xcg_                    7.9985000 Lunit
Ycg_                    0.0000000 Lunit
Zcg_                    0.0000000 Lunit
Mach_                   0.1500000 no_unit
AoA_                    0.0000000 deg
Beta_                   0.0000000 deg
Rho_                    1.2250000 Munit/Lunit^3
Vinf_                  51.0441000 Lunit/Tunit
Roll__Rate              0.0000000 rad/Tunit
Pitch_Rate              0.0000000 rad/Tunit
Yaw___Rate              0.0000000 rad/Tunit

#
Case                   Delta    Units        CFx         CFy         CFz         CMx         CMy         CMz         CL          CD          CS          CMl         CMm         CMn
#
Base_Aero              +0.000 n/a          0.0004925   -0.0000018  -0.0572191  -0.0000005   0.0525809  -0.0000006  -0.0572191   0.0004376  -0.0000018   0.0000005   0.0525809   0.0000006
Alpha                  +1.000 deg          0.0002429   -0.0000004  -0.0066126   0.0000011   0.0320736  -0.0000001  -0.0066159   0.0001809  -0.0000004  -0.0000011   0.0320736   0.0000001
Beta                   +1.000 deg          0.0004648   -0.0004492  -0.0569958   0.0007142   0.0526367  -0.0001592  -0.0569958   0.0004380  -0.0004410  -0.0007142   0.0526367   0.0001592
Roll__Rate             +1.000 rad/Tunit   -0.0994812   -0.0260273  -0.0501422   0.1010604   0.0404269  -0.0073916  -0.0501422   0.0288590  -0.0260273  -0.1010604   0.0404269   0.0073916
Pitch_Rate             +1.000 rad/Tunit   -0.1753694   -0.0002759   0.9367402   0.0000187  -0.4896555  -0.0000738   0.9367402   0.0815818  -0.0002759  -0.0000187  -0.4896555   0.0000738
Yaw___Rate             +1.000 rad/Tunit   -0.0019127    0.0084261  -0.0760946  -0.0091275   0.0776448   0.0030037  -0.0760946   0.0026734   0.0084261   0.0091275   0.0776448  -0.0030037
Mach                   +0.100 no_unit      0.0005026   0.0000020  -0.0575823  -0.0000024   0.0530865   0.0000011  -0.0575823   0.0004473   0.0000020   0.0000024   0.0530865  -0.0000011
#
#
#            Base    Derivative:
#            Aero         wrt         wrt         wrt         wrt         wrt         wrt
Coef         Total       Alpha        Beta           p           q           r       Mach           U
#              -           per         per         per         per         per         per         per
#              -           rad         rad         rad         rad         rad           M           u
#
CFx        0.0004925   -0.0143008   -0.0015829   -0.1816037   -0.7795225   -0.0043690    0.0001013    0.0000152
CFy       -0.0000018    0.0000759   -0.0256369   -0.0472758   -0.0012150    0.0153094    0.0000379    0.0000057
CFz       -0.0572191    2.8995369    0.0127955    0.0128553    4.4058091   -0.0342876   -0.0036321   -0.0005448
CMx       -0.0000005    0.0000898    0.0409468    0.1835788    0.0000852   -0.0165793   -0.0000192   -0.0000029
CMy        0.0525809   -1.1749799    0.0031949   -0.0220779   -2.4035090    0.0455289    0.0050559    0.0007584
CMz       -0.0000006    0.0000322   -0.0090860   -0.0134257   -0.0003244    0.0054575    0.0000171    0.0000026
CL        -0.0572191    2.8993518    0.0127955    0.0128553    4.4058091   -0.0342876   -0.0036321   -0.0005448
CD         0.0004376   -0.0147086    0.0000244    0.0516279    0.3596787    0.0040614    0.0000969    0.0000145
CS        -0.0000018    0.0000759   -0.0251681   -0.0472758   -0.0012150    0.0153094    0.0000379    0.0000057
CMl        0.0000005   -0.0000898   -0.0409468   -0.1835788   -0.0000852    0.0165793    0.0000192    0.0000029
CMm        0.0525809   -1.1749799    0.0031949   -0.0220779   -2.4035090    0.0455289    0.0050559    0.0007584
CMn        0.0000006   -0.0000322   -0.0090860    0.0134257    0.0003244   -0.0054575   -0.0000171   -0.0000026
#
#
#
#
# Result                 Value      Units
SM                     0.4052561 no_unit
X_np                  17.3320745 Lunit
#
#
#
```

Figure 2.22: Example of a VSPAERO `STAB` file.

2.3.3 Design of Experiments

Design of Experiments (DoE) is a powerful tool for identifying a set of process factors (parameters) which are most important to the process and then determine at what levels these factors must be kept to optimize the response (or quality characteristic) of interest, in other words, it is used to find cause-and-effect relationships.

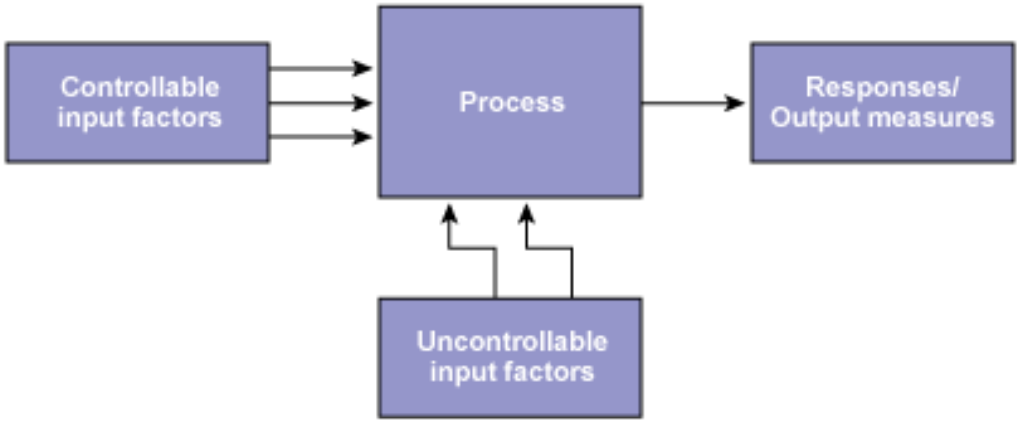

Figure 2.23: Process Factors and Responses.

- *Controllable input factors*, or x factors, are those input parameters that can be modified in an experiment or process;
- *Uncontrollable input factors* are those parameters that cannot be changed;
- *Responses*, or output measures, are the elements of the process outcome that gage the desired effect.

It derives its power from the fact that it helps maximize the information gained from a given number of experiments whilst using a minimum of resources. This is obtained through factorial design, a structured approach based on statistical methods that supports the simultaneous changing of more than one factor at a time. A second advantage of DoE is that it also provides more information than one-change-at-a-time traditional experimental methods, because it allows a judgment on the significance of not only input variables or factors acting alone (main effect), but also factors acting in combination with one another (interactions). This is because, when the factors are changed simultaneously, any influence that one factor has on the other becomes apparent in the resulting response. Any such interaction involving

two- or three-factor is called a "2nd order" or "3rd order" effect respectively, and so on. DoE has another important advantage over traditional methods in that it covers a wider range in the experimental domain (with fewer experiments). This means there is a heightened chance of locating the actual optimal process parameters (real peak) instead of just the best within the limited domain investigated in the one-change-at-a-time methods (false peak).

The DoE strategy usually involves a screening phase followed by an optimization phase. In the screening phase, the vital few factors that have a significant influence on the response are identified. In the optimization phase, where the focus is only on the already identified vital few factors, further refinement is applied to the selection of factors and their ranges.

There are some important differences between the DoE concepts applicable to numerical experiments and those relevant to physical experiments. These are contrasted below, since such a discussion is scarce to find in the literature. Firstly, in numerical DoE, there is no systematic bias because there are no uncontrollable external factors affecting the results. It is therefore not necessary to randomize the run order. Also, because the simulations are deterministic (same output every time for a given set of inputs), it is not necessary to replicate experiments to reduce the effects of noise factors and/or measurement errors. Finally, since the input quantities in numerical experiments remain the same (unlike in physical experiments where, for example, raw material quality could fluctuate between batches), there is no need to divide the experimental runs into blocks and arithmetically remove the difference to increase the sensitivity of the DoE. At the same time, some limitations of the numerical experiments also should be taken into account. Firstly, the simulation results (responses) will be a strong function of the quality of mathematics coded into the software code. This will determine how well the physics of the process has been captured in the code and how much accuracy is sacrificed to improve calculation efficiency. Secondly, the responses will also be strongly dependent on the quality of the input data for material properties and boundary conditions such as heat transfer coefficients between material interfaces. Therefore, unless realistic values are used, the DoE responses may not be truly representative of the physical process [24].

3

Results Investigation

3.1 Aerodynamic Analysis of the BWB planform

3.1.1 Single case of a BWB planform

Scope of this Chapter is to discuss the aerodynamic calculation implemented by the MATLAB algorithm, which was discussed in Chapter 2.3.1. In this section will be highlighted a single case of a BWB planform generated by the algorithm, as a matter of fact the algorithm is not only designed for a full Design of Experiments but it is possible to point out a smaller group of combinations even a single case.

As we choose a specific combination, the algorithm can output a MATLAB figure with the representation of the BWB planform as a *Surface*, *Plate*, and *Stick*, which are extracted by the the *DegenGeom* output file (Chapter 2.2.2). These representation are shown from Figure 3.1 to 3.3 below. In Figure 3.4 a different *Surface* representation of a BWB planform is shown as a way of highlight how different a planform geometry can be during the Design of Experiments.

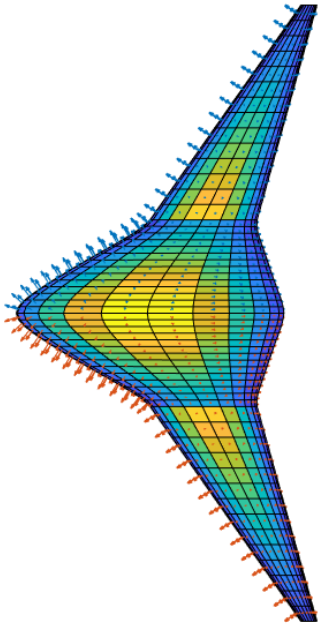

Figure 3.1: Representation of a BWB planform as a surface. MATLAB.

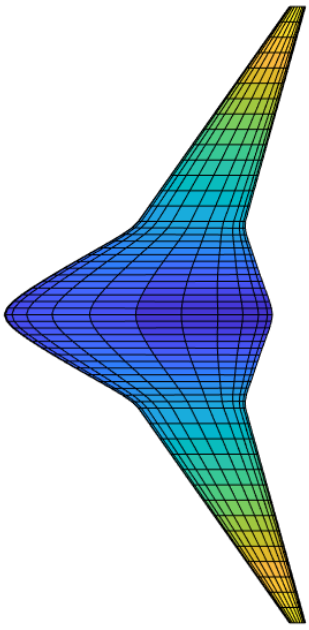

Figure 3.2: Representation of a BWB planform as a plate. MATLAB.

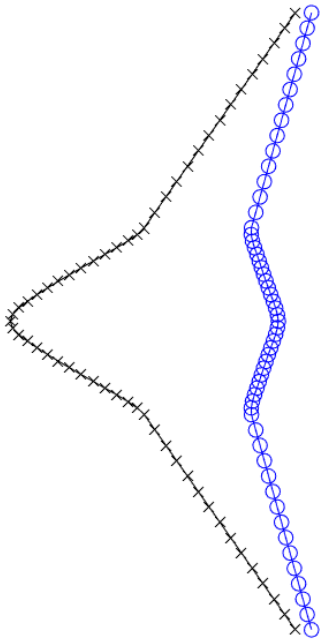

Figure 3.3: Representation of a BWB planform as a stick. MATLAB.

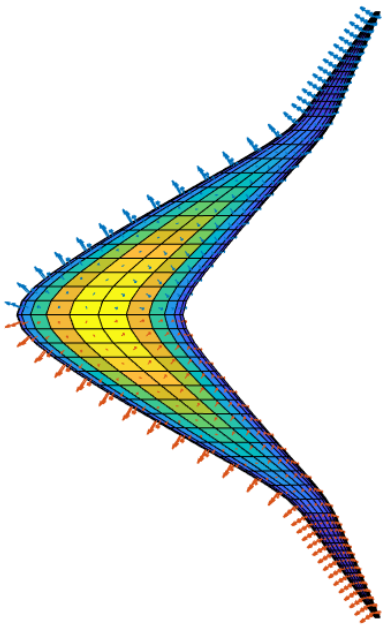

Figure 3.4: Representation of a different BWB planform as a surface. MATLAB.

Other outputs are the plot representations below. In Figure 3.5 the linear region of the aerodynamic lift curve with the variation of angle of attack is shown, also the slope of the curve (C_{L_α}) can be outlined from this plot. In Figure 3.6 the aerodynamic drag polar is represented while in Figure 3.7 the pitching moment coefficient with the variation of angle of attack is represented. Also with this kind of plot the slope of the curve ($C_{\mathcal{M}_\alpha}$) can be outlined. As it can be observed, its value is negative and, together with a positive value of the zero-lift pitching moment coefficient $C_{\mathcal{M}_0}$, an equilibrable and stable condition can be achieved, as described in Chapter 1.1.3. This condition was possible with the second airfoil selection (Chapter 2.2.1) as we extend the Liebeck airfoil from the root to the kink section, while the first airfoil selection not always displayed this desired condition. Lastly, Figure 3.8 represents the profile lift coefficient along the span at different angles of attack.

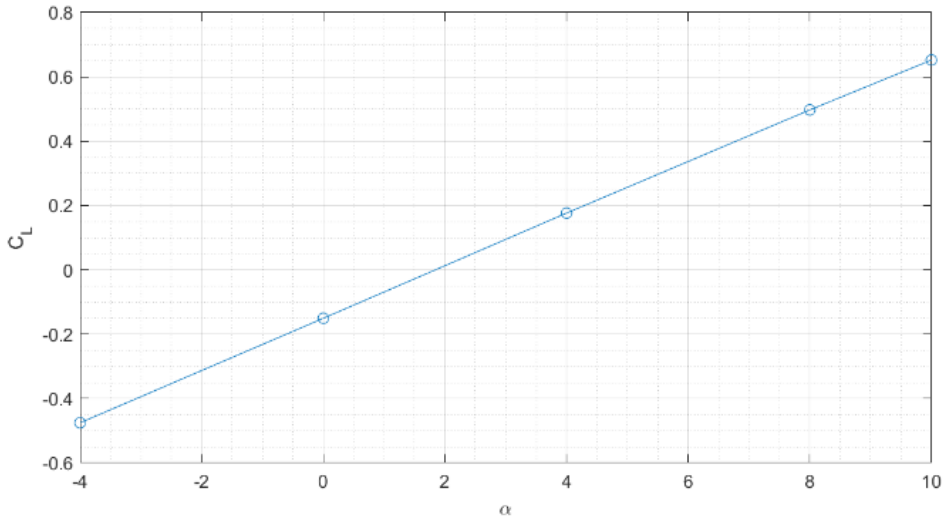

Figure 3.5: Linear region of aerodynamic lift coefficient plot of a BWB planform. MATLAB.

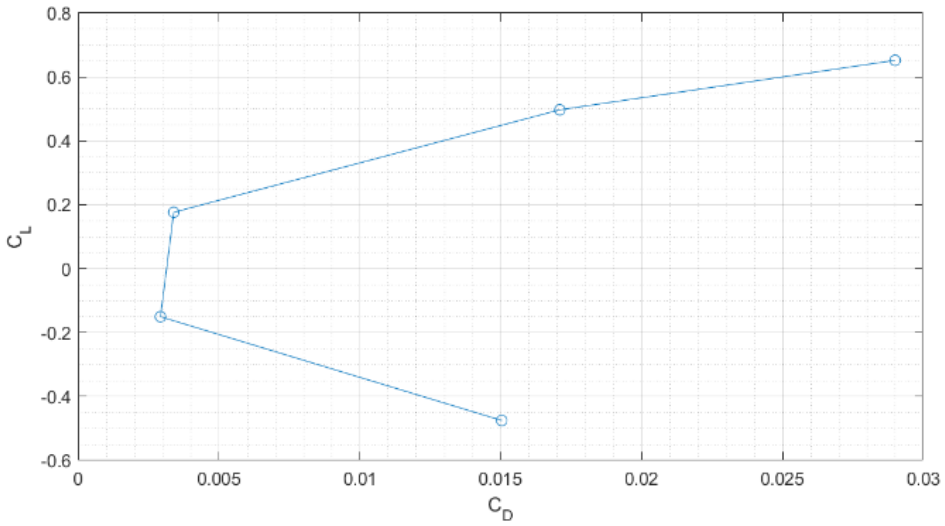

Figure 3.6: Aerodynamic polar plot of a BWB planform. MATLAB.

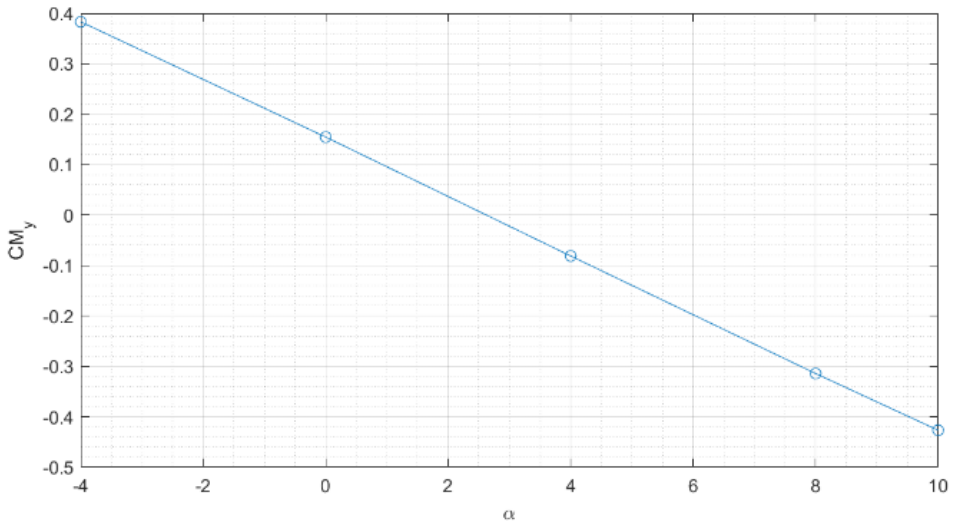

Figure 3.7: Aerodynamic pitching moment coefficient plot of a BWB planform. MATLAB.

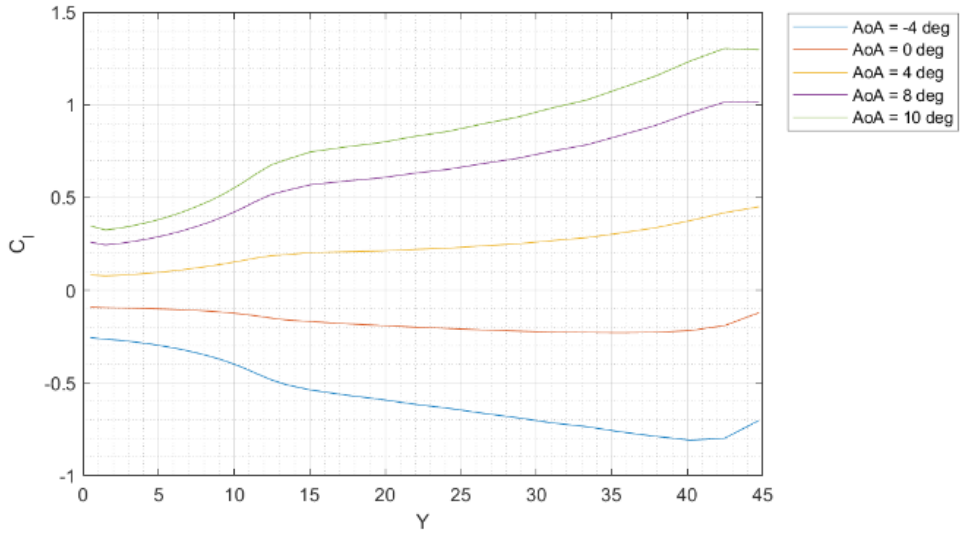

Figure 3.8: Aerodynamic lift coefficient along the span plot of a BWB planform. MATLAB.

3.2 Design of Experiments Analysis

3.2.1 Post Processing Algorithm

While in Section 3.1.1 it was presented how the algorithm can output the aerodynamic results and the related plots, in this section will be inspected the post-processing of the data acquired from the output files (e.g. Chapter 2.3.1). This post-processing work will lead to the DoE analysis and on how the combination of the input specification will effect various aerodynamic responses. A schematic flow chart of the algorithm is provided by Figure 3.9.

The algorithm starts with the selection of spreadsheet `.xlsx` output file from which we want to realize a post-processing analysis. As a matter of fact, all the different calculation runs are divided by the centre of gravity location in relation to the mean aerodynamic chord. In particular the location selected are $x_{\text{cg}}/\text{mac} = 0.15$ - 0.25 - 0.35 as we want to emphasize different behaviours that occurs as we change the location of the centre of gravity. After that, the algorithm enters in a `for` cycle as the data for all the BWB configuration are loaded back in the MATLAB workspace, in particular the algorithm reads the Mach regime of the calculation previously made.

If the Mach number is above the value of 0.6, the algorithm implements a `waveDrag` function employed in a wave drag evaluation for each configuration, as VSPAERO cannot predict this kind of drag. In particular the wave drag coefficient is calculated with the extended Korn equation. The Korn equation can be used to estimate the drag divergence Mach number. This equation has been extended to include sweep using simple sweep theory. The result is presented given by:

$$M_{DD} = \frac{\kappa_A}{\cos\Lambda} - \frac{(t/c)}{\cos^2\Lambda} - \frac{C_l}{10\cos^3\Lambda} \tag{3.1}$$

This model estimates the drag divergence Mach number as a function of an airfoil technology factor κ_{A}, the thickness-to-chord ratio t/c, the lift coefficient C_l, and the sweep angle Λ. In particular the airfoil technology factor is different for each kind of airfoil and its value are 0.89 for the root section, 0.91 for the kink section, and 0.95 for the tip section, after that a linear interpolation is made in order to find the Korn technology factor distribution along the span. Moreover thickness-to-chord ratio, lift coefficient and sweep angle distribution are calculated from the loaded data.

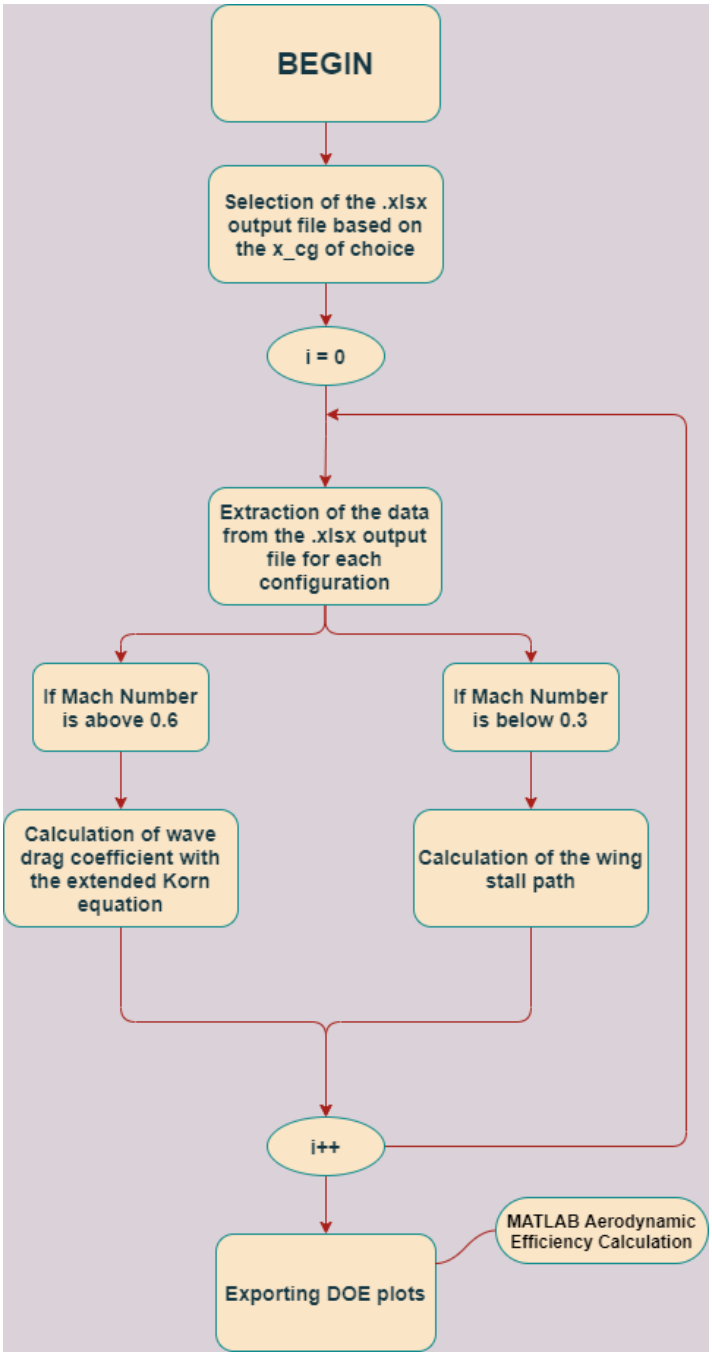

Figure 3.9: MATLAB DoE algorithm flow chart.

With this approximation for the drag divergence Mach number, we can now calculate the critical Mach number. The definition of the drag divergence Mach number is taken to be:

$$\frac{\partial C_D}{\partial M} \;=\; 0.1 \tag{3.2}$$

Next, making use of Lock's proposed empirically-derived shape of the drag rise [25]

$$C_D \;=\; 20\,(M - M_{\text{crit}})^4 \tag{3.3}$$

The definition of the drag divergence Mach number is equated to the derivative of the drag rise formula given above to produce the following equation:

$$\frac{\partial C_D}{\partial M} \;=\; 0.1 \;=\; 80\,(M - M_{\text{crit}})^3 \tag{3.4}$$

We can then solve this equation for the critical Mach number where the drag divergence Mach number is given by the extended Korn equation:

$$M_{\text{crit}} \;=\; M_{DD} \;-\; \left(\frac{0.1}{80}\right)^{1/3} \tag{3.5}$$

Once the M_{crit} has been calculated, if the Mach number is above the M_{crit} the profile wave drag coefficient can be calculated with the following relation [26]:

$$C_{d_{\text{wave}}} \;=\; 20\,(M - M_{crit})^4 \;\frac{S_{\text{strip}}}{S_{\text{ref}}} \tag{3.6}$$

Where the local (t/c), C_l, and half-chord sweep angle are specified for a number of spanwise strips of length c and width y along the wing, and the drag of each strip is combined to form the total wave drag. In the equation above, the wave drag for each strip is multiplied by the ratio of the strip area (S_{strip}) to the reference area (S_{ref}).

The BWB wave drag coefficient is then the sum of the profile drag coefficients of each strip:

$$C_{D_{\text{wave}}} = \sum_{i=1}^{n} C_{d_{\text{wave}},i} \tag{3.7}$$

Once the the $C_{D_{\text{wave}}}$ has been calculated, the algorithm comes out of the `for` cycle and the DoE plots are generated. In particular, the evaluation of the aerodynamic efficiency is made as shown below:

$$E = \frac{C_L}{C_{D_0} + C_{D_i} + C_{D_w}} \tag{3.8}$$

where the parasite drag C_{D_0} and the induced drag C_{D_i} are calculated by VSPAERO, while the wave drag C_{D_w} is calculated as shown by Equation (3.7).

Instead, if the Mach number is below the value of 0.3 the algorithm implements an aircraft stall path evaluation, established as the first section along the wing span that reaches the maximum airfoil lift coefficient value ($C_{l_{\text{max}}}$). Since the airfoils employed in the root, kink, and tip sections are known, considering also their different thickness-to-chord ratio and chord length depending on the Design of Experiments combination, it is possible to extract their $C_{l_{\text{max}}}$ value, in this case XFOIL software [27] was employed for the task, and subsequently perform a linear interpolation to obtain the $C_{l_{\text{max}}}$ trend along the span. From the C_l values at the highest angle of attack, at which the aerodynamic analysis was made, obtained from the `.lod` file (e.g. Chapter 2.3.2), the lift distribution is scaled until at least one profile achieve its own $C_{l_{\text{max}}}$ value. When the distance between the C_l and $C_{l_{\text{max}}}$ curves along the span gets to zero, such section location is considered as the starting point of the wing stall path. Two examples of this process are proposed in Figure 3.10 and 3.11, where in the former the stall begins in the tip region, while in the latter we have a *centre-body* start for the stall process.

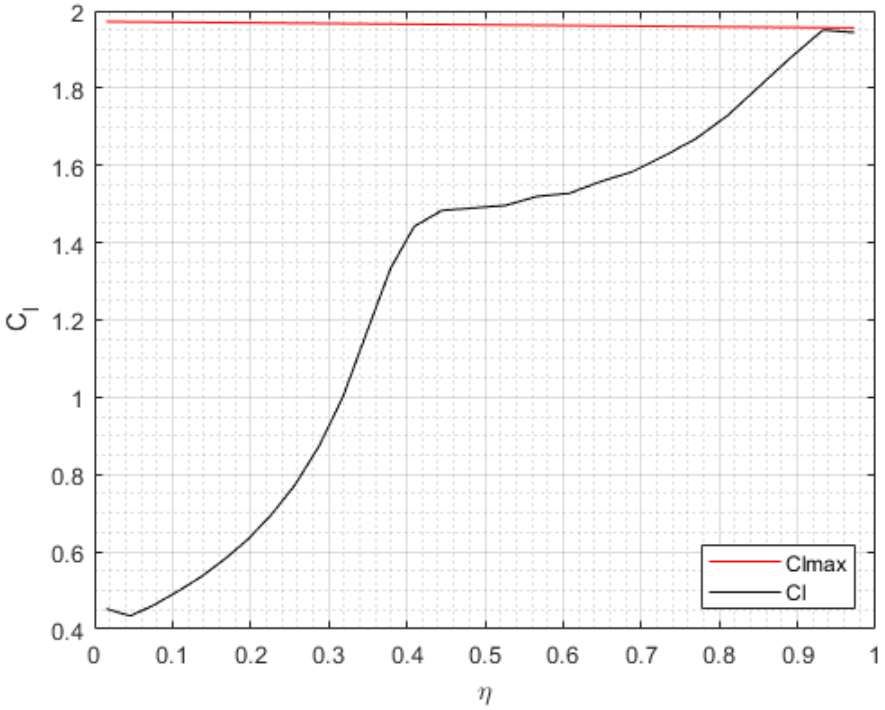

Figure 3.10: Example of the Wing Stall Path process with a tip start for a BWB aircraft combination. MATLAB.

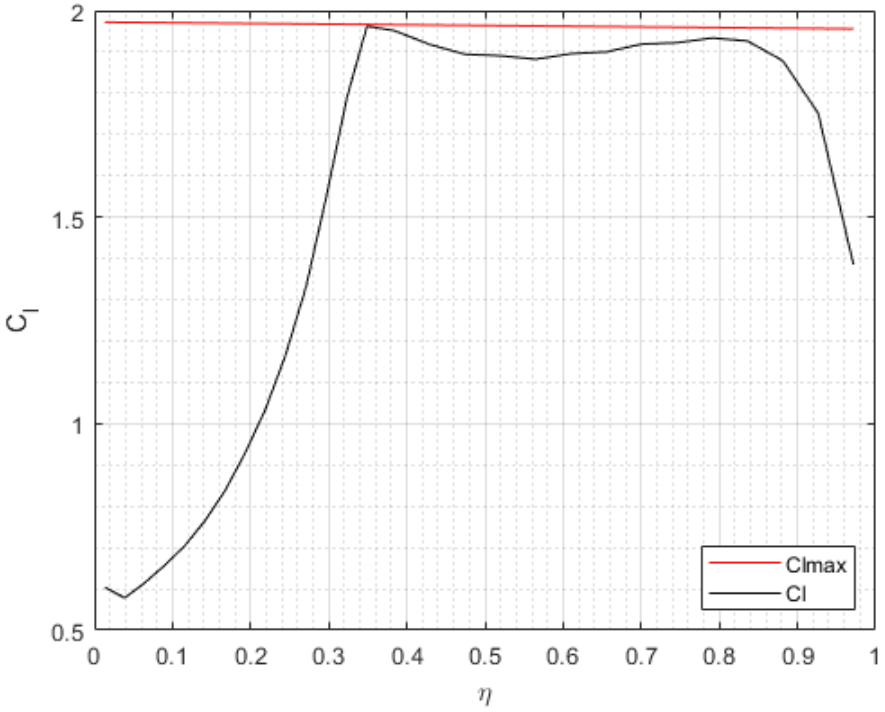

Figure 3.11: Example of the Wing Stall Path process with a *centre-body* start for a BWB aircraft combination. MATLAB.

Once the the stall path section location has been calculated, the algorithm comes out of the `for` cycle and the DoE plots are generated to which a location percentage along the span plot has been added compared to the high Mach number case. Since the $C_{D_{\text{wave}}}$ contribution is negligible for Mach number below the value of 0.3, the aerodynamic efficiency is calculated as shown below:

$$E = \frac{C_L}{C_{D_0} + C_{D_i}} \tag{3.9}$$

3.2.2 DoE interaction plots investigation on the Second Design of Experiments at high subsonic regime

In this section the results of the second Design of Experiments will be presented. It is important to underline that the same calculation made for this Design of Experiments, which data are summarized in Table 2.2, were also made for the first Design of Experiments (Table 2.1). The reason why the results for the first Design of Experiments are omitted is that they exhibit the same patterns of results found also for the second Design of Experiments but at the same time, as in first case the range between the minimum and maximum value for the specification is lower, they display these patterns less clear than the second case.

This calculation is meant to recreate a cruise condition in high subsonic regime. The cruise Mach number is set at $M = 0.82$, the altitude at $h = 10000\,\text{m}$ and the angles of attack range vary from $-2°$ to $6°$ with a $2°$ step for each calculation while the sideslip angle is set to 0. Since the Mach number is above the value of 0.6, the wave drag evaluation seen in Section 3.2.1 is implemented in the aerodynamic efficiency calculation. Also the results for each centre of gravity location are presented.

The chosen outputs for this kind of investigation are the Aerodynamic Efficiency E, the Pitching Moment Coefficient at zero lift angle of attack $C_{\mathcal{M}_0}$ and the Wing Lift Slope coefficient C_{L_α}. In addition, the stability calculation, implemented with a variation of one unit for the angle of attack and sideslip, shows longitudinal, directional, and lateral stability results with the Pitching Moment Coefficient gradient respect angle of attack $C_{\mathcal{M}_\alpha}$, the Yaw Moment Coefficient gradient respect angle of sideslip $C_{\mathcal{N}_\beta}$, and the Roll Moment Coefficient gradient respect angle of sideslip $C_{\mathcal{L}_\beta}$.

The DoE interaction plots for each of the investigated responses presents values of the response or dependent variable on the y-axis while the x-axis shows the values of

the first independent variable. Meanwhile, the various lines represent values of the second independent variable, in particular the blue line represents the minimum input value, while the green line represents the maximum input value (Table 2.2). The interaction plot is a matrix plot, with the number of rows and columns both equal to the number of the input variables. The input variable names are printed on the diagonal of the plot matrix. The plot at off-diagonal position (i, j) is the interaction of the two variables whose names are given at row diagonal (i, i) and column diagonal (j, j), respectively. On an interaction plot, parallel lines indicate that there is no interaction effect while different slopes suggest that one might be present. In a very strong interaction the lines tend to be nearly perpendicular, an interaction where the lines cross is sometimes called an "interference" or "antagonistic" interaction effect. An interaction where the lines depart the interaction effect is sometimes called a "reinforcement" or "synergistic" interaction effect. In general the goal is to identify the 2-factor interaction that has the largest shift that is determined by the steepest line, this defines the "most important factor". Furthermore will be identified the interaction with the next largest shift and so the "second most important factor" and then continue for the remaining factors.

Prior to the diverse aerodynamic response interaction plots, in Figure 3.12 the interaction plot of the reference wing area S_{ref} is presented. This specification isn't obtained from an aerodynamic analysis and doesn't depend on the center of gravity location but it is clear how the S_{ref} is related to all the aerodynamic responses. The most important input that allow S_{ref} to change are Æ_{in}, Æ_{out}, λ_{in} and λ_{out} because from them the span and the chords of the entire aircraft depend but it is also important to clarify that the most important interaction are between Æ_{out}-λ_{in} and Æ_{out}-λ_{out}, where the two lines tend to cross . To a second grade comes the interaction between Æ_{in}-λ_{in}, Æ_{in}-λ_{out}, and λ_{in}-λ_{out}. Regarding the absolute values of S_{ref}, it varies from a minimum value of about $400\,\text{m}^2$ where Æ and λ are at their minimum value to a maximum value of about $800\,\text{m}^2$ where Æ and λ are at their maximum value. It is important to remember that lower S_{ref} means lower S_{wet} and so higher aerodynamic efficiency E, therefore higher range, endurance and cruise flight speed, allowing to have less DOC and pollution. In contrast higher S_{ref} allows better take-off and landing distance and also more space for control devices allocation, crucial for the BWB certification.

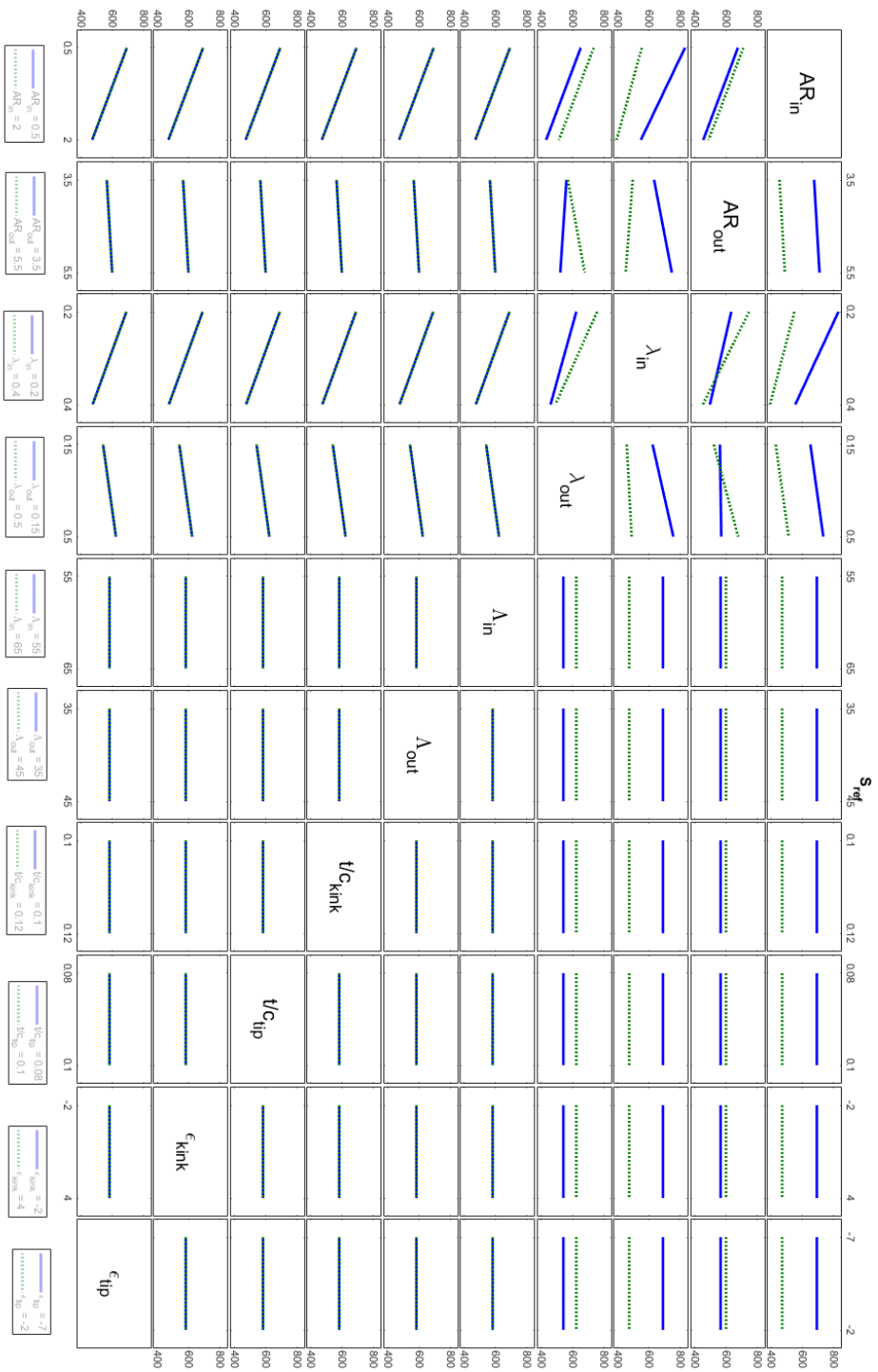

Figure 3.12: DoE interaction plot of the Reference Wing Area (S_{ref}) for the second Design of Experiments. MATLAB.

Results Interpretation

The first result that can be seen from the plots above-listed is that E, $C_{\mathcal{M}_0}$, and C_{L_α} do not depend on the center of gravity location. This result is connected to the untrimmed condition in which the aerodynamic analyses have been conducted. Reflex airfoils in the *centre-body* region act as benefit for equilibrium load, given the lack of an horizontal tail, especially for most forward x_{cg} position. For this reason the effect of the x_{cg} location can be evaluated only on the longitudinal, directional, and lateral stability contributions ($C_{\mathcal{M}_\alpha}$, $C_{\mathcal{N}_\beta}$, and $C_{\mathcal{L}_\beta}$ respectively).

In Figure 3.14 - 3.20 - 3.26 is presented the DoE interaction plots of the aerodynamic efficiency E. It is clear how a greater $\mathcal{AR}$ can increase the value of E, not only with a lower S but also with a greater span b which approaches towards an *infinite* wing span. Nevertheless, the most important interactions are between $\mathcal{AR}_{\text{in}}$-λ_{in} and λ_{in}-Λ_{inner}, to a second degree also between $\varepsilon_{\text{kink}}$-$\varepsilon_{\text{tip}}$. The λ_{in}-Λ_{inner} interaction clears that in order to have an higher E, low values of the taper ratio demand less sweep angle, conversely higher values of the taper ratio demand more sweep angle. Finally it is worth to notice that for all combinations the minimum value for E is around 20 and if all the inputs are optimized towards this efficiency, E can reach value of about 30.

In Figure 3.15 - 3.21 - 3.27 is presented the DoE interaction plots of $C_{\mathcal{M}_0}$. The greater variation is given by $\varepsilon_{\text{kink}}$ and ε_{tip}, especially for positive values of $\varepsilon_{\text{kink}}$. It is important to notice that $C_{\mathcal{M}_0}$ also tends toward negative values which are not accepted for stability purpose. Most important interaction is between $\mathcal{AR}_{\text{in}}$-$\varepsilon_{\text{kink}}$: it shows that positive values of $\varepsilon_{\text{kink}}$ can be contemplated with higher values of $\mathcal{AR}_{\text{in}}$. To a second degree come the interaction between $\mathcal{AR}_{\text{in}}$-λ_{in}, $\mathcal{AR}_{\text{in}}$-Λ_{inner}, $\varepsilon_{\text{kink}}$-$\mathcal{AR}_{\text{out}}$, $\varepsilon_{\text{kink}}$-$\Lambda_{\text{inner}}$, $\varepsilon_{\text{kink}}$-$\Lambda_{\text{out}}$, ε_{tip}-$\mathcal{AR}_{\text{out}}$, ε_{tip}-Λ_{inner} and ε_{tip}-Λ_{out}.

In Figure 3.16 - 3.22 - 3.28 is presented the DoE interaction plots of C_{L_α}. Most influential interactions are between $\mathcal{AR}_{\text{in}}$-$\mathcal{AR}_{\text{out}}$, where we know that higher values of $\mathcal{AR}$ imply a greater slope in the C_L vs. α plot but this interaction clears that, for higher values of C_{L_α}, $\mathcal{AR}_{\text{out}}$ has to be to the maximum value, while $\mathcal{AR}_{\text{in}}$ at its minimum and viceversa, $\mathcal{AR}_{\text{in}}$-λ_{in}, $\mathcal{AR}_{\text{in}}$-Λ_{inner} and $\mathcal{AR}_{\text{in}}$-Λ_{outer}.

In Figure 3.17 - 3.23 - 3.29 is presented the DoE interaction plots of $C_{\mathcal{M}_\alpha}$. This time there is also an influence of x_{cg} location, in particular it can be noticed that a larger value of x_{cg}/mac yields a greater range of values for $C_{\mathcal{M}_\alpha}$. In Figure 3.13 it is presented the pitching moment plot $C_{\mathcal{M}_y}$ vs. α for the same BWB configuration

at different x_{cg}/mac percentage. Most influential interactions are between $\mathcal{R}_{in}$-λ_{in}, $\mathcal{R}_{in}$-$\mathcal{R}_{out}$, $\mathcal{R}_{in}$-λ_{out}, $\mathcal{R}_{out}$-λ_{in}, and λ_{in}-λ_{out}.

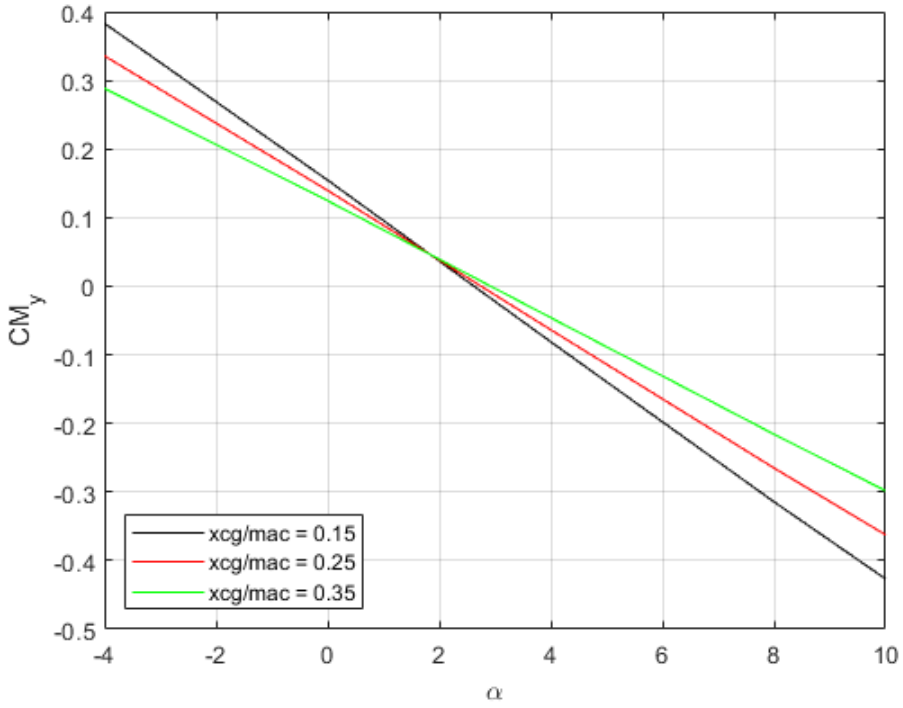

Figure 3.13: Pitching moment coefficient $C_{\mathcal{M}_y}$ of a BWB planform at x_{cg}/mac = 0.15 - 0.25 - 0.35 $M = 0.82$. MATLAB.

In Figure 3.18 - 3.24 - 3.30 is presented the DoE interaction plots of $C_{\mathcal{N}_\beta}$. Also for this response with a higher percentage of x_{cg}/mac comes a greater range of values for $C_{\mathcal{N}_\beta}$. Most influential interactions are between ε_{kink}-$\mathcal{R}_{in}$, ε_{kink}-λ_{in}, ε_{kink}-λ_{out}, in a less degree compared to the λ_{in} case, ε_{kink}-Λ_{inner}, ε_{kink}-Λ_{outer}, $\mathcal{R}_{in}$-λ_{in}, $\mathcal{R}_{in}$-λ_{out}, $\mathcal{R}_{in}$-Λ_{inner} and λ_{in}-λ_{out}. To a second degree of relevance comes the interaction between ε_{tip} and the same specification in which there is an interaction with ε_{kink}. It is important to point out that $C_{\mathcal{N}_\beta}$ must be negative for the lateral stability taking in the account a *construction* reference axis (Chapter 2.2.2). Moreover, given the lack of a vertical tail for a BWB configuration, the sweep angle contribution on the directional stability becomes crucial.

In Figure 3.19 - 3.25 - 3.31 is presented the DoE interaction plots of $C_{\mathcal{L}_\beta}$. Compared to the $C_{\mathcal{M}_\alpha}$ and $C_{\mathcal{N}_\beta}$ cases, the x_{cg} location didn't show an influence on the values. Most influential interactions are between ε_{kink}-λ_{in}, ε_{kink}-Λ_{outer}, $\mathcal{R}_{in}$-λ_{in}, $\mathcal{R}_{in}$-Λ_{inner}, ε_{tip}-$\mathcal{R}_{in}$, ε_{tip}-$\mathcal{R}_{out}$, ε_{tip}-λ_{in} and ε_{tip}-λ_{out}. By taking in consideration the *construction* reference axis, the value of $C_{\mathcal{L}_\beta}$ has to be negative for lateral stability.

Centre of gravity at 15% of mac

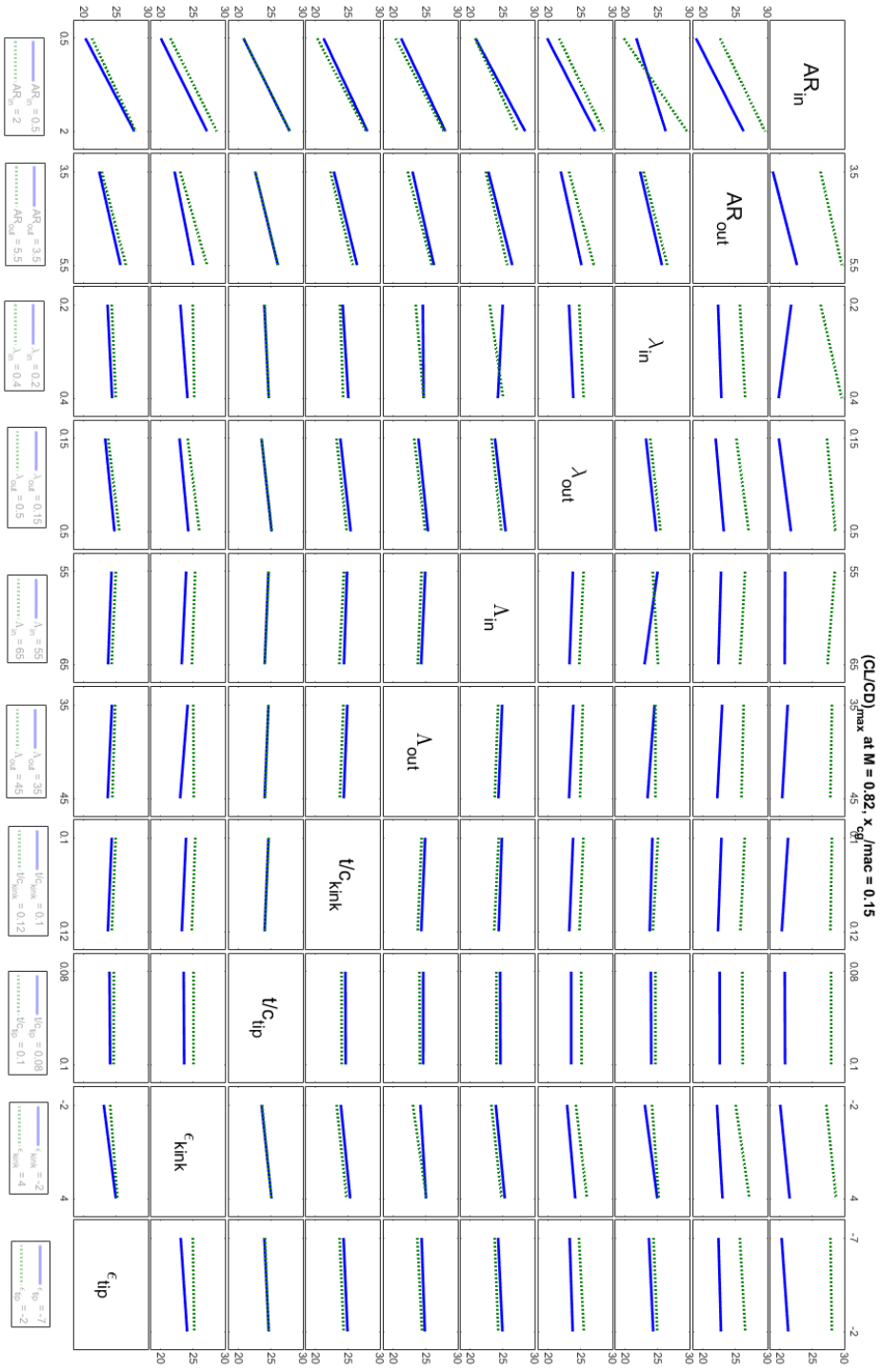

Figure 3.14: DoE interaction plot of the Aerodynamic Efficiency (E) for the second Design of Experiments at $x_{\text{cg}}/\text{mac} = 0.15$ $M = 0.82$. MATLAB.

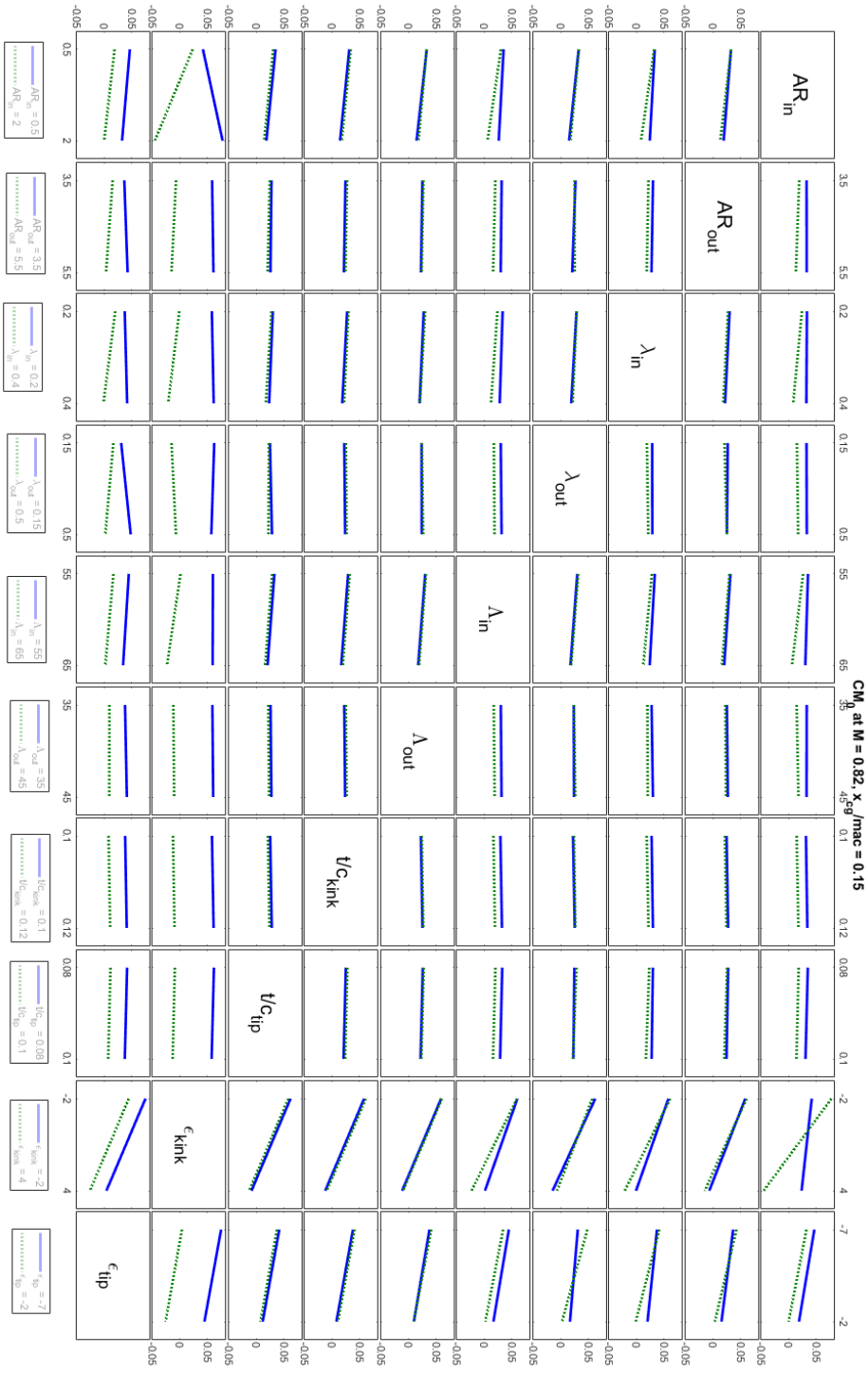

Figure 3.15: DoE interaction plot of the Pitching Moment Coefficient at zero lift angle of attack ($C_{\mathcal{M}_0}$) for the second Design of Experiments at $x_{\text{cg}}/\text{mac} = 0.15$ $M = 0.82$. MATLAB.

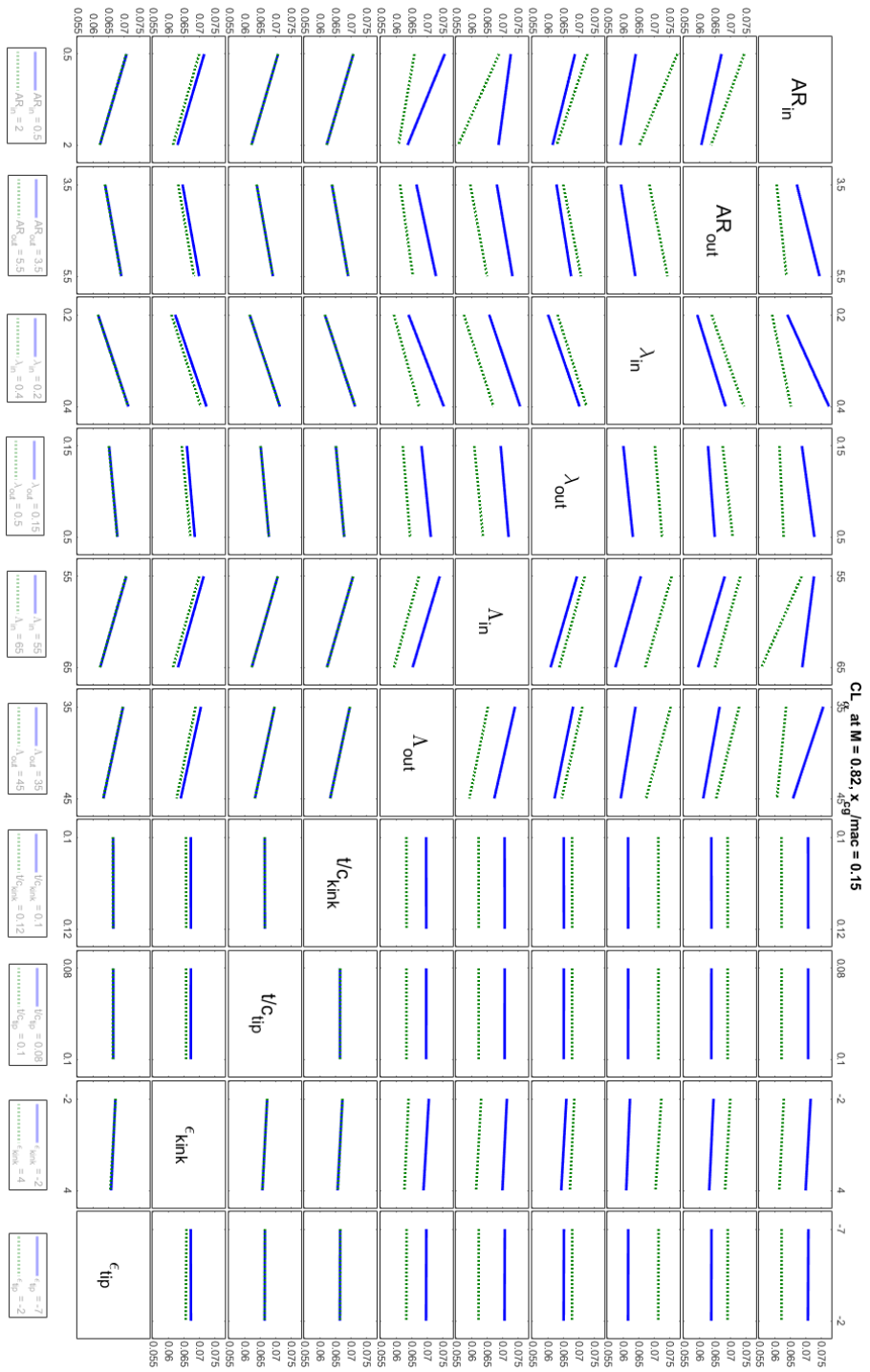

Figure 3.16: DoE interaction plot of the Wing Lift Slope coefficient (C_{L_α}) for the second Design of Experiments at $x_{\text{cg}}/\text{mac} = 0.15$ $M = 0.82$. MATLAB.

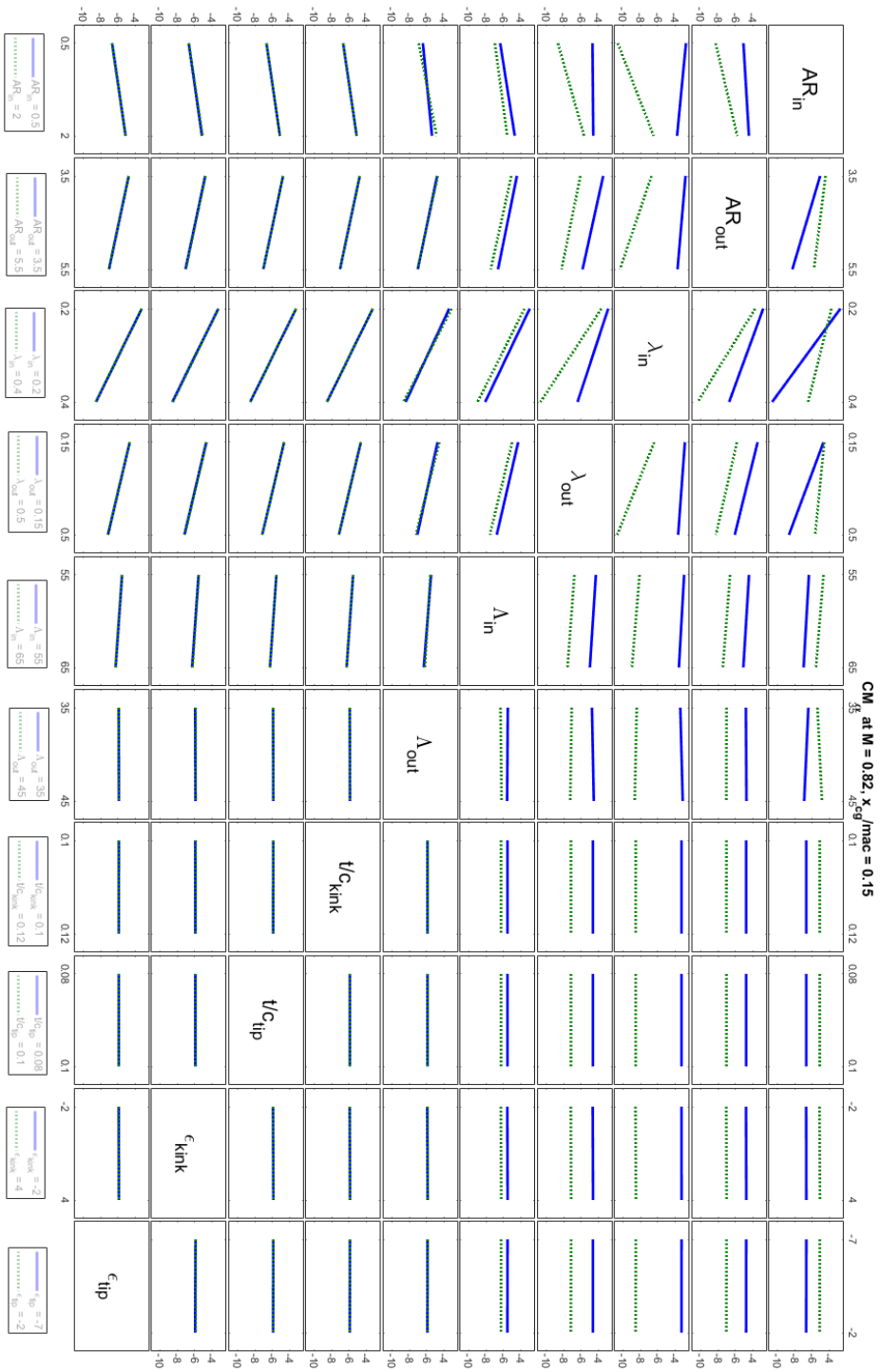

Figure 3.17: DoE interaction plot of the Pitching Moment Coefficient gradient respect angle of attack ($C_{\mathcal{M}_\alpha}$) for the second Design of Experiments at $x_{\text{cg}}/\text{mac} = 0.15$ $M = 0.82$. MATLAB.

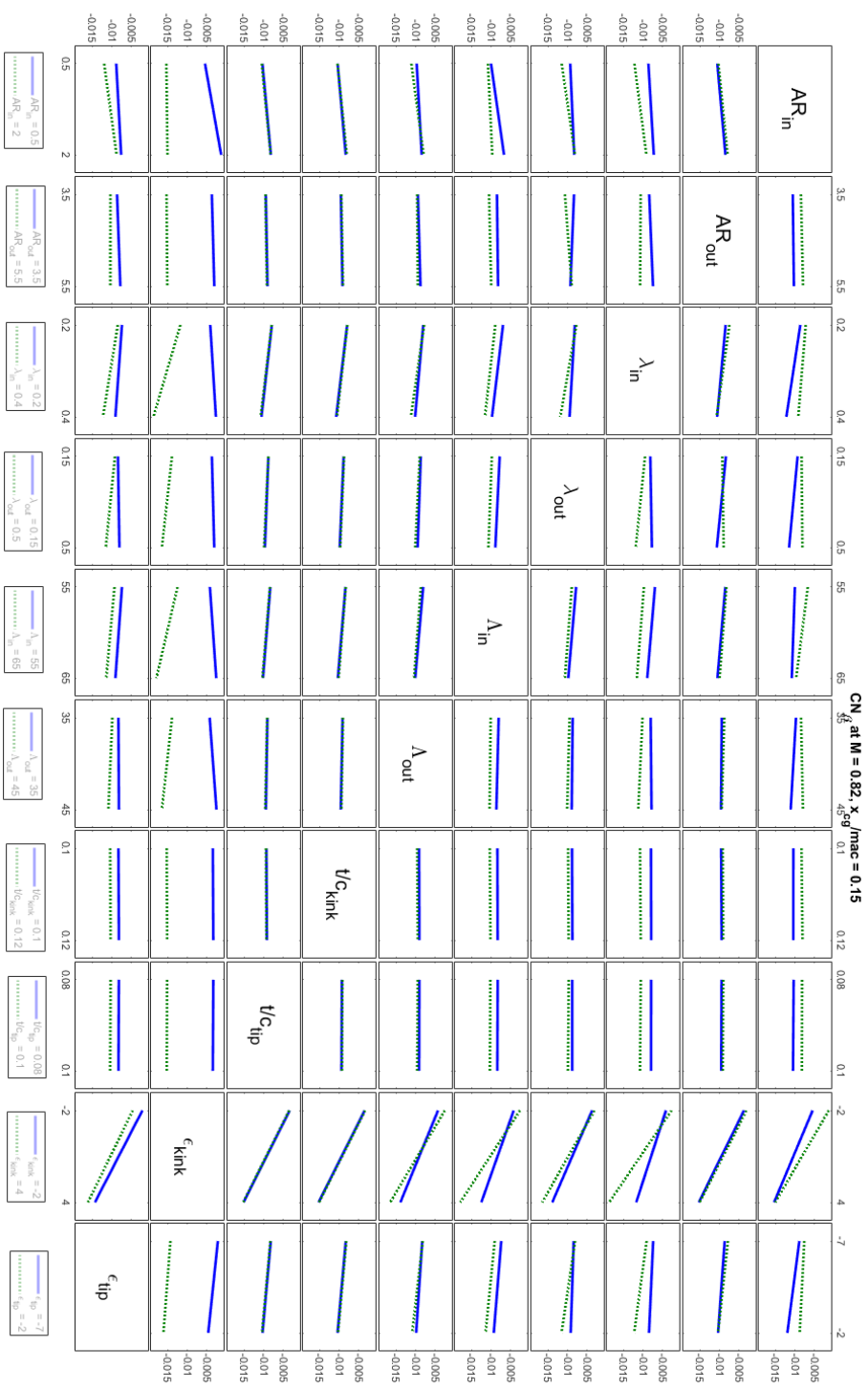

Figure 3.18: DoE interaction plot of the Yaw Moment Coefficient gradient respect angle of sideslip ($C_{\mathcal{N}_\beta}$) for the second Design of Experiments at $x_{\text{cg}}/\text{mac} = 0.15$ $M = 0.82$. MATLAB.

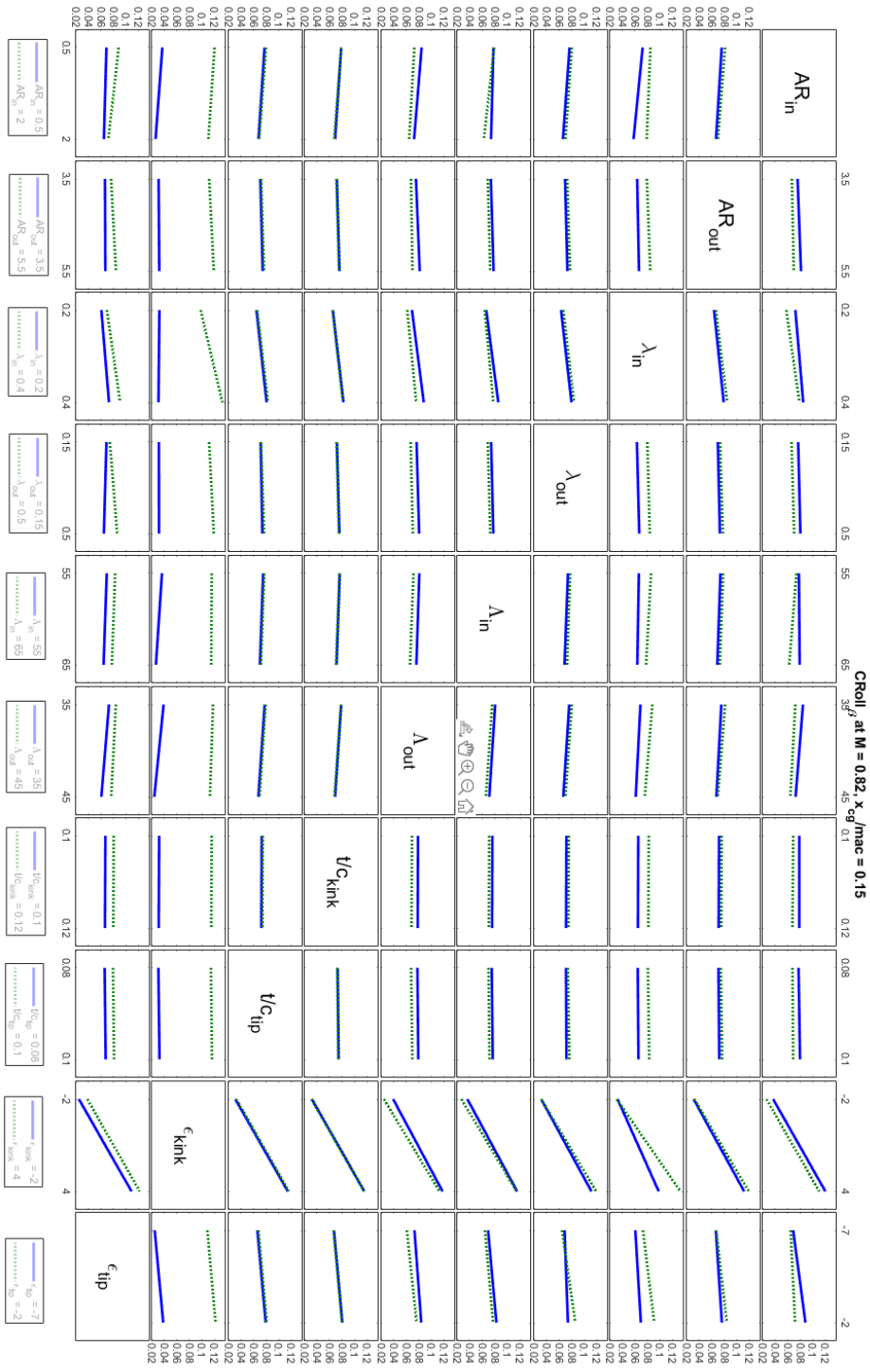

Figure 3.19: DoE interaction plot of the Roll Moment Coefficient gradient respect angle of sideslip ($C_{\mathcal{L}_\beta}$) for the second Design of Experiments at $x_{cg}/\text{mac} = 0.15$ $M = 0.82$. MATLAB.

Centre of gravity at 25% of mac

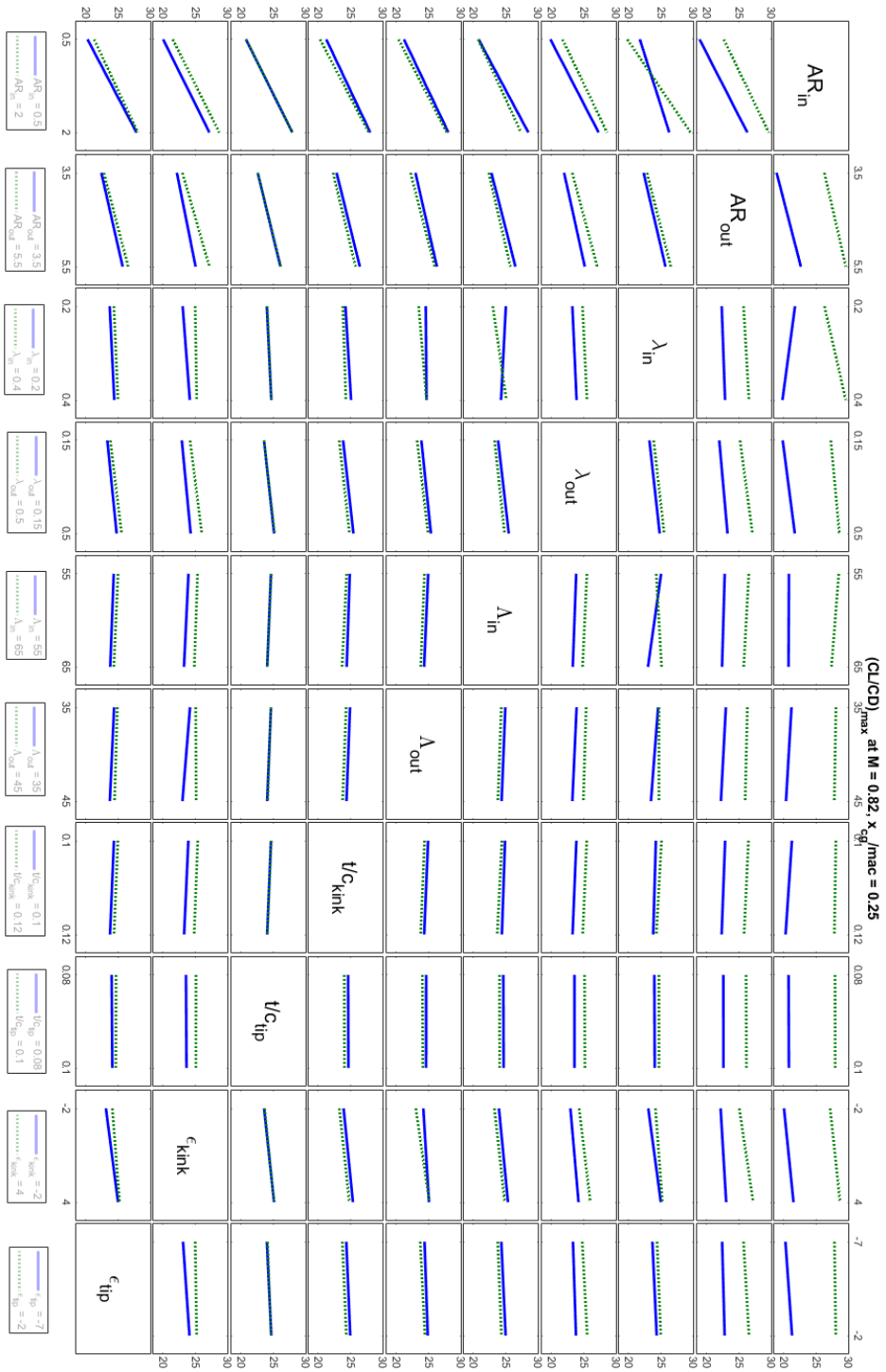

Figure 3.20: DoE interaction plot of the Aerodynamic Efficiency (E) for the second Design of Experiments at $x_{\text{cg}}/\text{mac} = 0.25$ $M = 0.82$. MATLAB.

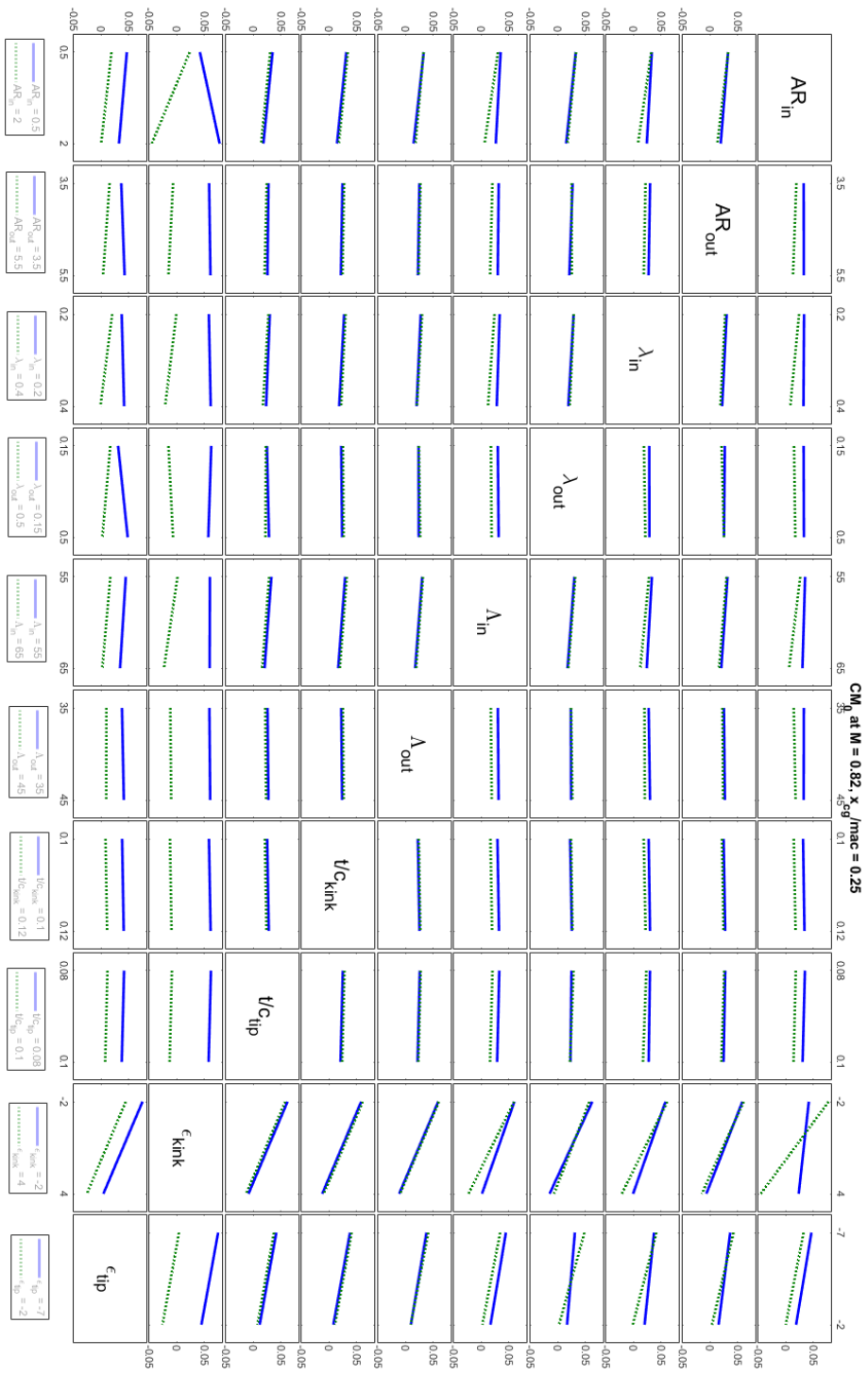

Figure 3.21: DoE interaction plot of the Pitching Moment Coefficient at zero lift angle of attack ($C_{\mathcal{M}_0}$) for the second Design of Experiments at $x_{\text{cg}}/\text{mac} = 0.25$ $M = 0.82$. MATLAB.

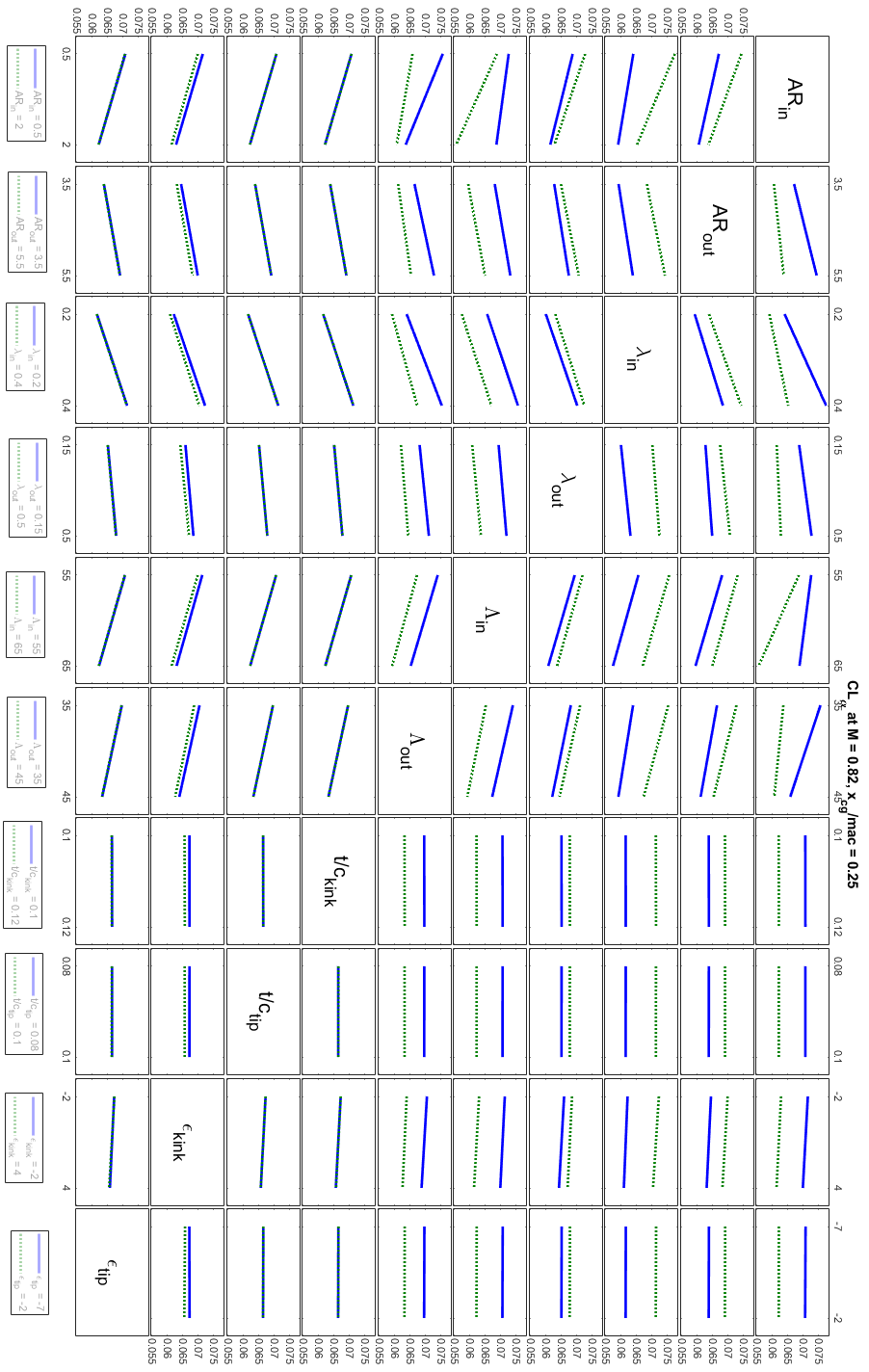

Figure 3.22: DoE interaction plot of the Wing Lift Slope coefficient (C_{L_α}) for the second Design of Experiments at $x_{\text{cg}}/\text{mac} = 0.25$ $M = 0.82$. MATLAB.

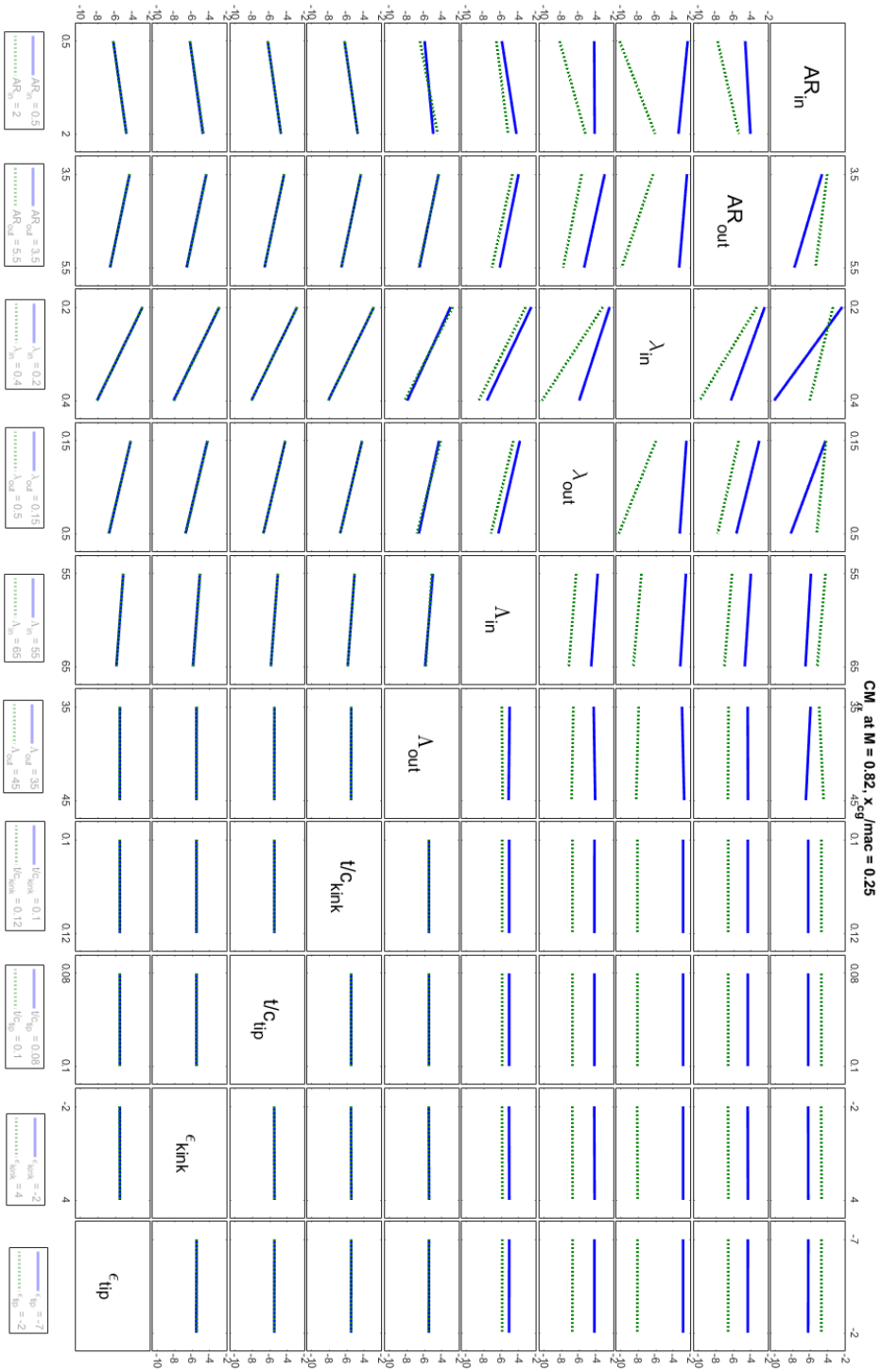

Figure 3.23: DoE interaction plot of the Pitching Moment Coefficient gradient respect angle of attack ($C_{\mathcal{M}_\alpha}$) for the second Design of Experiments at $x_{\text{cg}}/\text{mac} = 0.25$ $M = 0.82$. MATLAB.

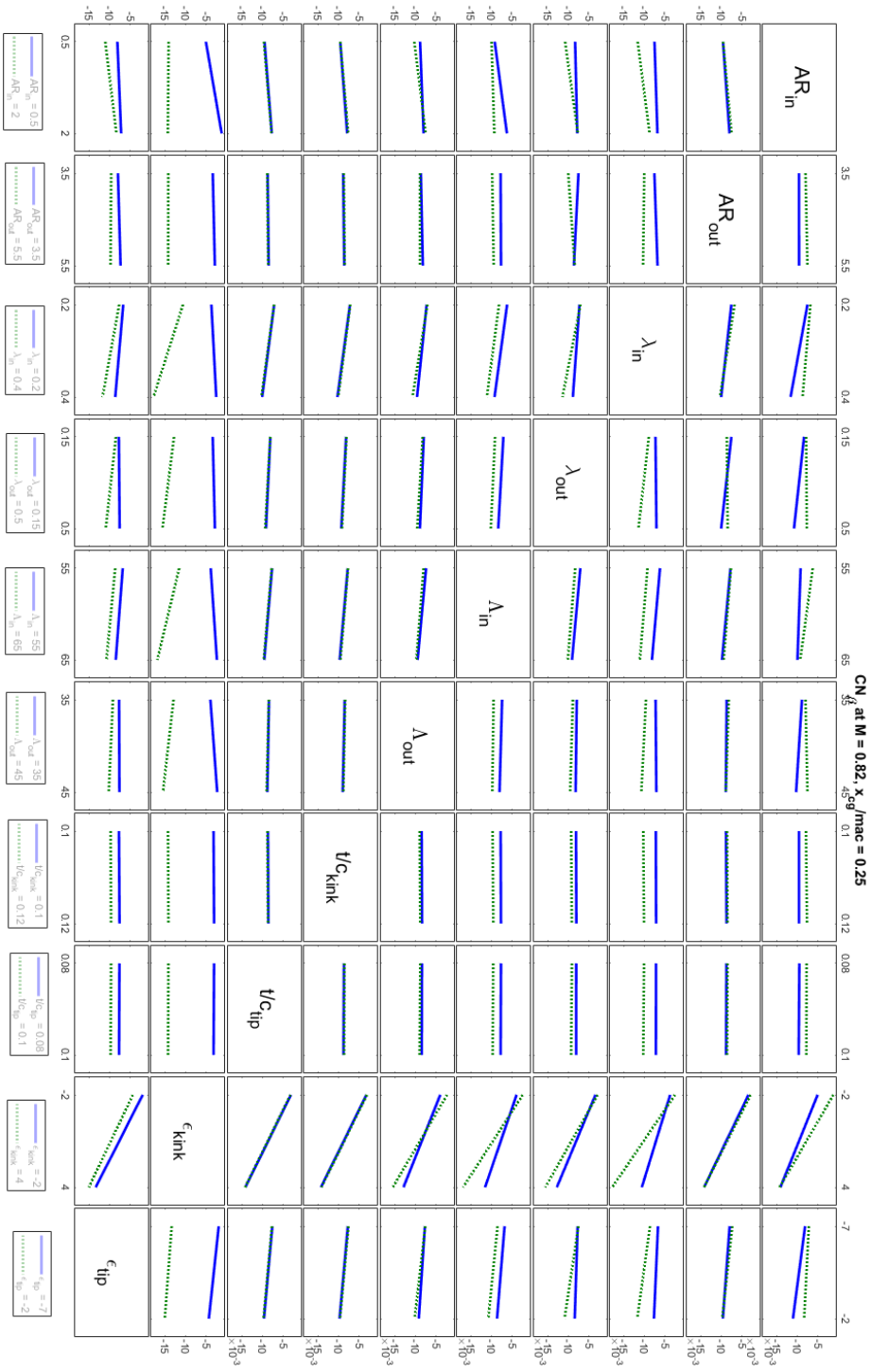

Figure 3.24: DoE interaction plot of the Yaw Moment Coefficient gradient respect angle of sideslip ($C_{\mathcal{N}_\beta}$) for the second Design of Experiments at $x_{\text{cg}}/\text{mac} = 0.25$ $M = 0.82$. MATLAB.

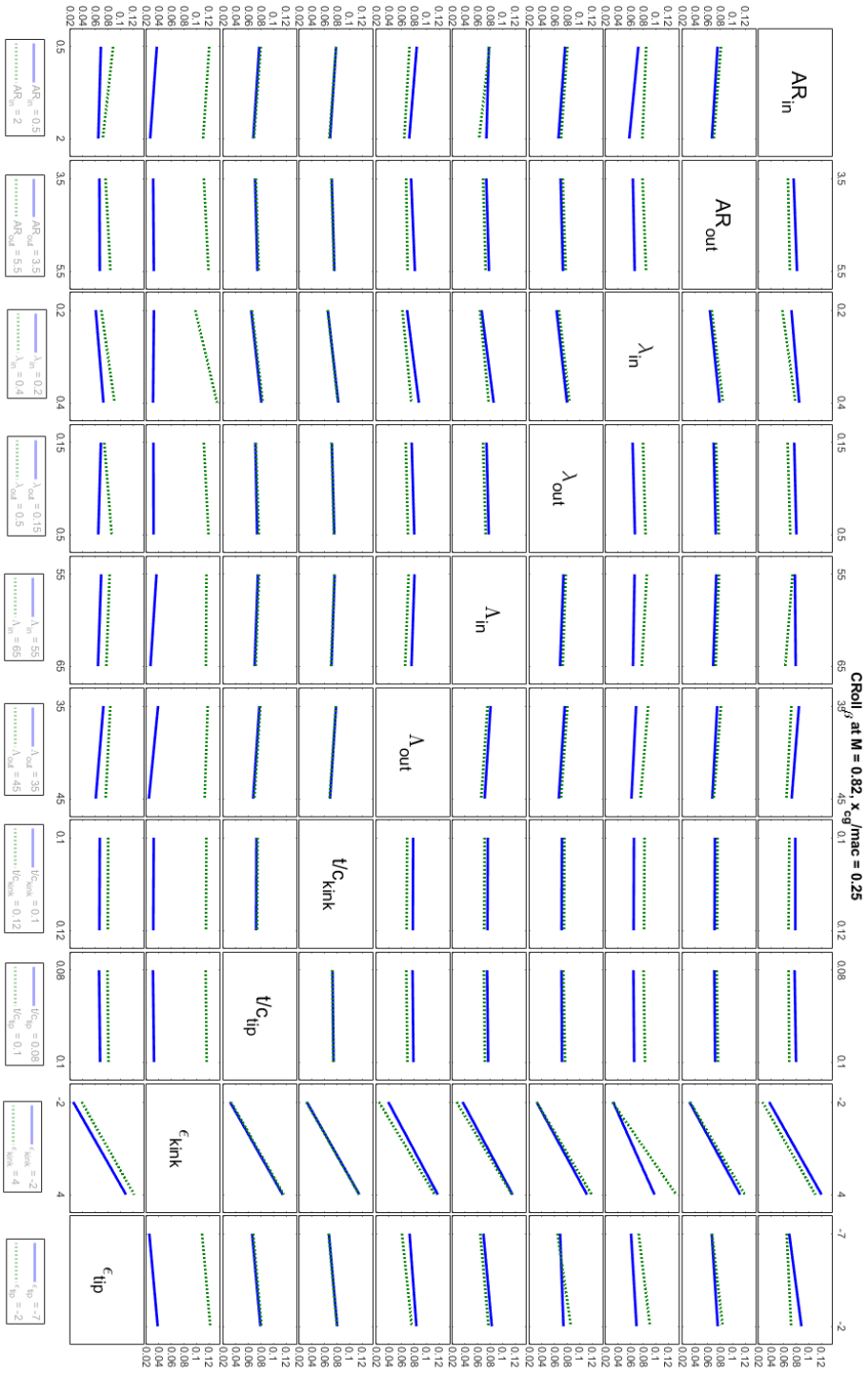

Figure 3.25: DoE interaction plot of the Roll Moment Coefficient gradient respect angle of sideslip ($C_{\mathcal{L}_\beta}$) for the second Design of Experiments at $x_{\text{cg}}/\text{mac} = 0.25$ $M = 0.82$. MATLAB.

Centre of gravity at 35% of mac

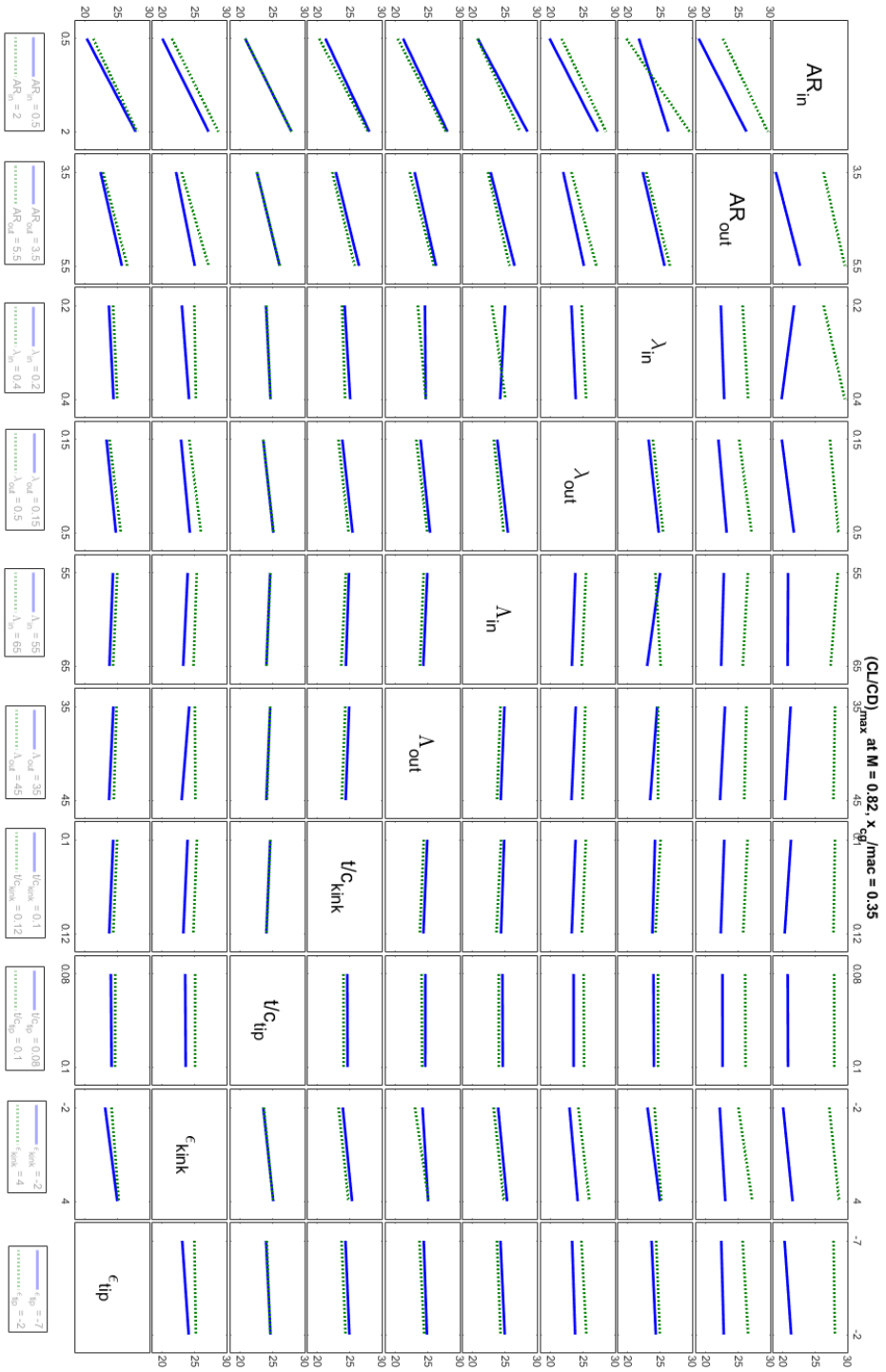

Figure 3.26: DoE interaction plot of the Aerodynamic Efficiency (E) for the second Design of Experiments at $x_{\text{cg}}/\text{mac} = 0.35$ $M = 0.82$. MATLAB.

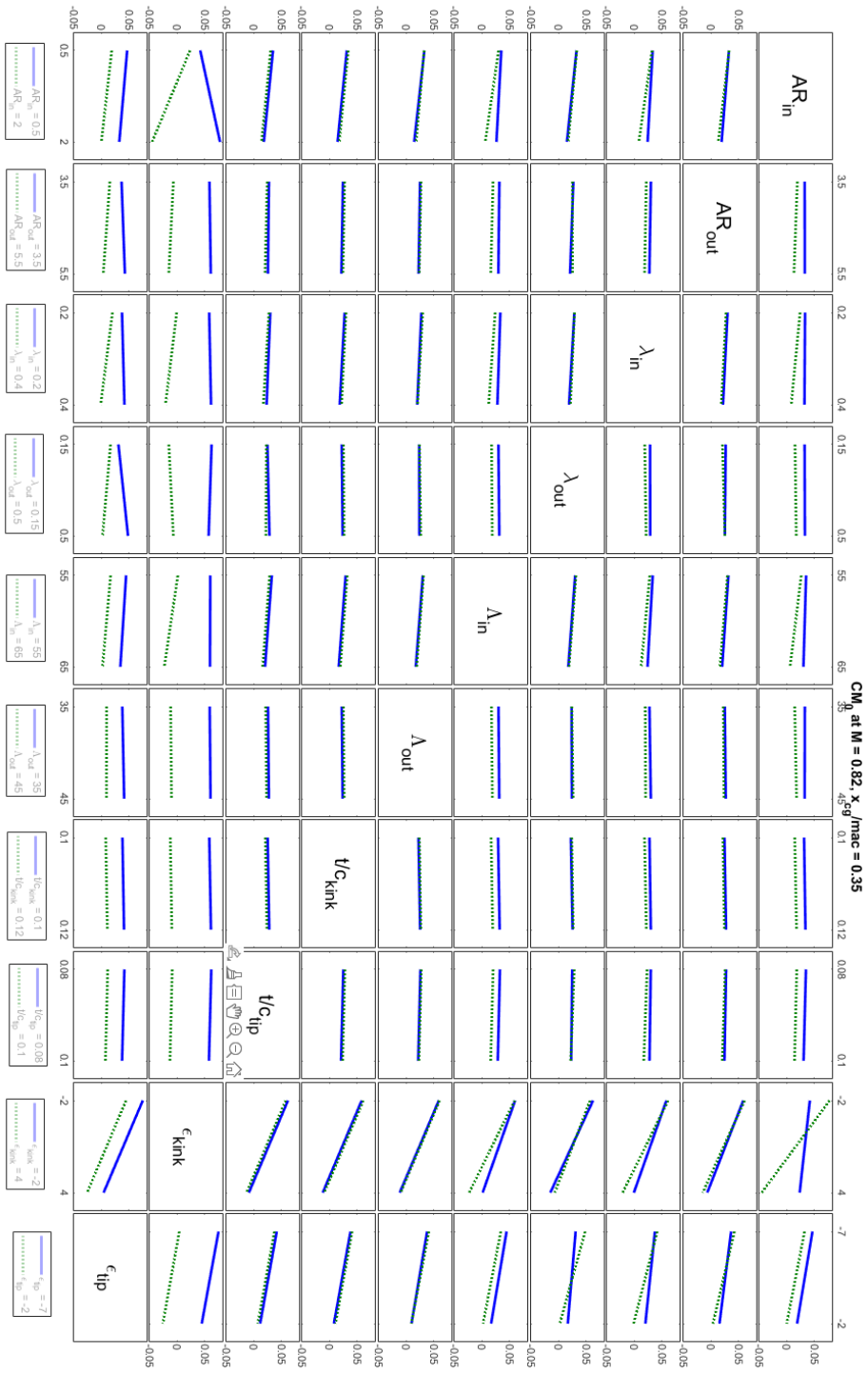

Figure 3.27: DoE interaction plot of the Pitching Moment Coefficient at zero lift angle of attack ($C_{\mathcal{M}_0}$) for the second Design of Experiments at $x_{\text{cg}}/\text{mac} = 0.35$ $M = 0.82$. MATLAB.

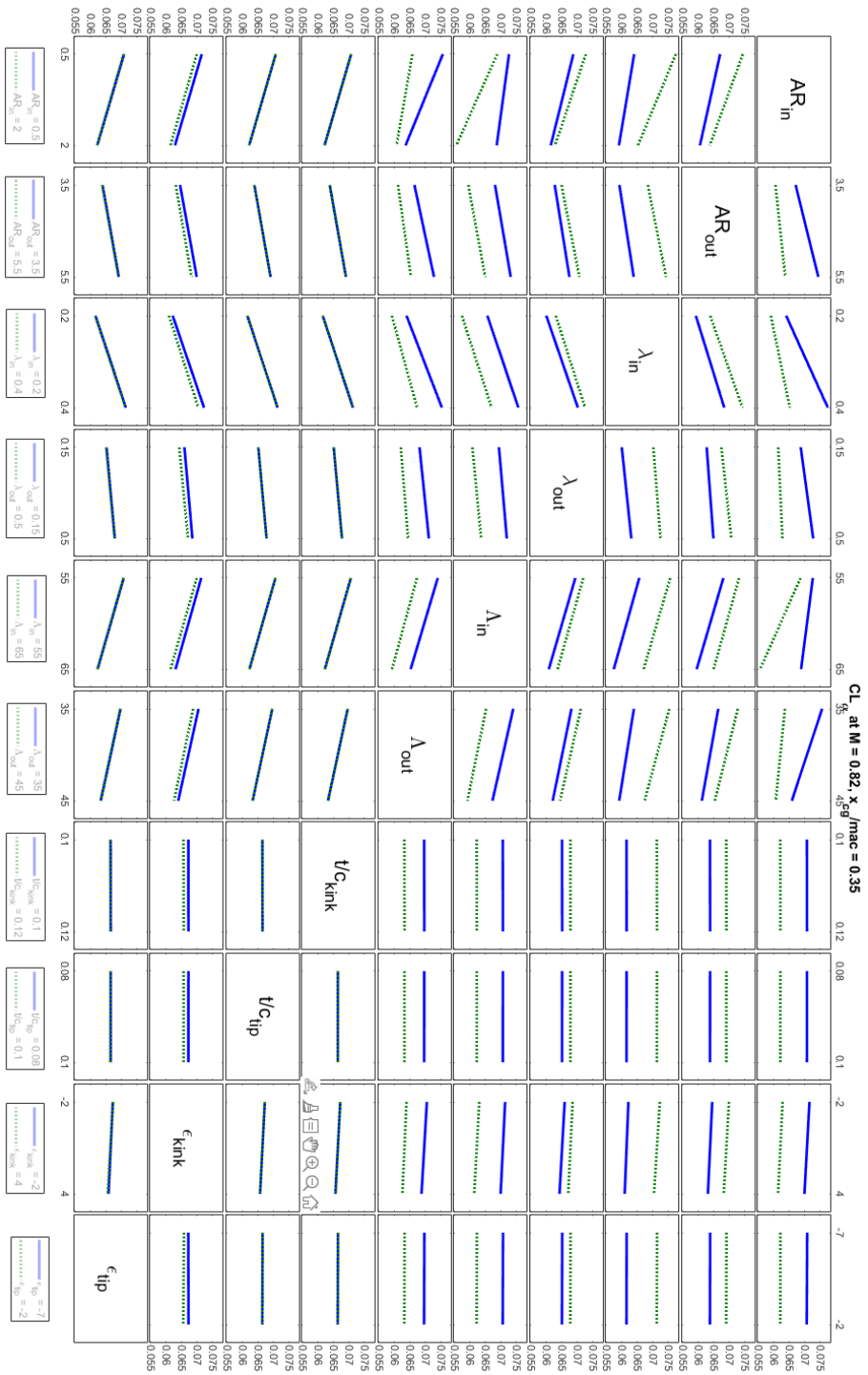

Figure 3.28: DoE interaction plot of the Wing Lift Slope coefficient (C_{L_α}) for the second Design of Experiments at $x_{\text{cg}}/\text{mac} = 0.35$ $M = 0.82$. MATLAB.

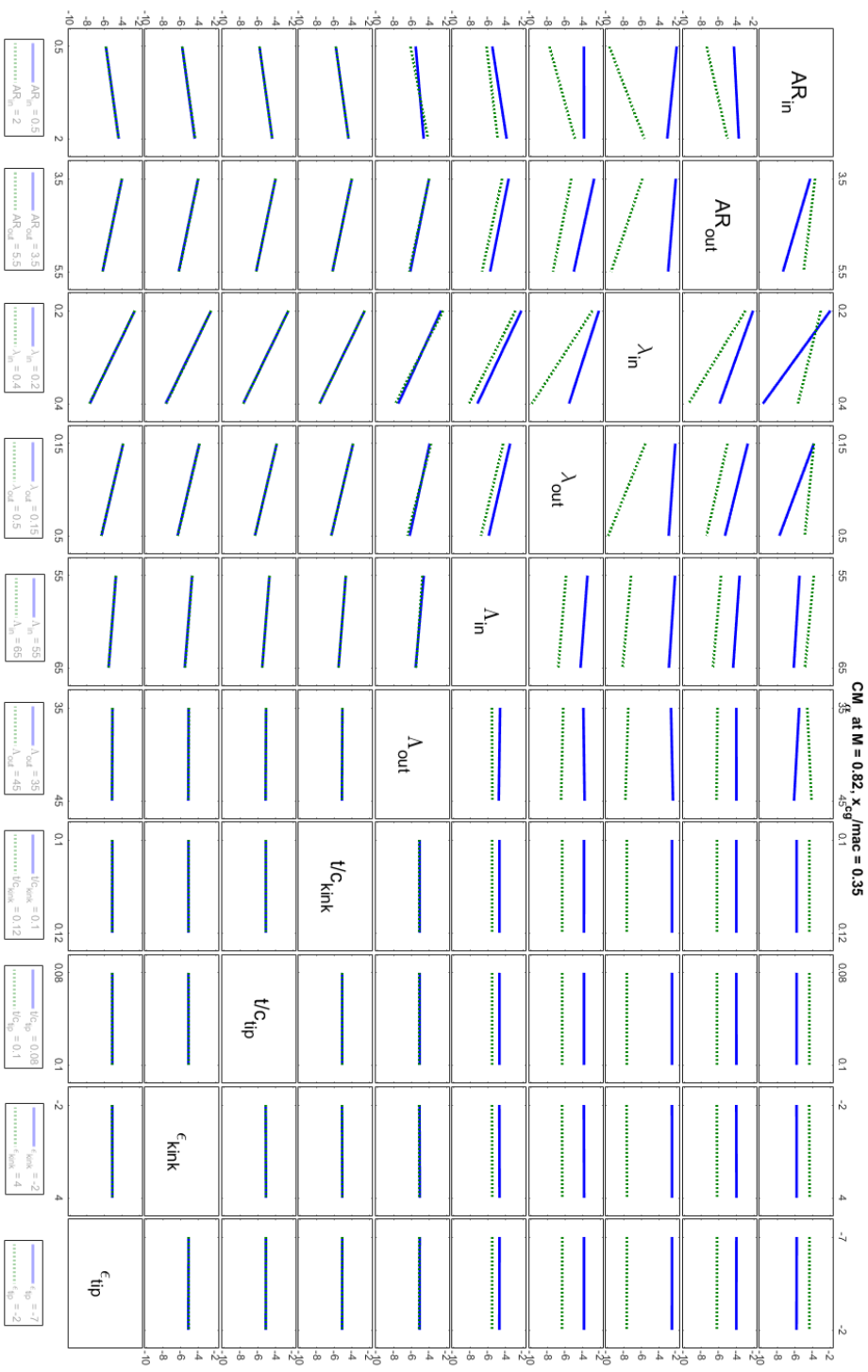

Figure 3.29: DoE interaction plot of the Pitching Moment Coefficient gradient respect angle of attack ($C_{\mathcal{M}_\alpha}$) for the second Design of Experiments at $x_{\text{cg}}/\text{mac} = 0.35$ $M = 0.82$. MATLAB.

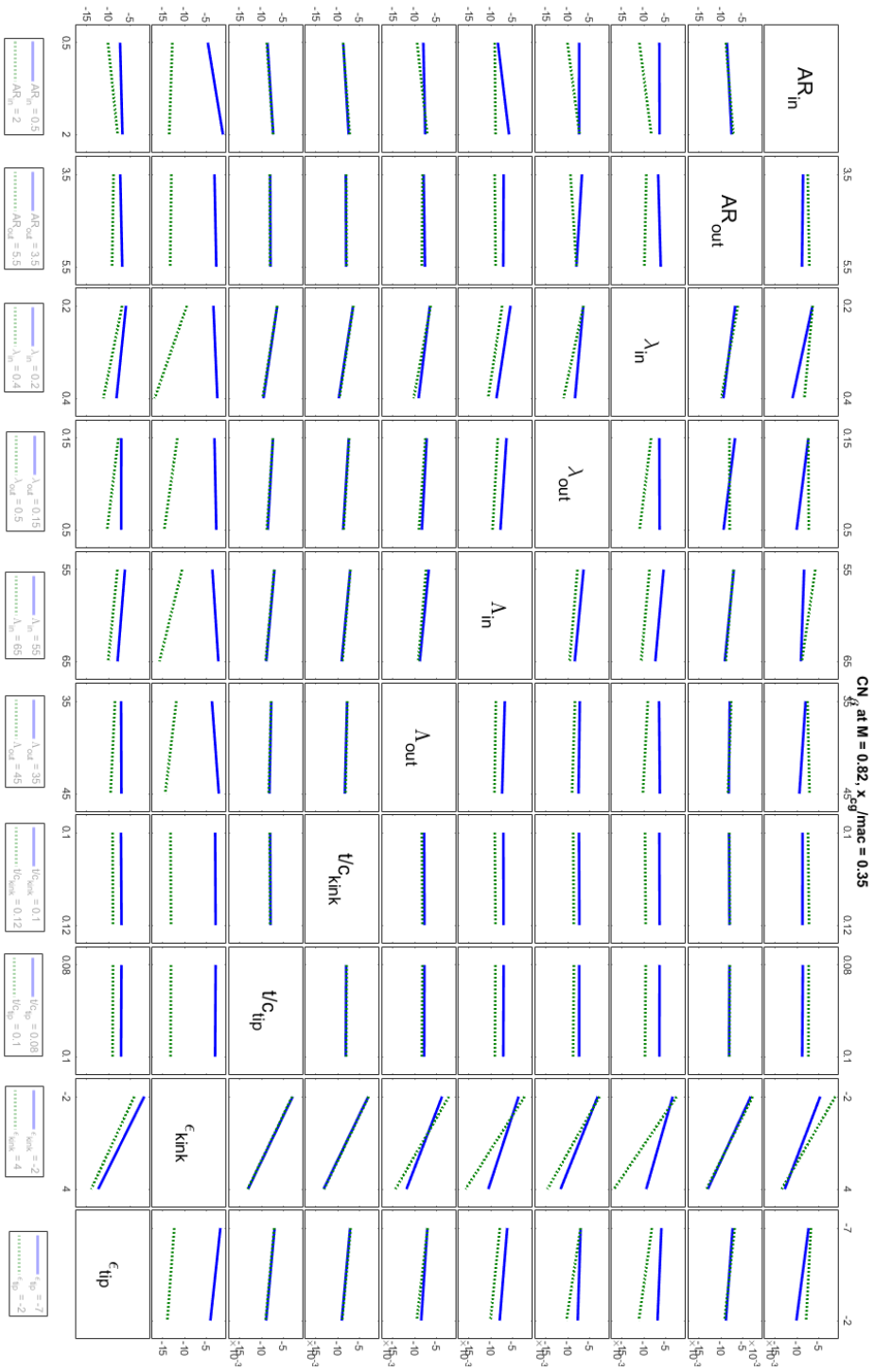

Figure 3.30: DoE interaction plot of the Yaw Moment Coefficient gradient respect angle of sideslip ($C_{\mathcal{N}_\beta}$) for the second Design of Experiments at $x_{cg}/\text{mac} = 0.35$ $M = 0.82$. MATLAB.

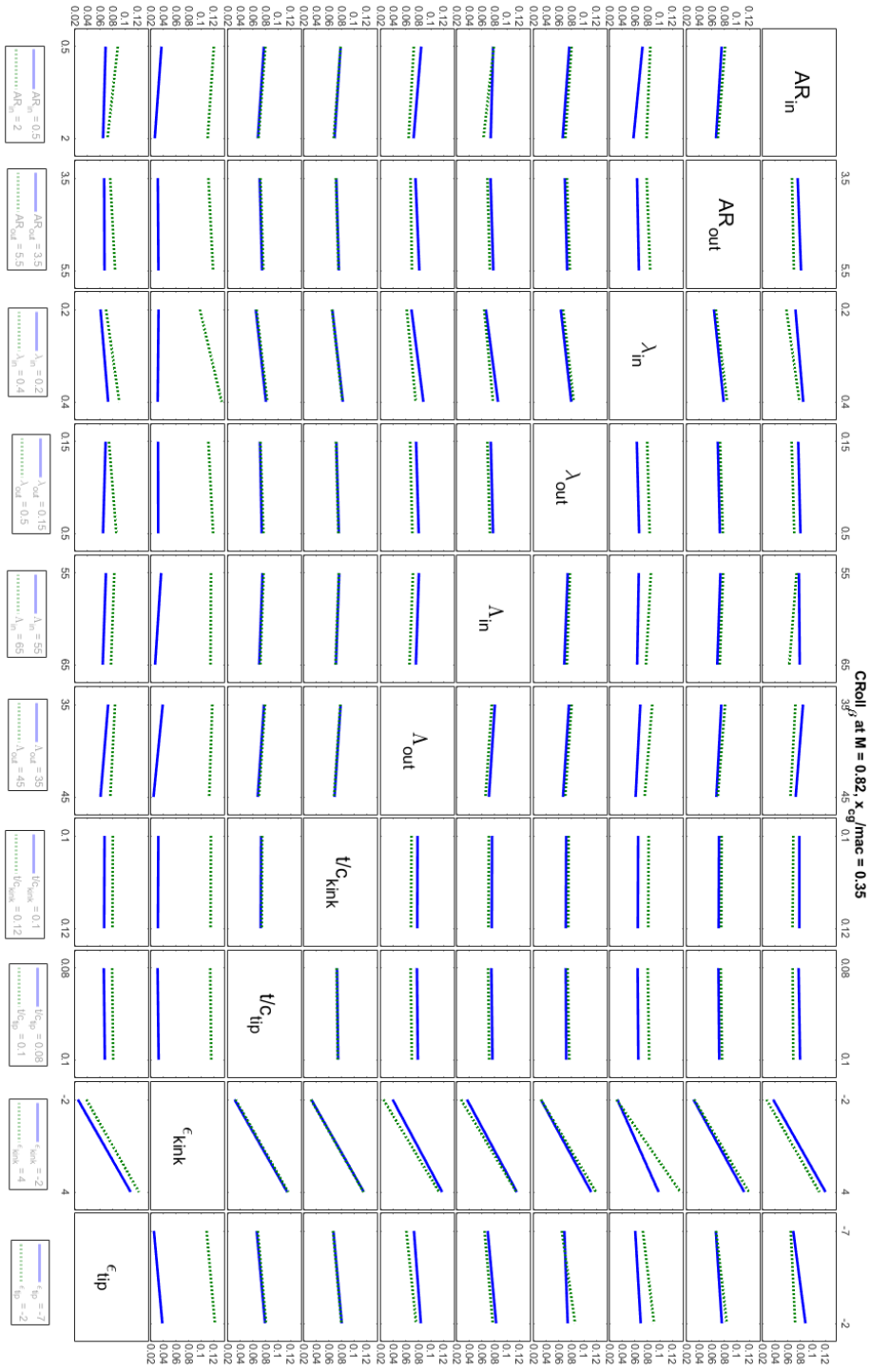

Figure 3.31: DoE interaction plot of the Roll Moment Coefficient gradient respect angle of sideslip ($C_{\mathcal{L}_\beta}$) for the second Design of Experiments at $x_{cg}/\text{mac} = 0.35$ $M = 0.82$. MATLAB.

3.2.3 DoE interaction plots investigation on the Second Design of Experiments at subsonic regime

As pointed out in Section 3.2.2, the results presented in this section are also made with the second Design of Experiments choice (Table 2.2).

Unlike the case shown before, this calculation is meant to recreate a take-off and landing condition in subsonic regime. For this reason the altitude is set at sea level condition ($h = 0\,\mathrm{m}$) and the Mach number at $M = 0.15$. The range of angles of attack vary from $-4°$ to $10°$ while keeping the sideslip angle set to 0. As seen in Section 3.2.1, since the Mach number is below the value of 0.3, the aircraft stall path evaluation will be implemented while the wave drag evaluation is omitted, being this drag contribution irrelevant at this Mach number.

The chosen outputs are the same displayed in the previous case with the addition of the starting stall path section location along the span (η_{SP}). Also in this case the results are shown for each centre of gravity location. Since the geometry planform for each combination of the Design of Experiments remained unchanged compared to the previous case, the DoE interaction plot of the reference wing area S_{ref} shows the same results seen in Figure 3.12.

Results Interpretation

Similar to the high subsonic case discussed before, this case is not a trimmed condition so the x_{cg} location contribution can be noticed only on the stability derivative responses.

In Figure 3.33 - 3.40 - 3.47 is presented the DoE interaction plots of the aerodynamic efficiency E. The first difference compared to the high subsonic case is in an higher efficiency value. Furthermore if in the previous case the $\mathit{Æ}_{\mathrm{in}}$-λ_{in} and λ_{in}-Λ_{inner} interactions were the most predominant, now in the subsonic regime these interactions lose relevance in favor of a λ_{in}-$\varepsilon_{\mathrm{kink}}$ predominant interaction. To a second degree of relevance we find the interactions between $\mathit{Æ}_{\mathrm{in}}$-$\mathit{Æ}_{\mathrm{out}}$, $\mathit{Æ}_{\mathrm{out}}$-$\lambda_{\mathrm{in}}$, and Λ_{inner}-$\varepsilon_{\mathrm{kink}}$.

In Figure 3.34 - 3.41 - 3.48 is presented the DoE interaction plots of $C_{\mathcal{M}_0}$. This response shows the same interactions behaviour of the high subsonic case. The most important interaction is between $\mathit{Æ}_{\mathrm{in}}$-$\varepsilon_{\mathrm{kink}}$.

In Figure 3.35 - 3.42 - 3.49 is presented the DoE interaction plots of C_{L_α}. Compared to the high subsonic case, the value of C_{L_α} tend to be lower. The most important interaction behaviour remains equal to the previous case with $\mathcal{R}_{\text{in}}$-$\mathcal{R}_{\text{out}}$, $\mathcal{R}_{\text{in}}$-λ_{in}, $\mathcal{R}_{\text{in}}$-Λ_{inner}, and $\mathcal{R}_{\text{in}}$-Λ_{outer}.

In Figure 3.36 - 3.43 - 3.50 the DoE interaction plots of $C_{\mathcal{M}_\alpha}$ are presented. Also for this response the value of $C_{\mathcal{M}_\alpha}$ tend to be lower compared to the high subsonic case. Interaction behaviours remain unchanged, most influential ones are between $\mathcal{R}_{\text{in}}$-λ_{in}, $\mathcal{R}_{\text{in}}$-$\mathcal{R}_{\text{out}}$, $\mathcal{R}_{\text{in}}$-λ_{out}, $\mathcal{R}_{\text{out}}$-λ_{in}, and λ_{in}-λ_{out}. The x_{cg} location influence is shown in Figure 3.32.

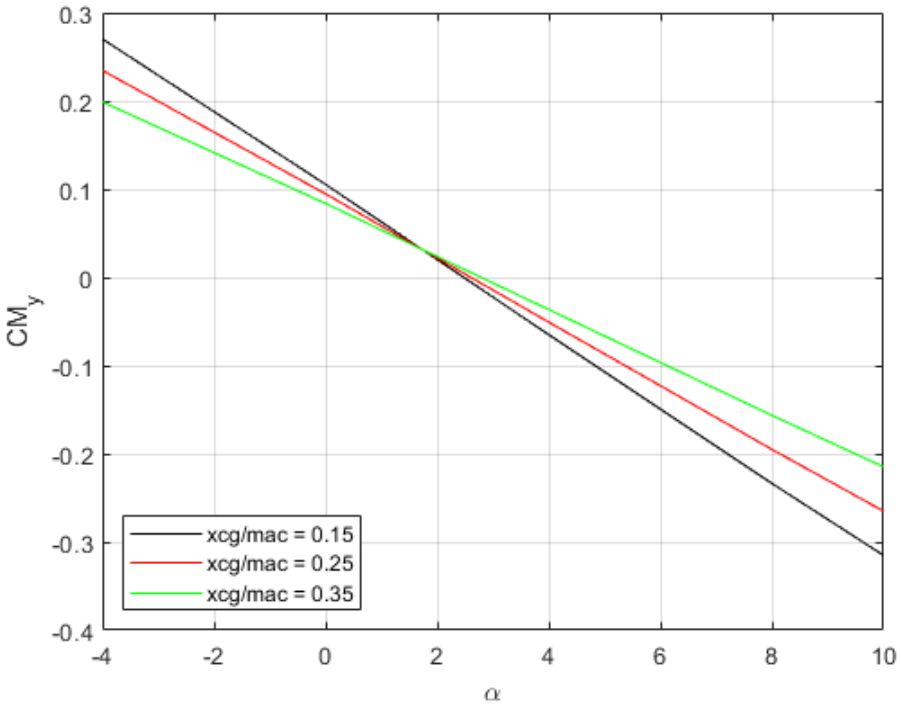

Figure 3.32: Pitching moment coefficient $C_{\mathcal{M}_y}$ of a BWB planform at $x_{\text{cg}}/\text{mac} = 0.15$ - 0.25 - 0.35 $M = 0.15$. MATLAB.

In Figure 3.37 - 3.44 - 3.51 and in Figure 3.38 - 3.45 - 3.52 the DoE interaction plots of $C_{\mathcal{N}_\beta}$ and $C_{\mathcal{L}_\beta}$ are presented. For both the responses the results aforementioned doesn't change compared to the high subsonic case.

Lastly in Figure 3.39 - 3.46 - 3.53 the DoE interaction plots of η_{SP} are presented. No evidence of the x_{cg} location was found. Most relevant interactions are between $\mathcal{R}_{\text{in}}$-λ_{in}, $\mathcal{R}_{\text{in}}$-λ_{out}, $\mathcal{R}_{\text{in}}$-ε_{tip}, $\mathcal{R}_{\text{out}}$-ε_{tip}, λ_{out}-ε_{tip} and $\varepsilon_{\text{kink}}$-$\varepsilon_{\text{tip}}$. In order to achieve a stall starting point closer to the *centre-body* region, the aircraft geometry demands a large

value of λ_{out}, in order to have larger chords and larger Reynolds number, and large negative values of ε_{tip} in order to shift the aerodynamic load towards the root chord. In particular, minimum value of Æ_{in} together with maximum value Æ_{out} involve in less η_{SP} value. It is important to clarify that this calculation was performed at low Mach number in order to simulate a take-off/landing condition where the *outer-wing* ailerons will guarantee an appropriate controllability of the aircraft. To a second degree come the interactions between λ_{in}-λ_{out}, Æ_{in}-Λ_{inner}, and λ_{out}-Λ_{inner}.

Centre of gravity at 15% of mac

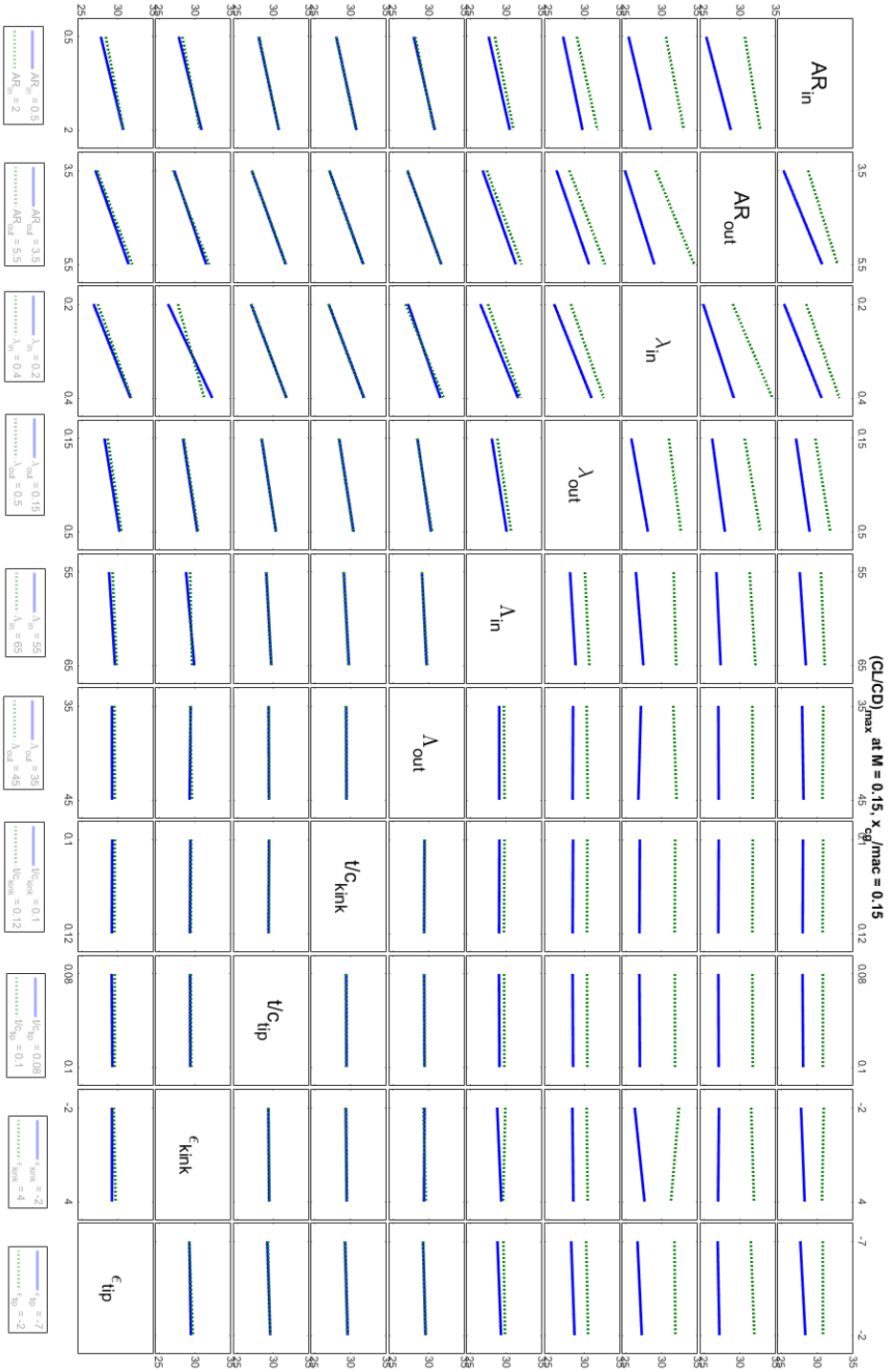

Figure 3.33: DoE interaction plot of the Aerodynamic Efficiency (E) for the second Design of Experiments at $x_{\text{cg}}/\text{mac} = 0.15$ $M = 0.15$. MATLAB.

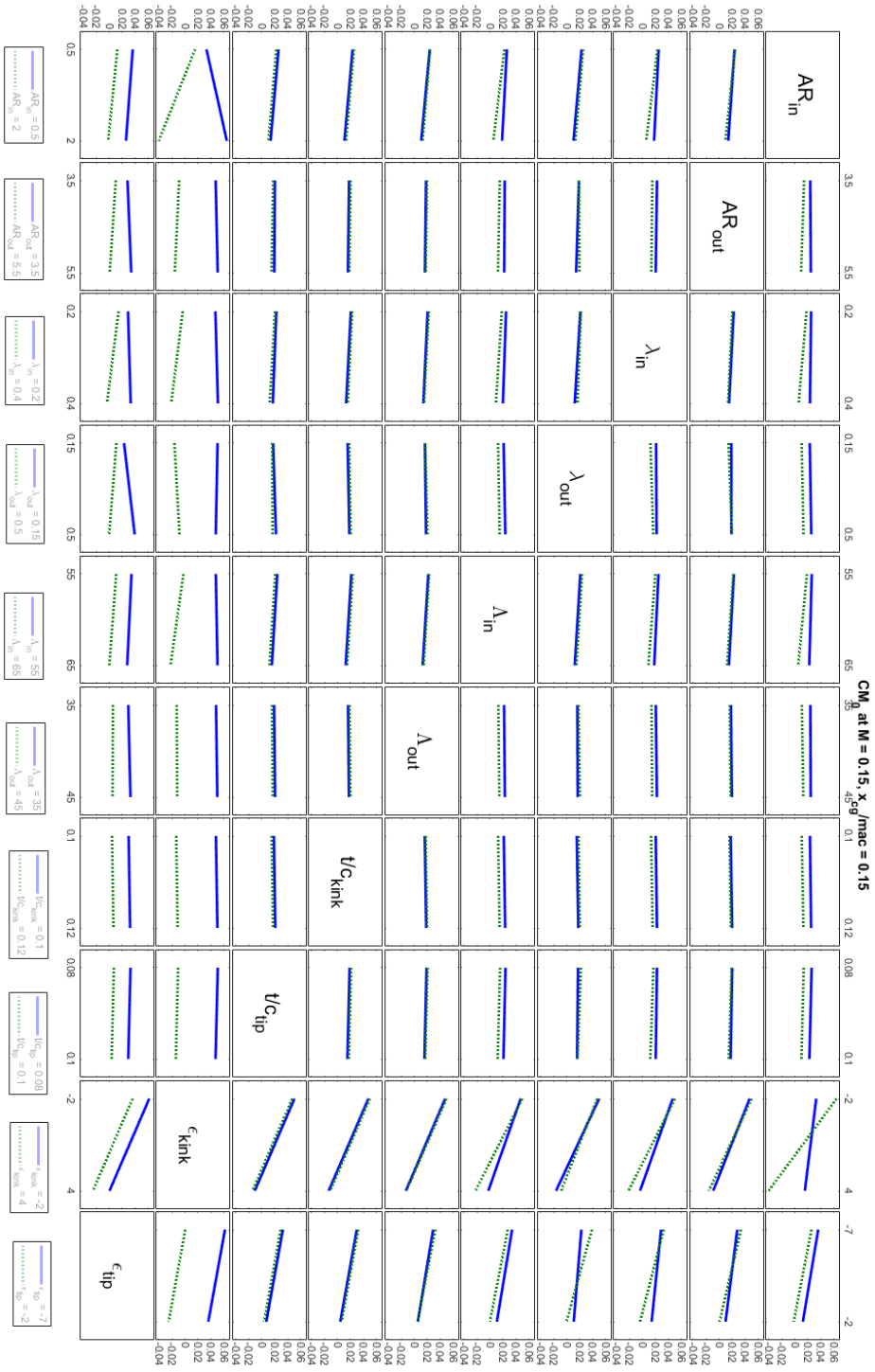

Figure 3.34: DoE interaction plot of the Pitching Moment Coefficient at zero lift angle of attack ($C_{\mathcal{M}_0}$) for the second Design of Experiments at $x_{\text{cg}}/\text{mac} = 0.15$ $M = 0.15$. MATLAB.

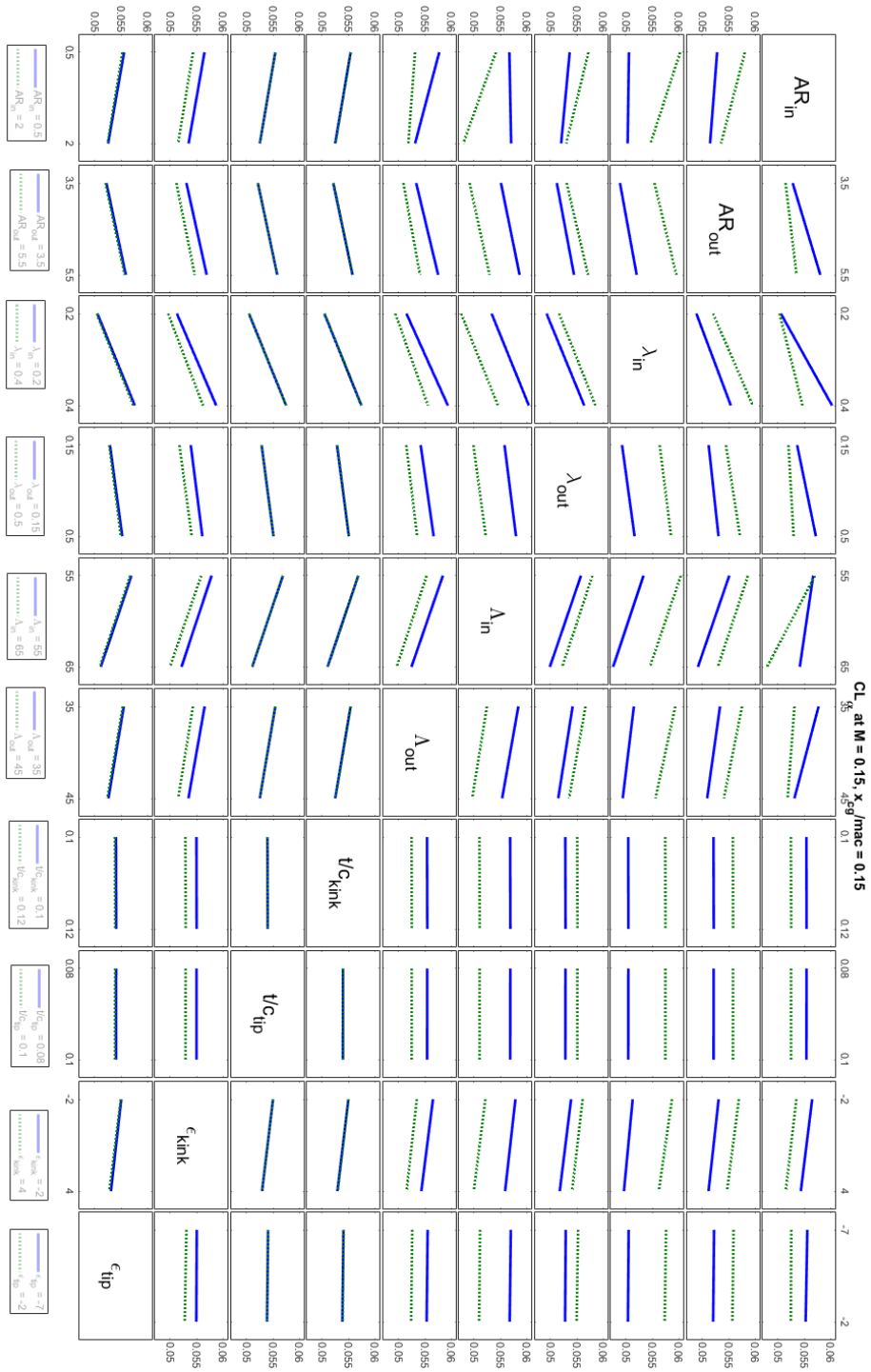

Figure 3.35: DoE interaction plot of the Wing Lift Slope coefficient (C_{L_α}) for the second Design of Experiments at $x_{\text{cg}}/\text{mac} = 0.15$ $M = 0.15$. MATLAB.

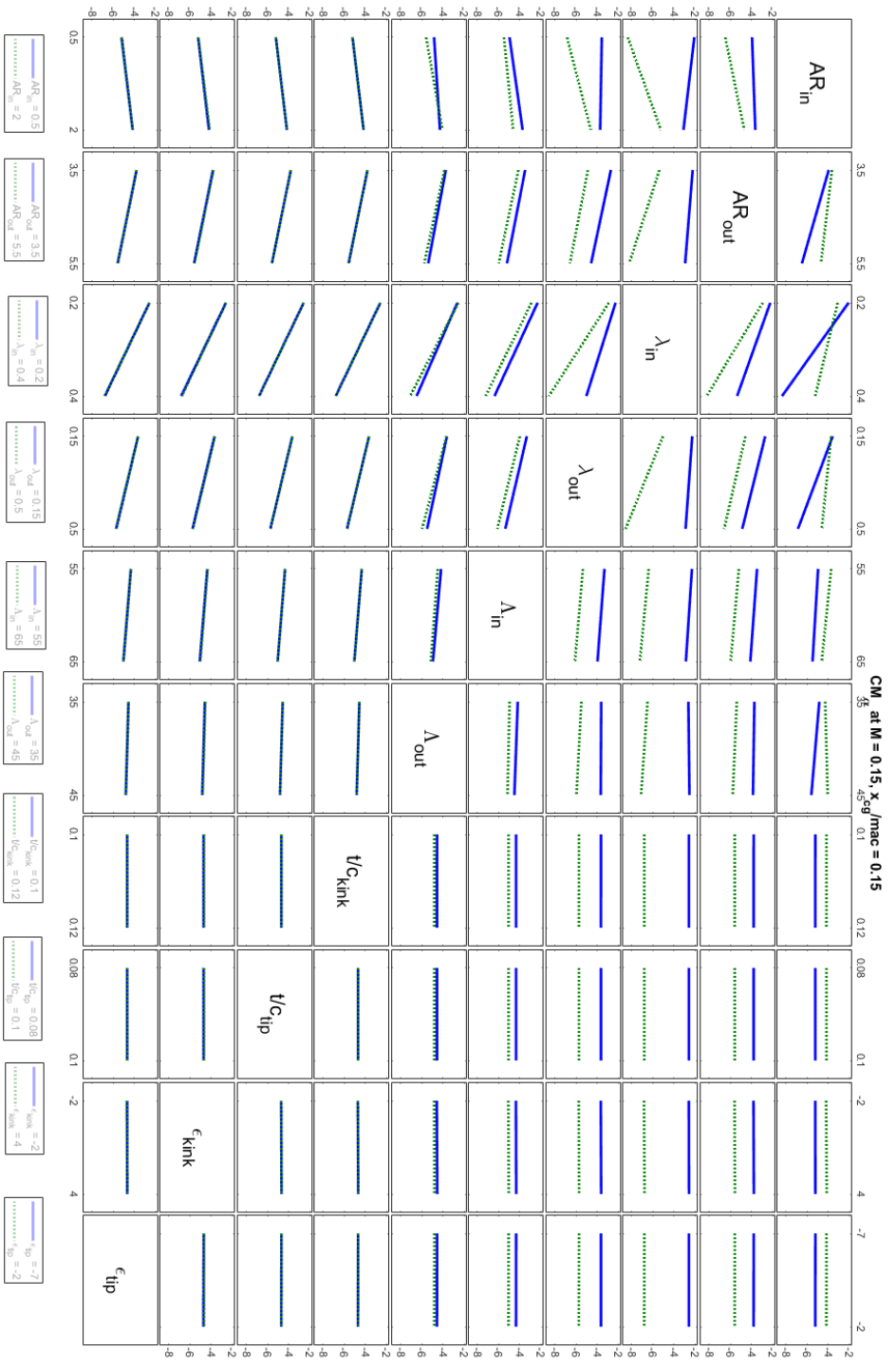

Figure 3.36: DoE interaction plot of the Pitching Moment Coefficient gradient respect angle of attack ($C_{\mathcal{M}_\alpha}$) for the second Design of Experiments at $x_{\text{cg}}/\text{mac} = 0.15$ $M = 0.15$. MATLAB.

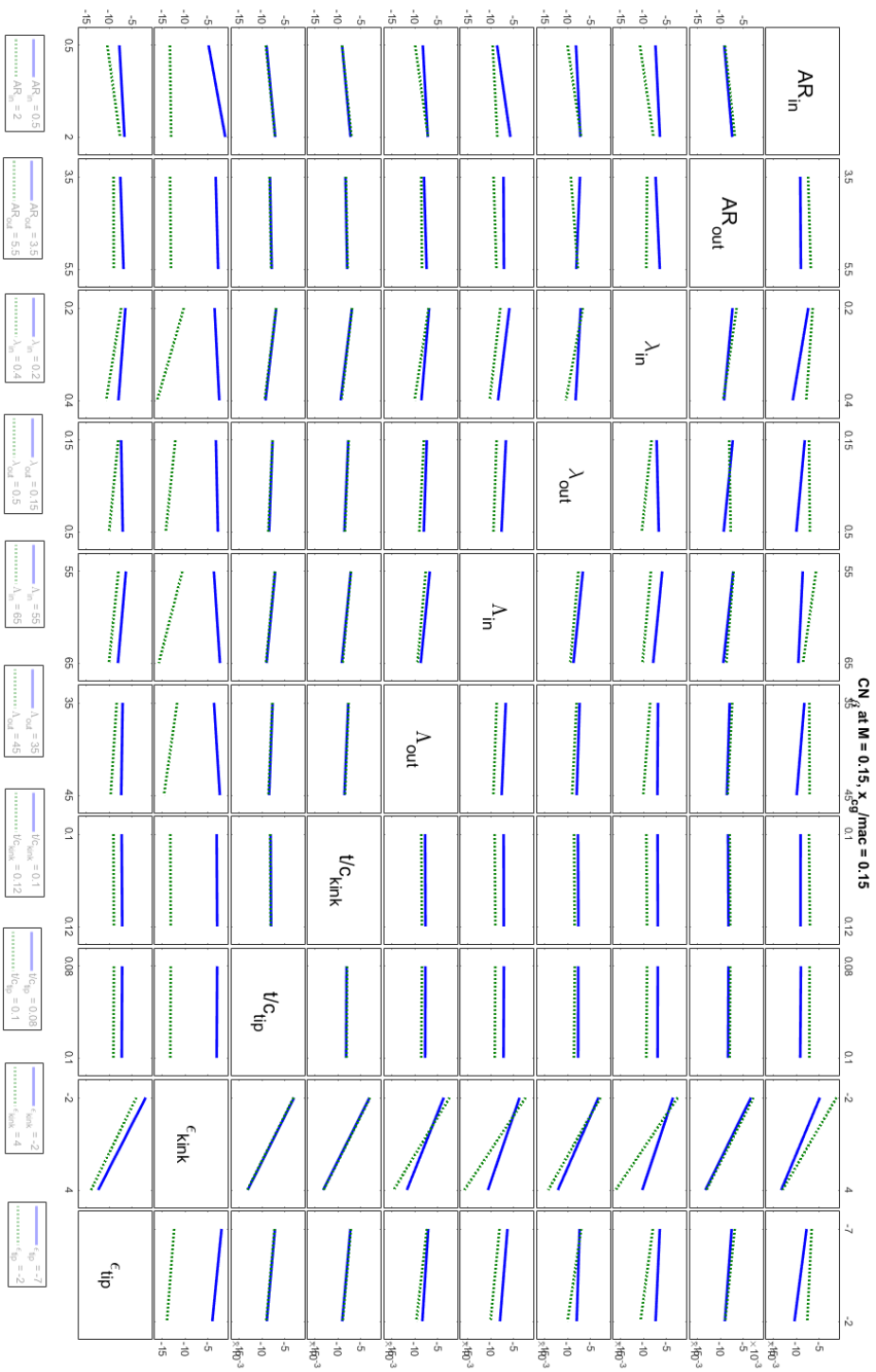

Figure 3.37: DoE interaction plot of the Yaw Moment Coefficient gradient respect angle of sideslip ($C_{\mathcal{N}_\beta}$) for the second Design of Experiments at $x_{\text{cg}}/\text{mac} = 0.15$ $M = 0.15$. MATLAB.

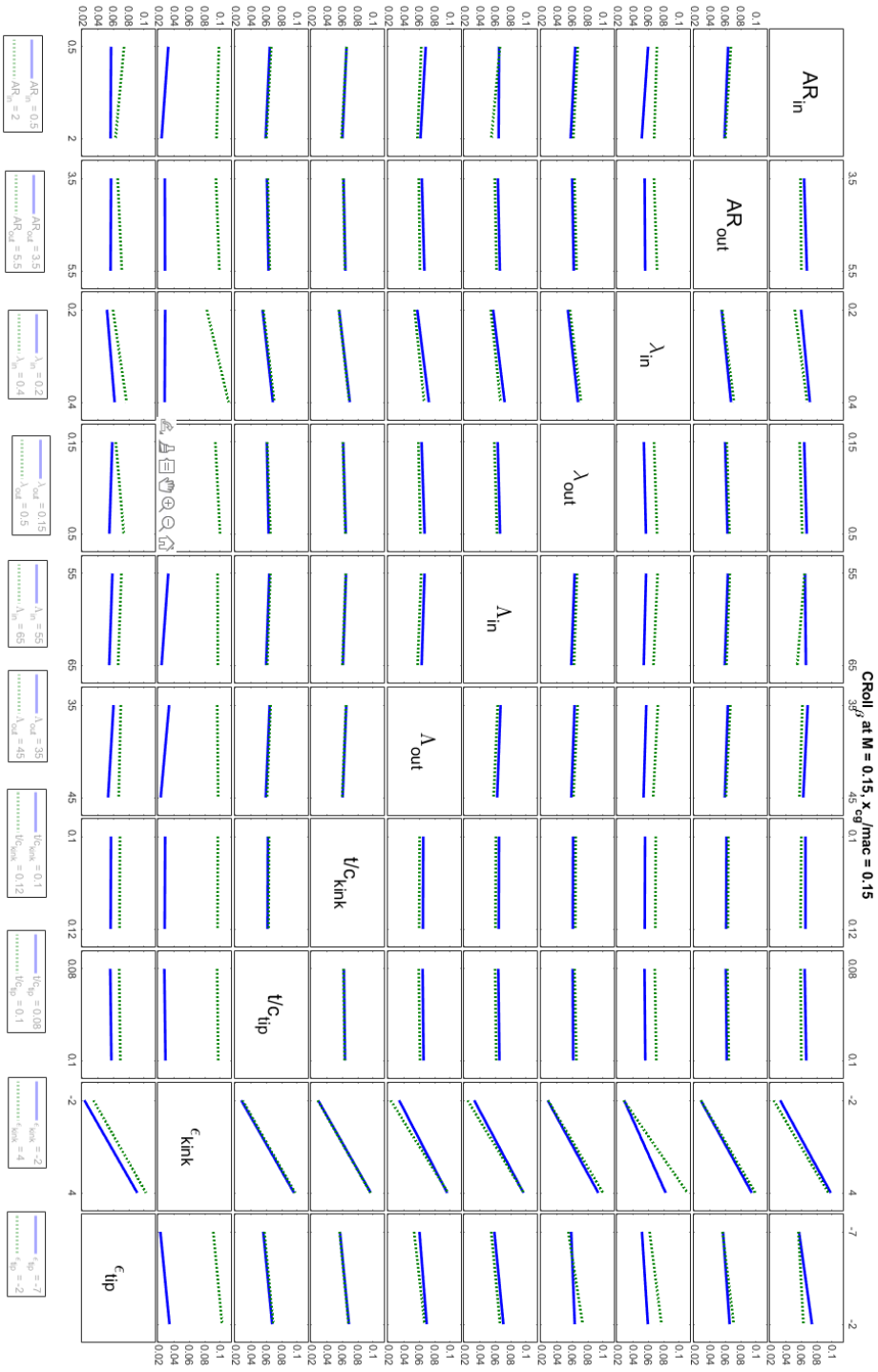

Figure 3.38: DoE interaction plot of the Roll Moment Coefficient gradient respect angle of sideslip ($C_{\mathcal{L}_\beta}$) for the second Design of Experiments at $x_{cg}/\text{mac} = 0.15$ $M = 0.15$. MATLAB.

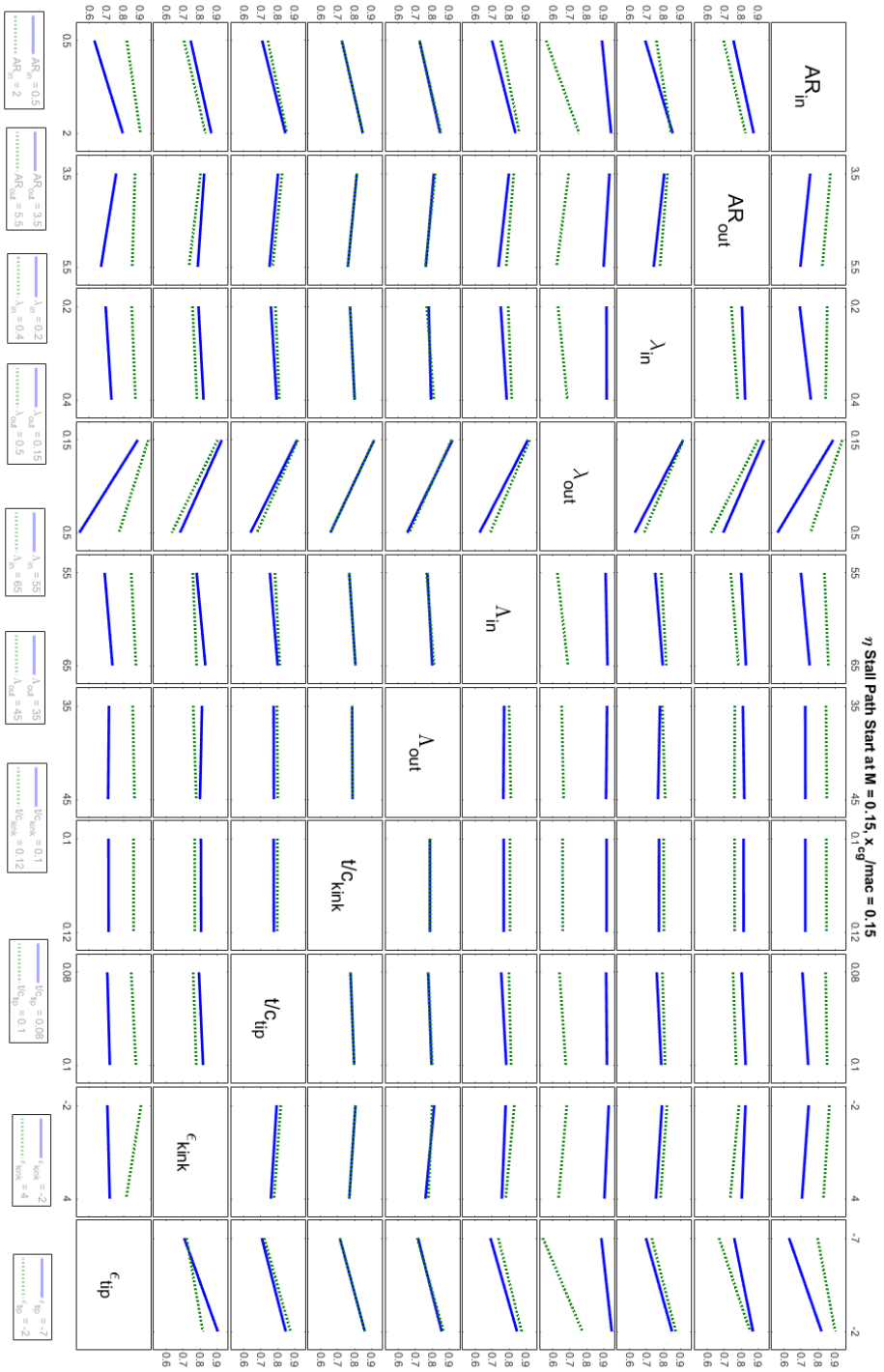

Figure 3.39: DoE interaction plot of the Stall Path section location along the span (η_{SP}) for the second Design of Experiments at $x_{\text{cg}}/\text{mac} = 0.15$ $M = 0.15$. MATLAB.

Centre of gravity at 25% of mac

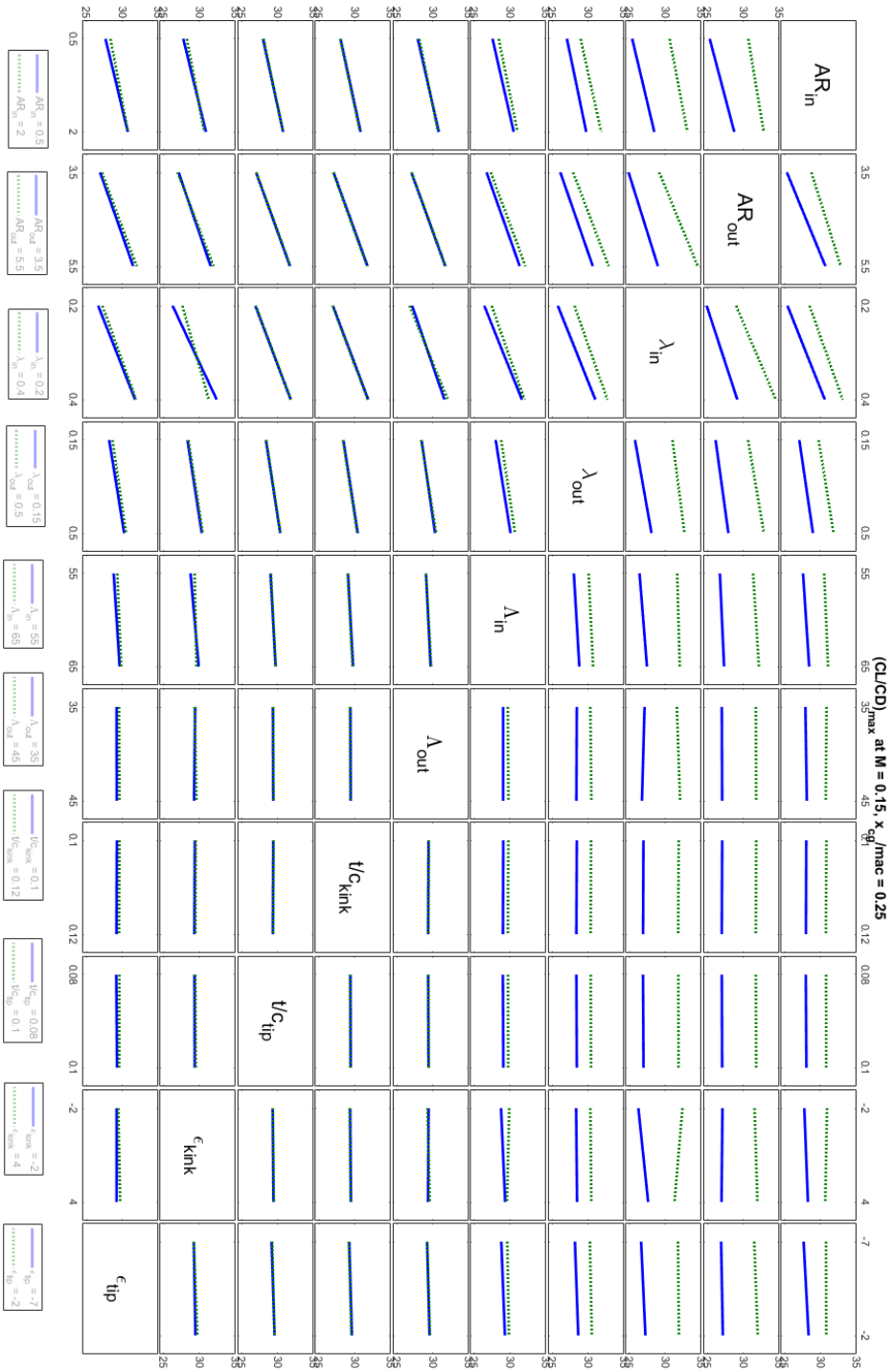

Figure 3.40: DoE interaction plot of the Aerodynamic Efficiency (E) for the second Design of Experiments at $x_{\text{cg}}/\text{mac} = 0.25$ $M = 0.15$. MATLAB.

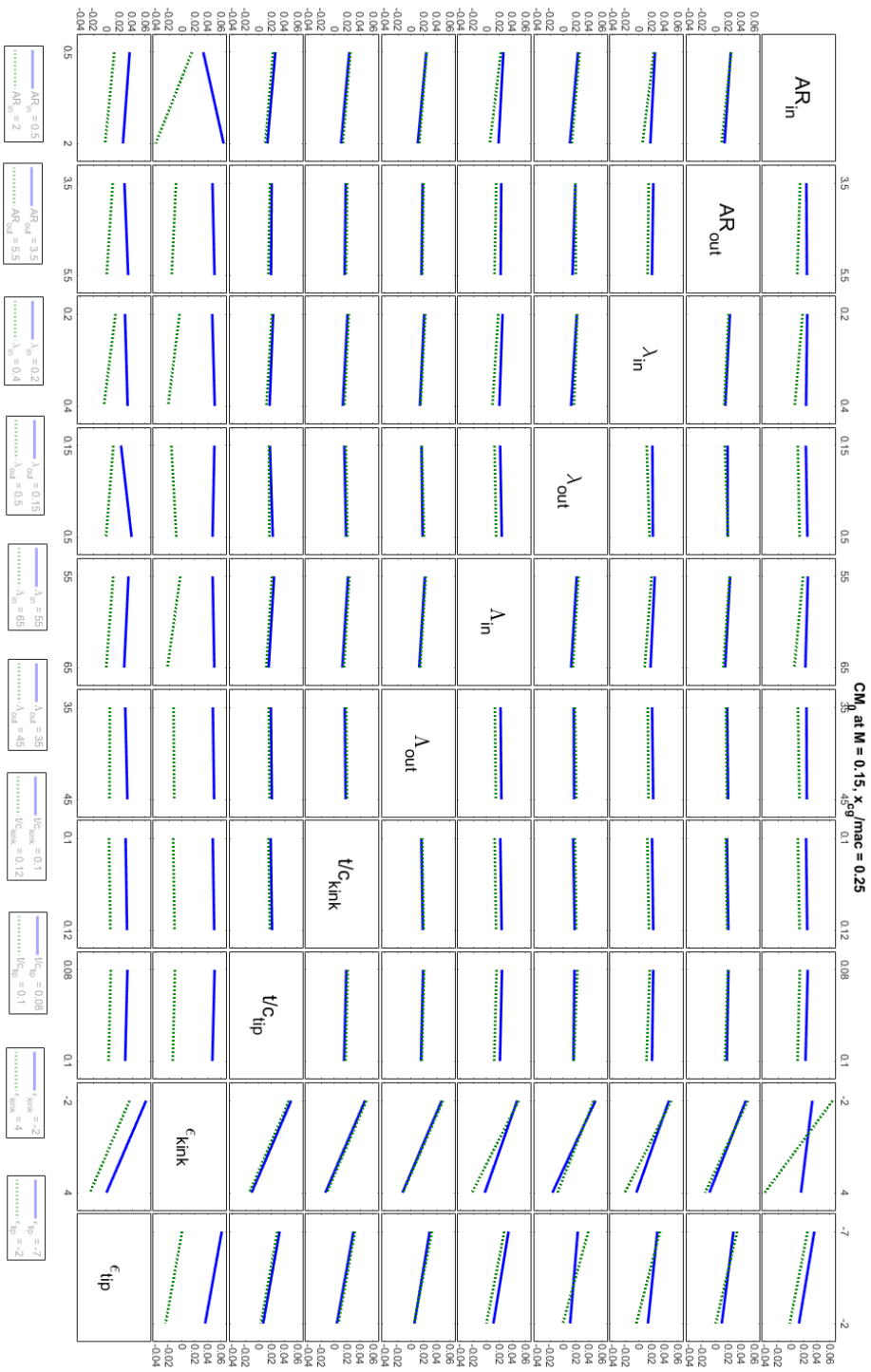

Figure 3.41: DoE interaction plot of the Pitching Moment Coefficient at zero lift angle of attack ($C_{\mathcal{M}_0}$) for the second Design of Experiments at $x_{\text{cg}}/\text{mac} = 0.25$ $M = 0.15$. MATLAB.

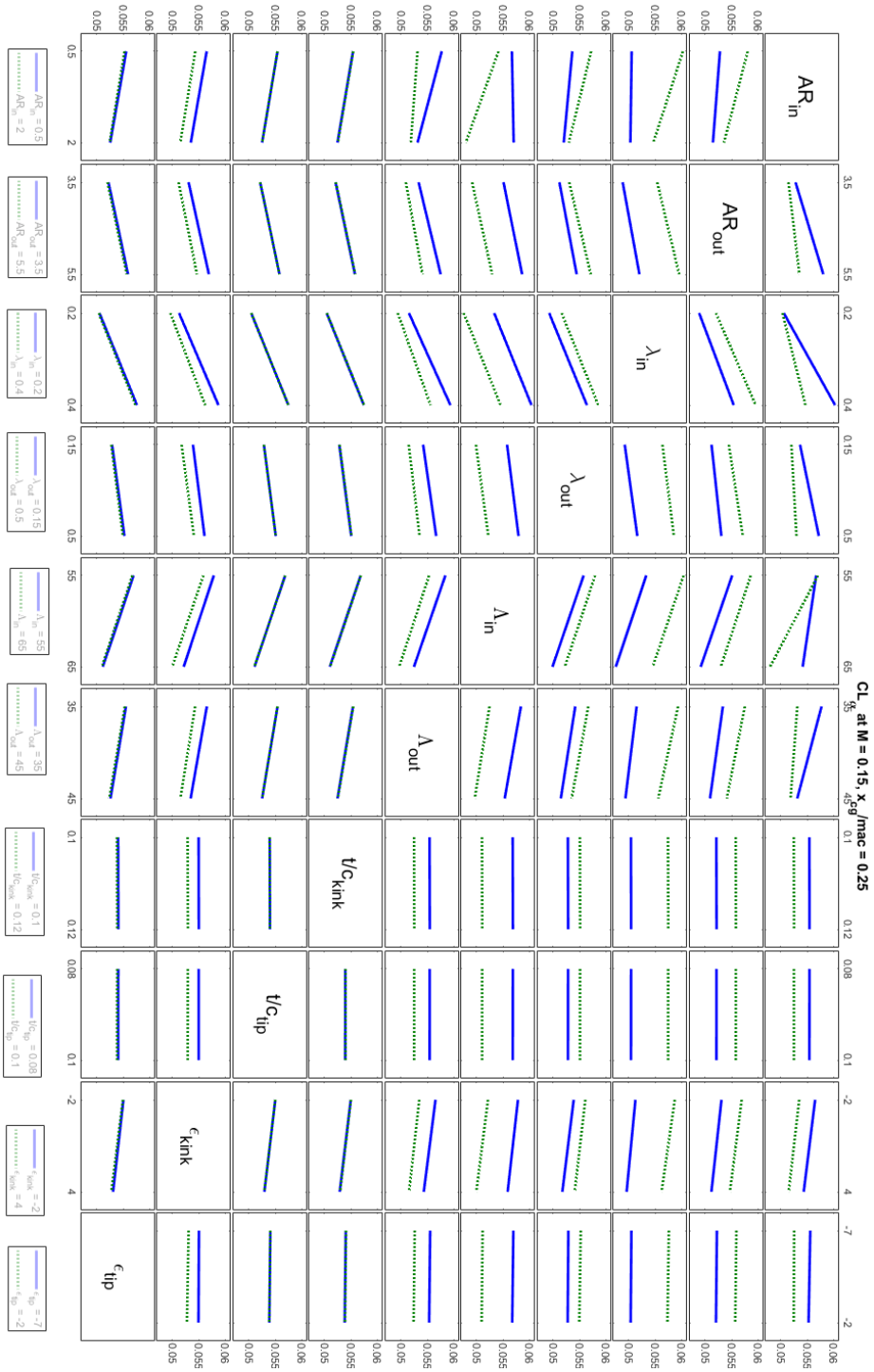

Figure 3.42: DoE interaction plot of the Wing Lift Slope coefficient (C_{L_α}) for the second Design of Experiments at $x_{\text{cg}}/\text{mac} = 0.25$ $M = 0.15$. MATLAB.

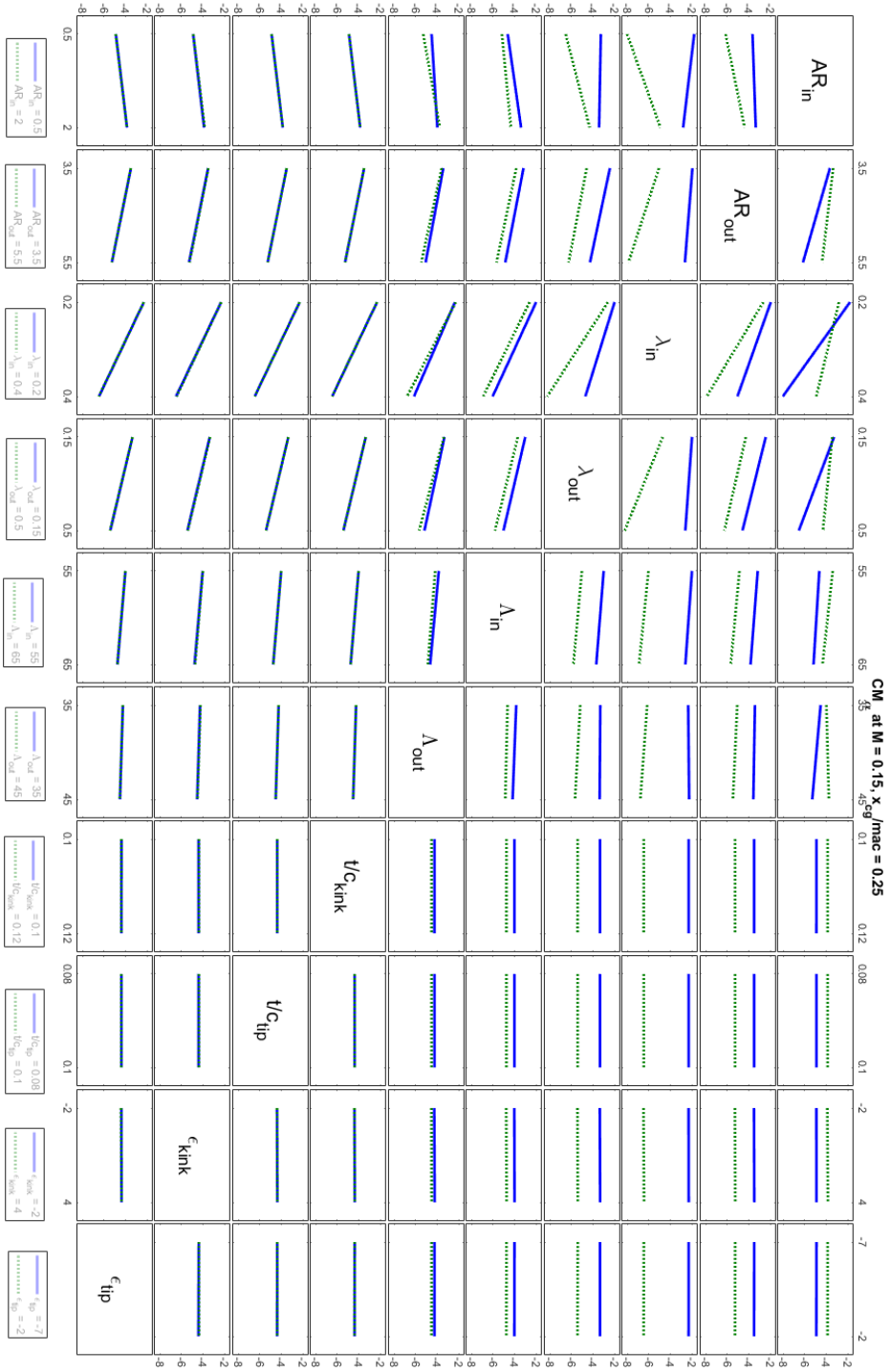

Figure 3.43: DoE interaction plot of the Pitching Moment Coefficient gradient respect angle of attack ($C_{\mathcal{M}_\alpha}$) for the second Design of Experiments at $x_{\text{cg}}/\text{mac} = 0.25$ $M = 0.15$. MATLAB.

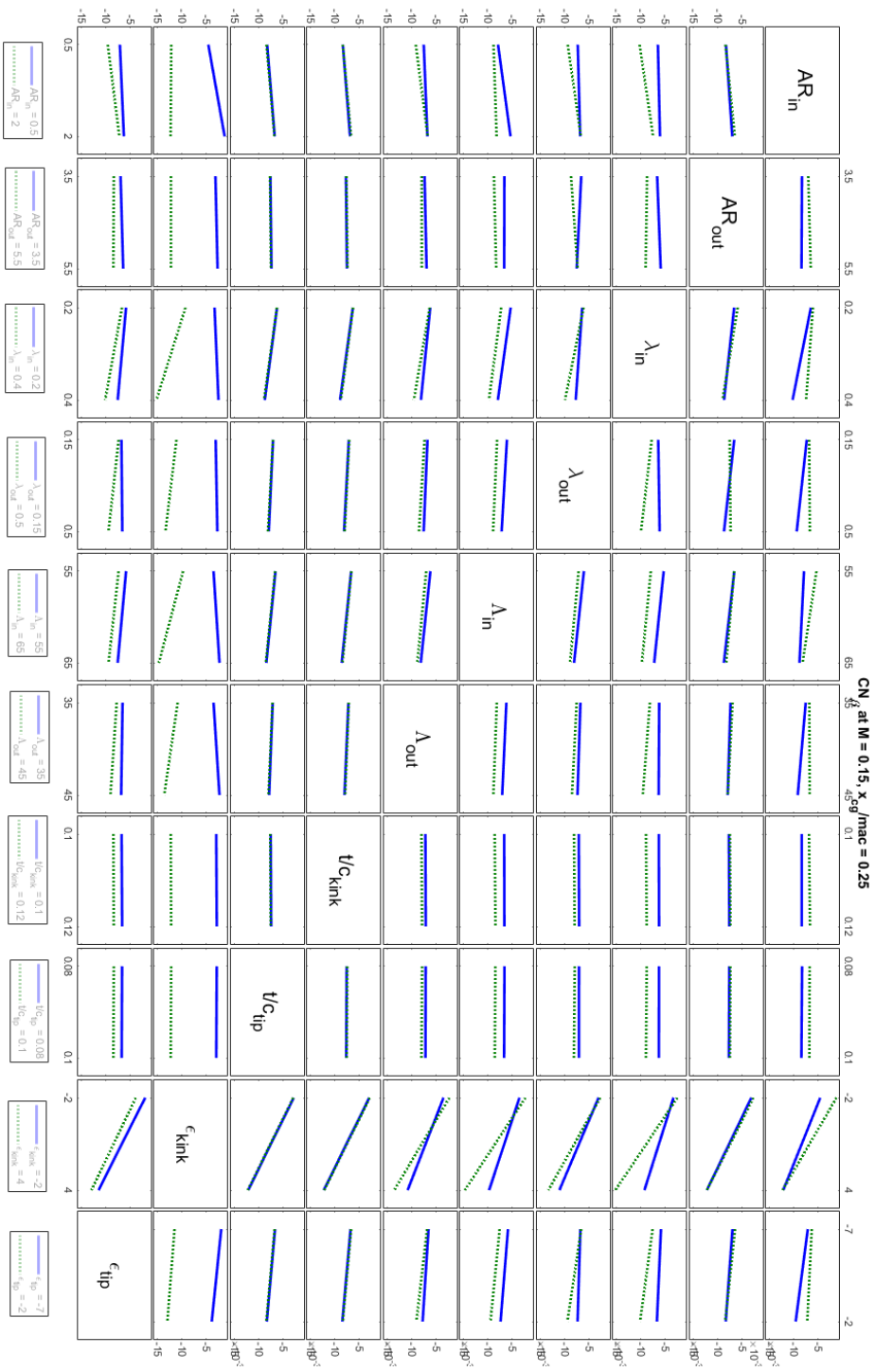

Figure 3.44: DoE interaction plot of the Yaw Moment Coefficient gradient respect angle of sideslip ($C_{\mathcal{N}_\beta}$) for the second Design of Experiments at $x_{\text{cg}}/\text{mac} = 0.25$ $M = 0.15$. MATLAB.

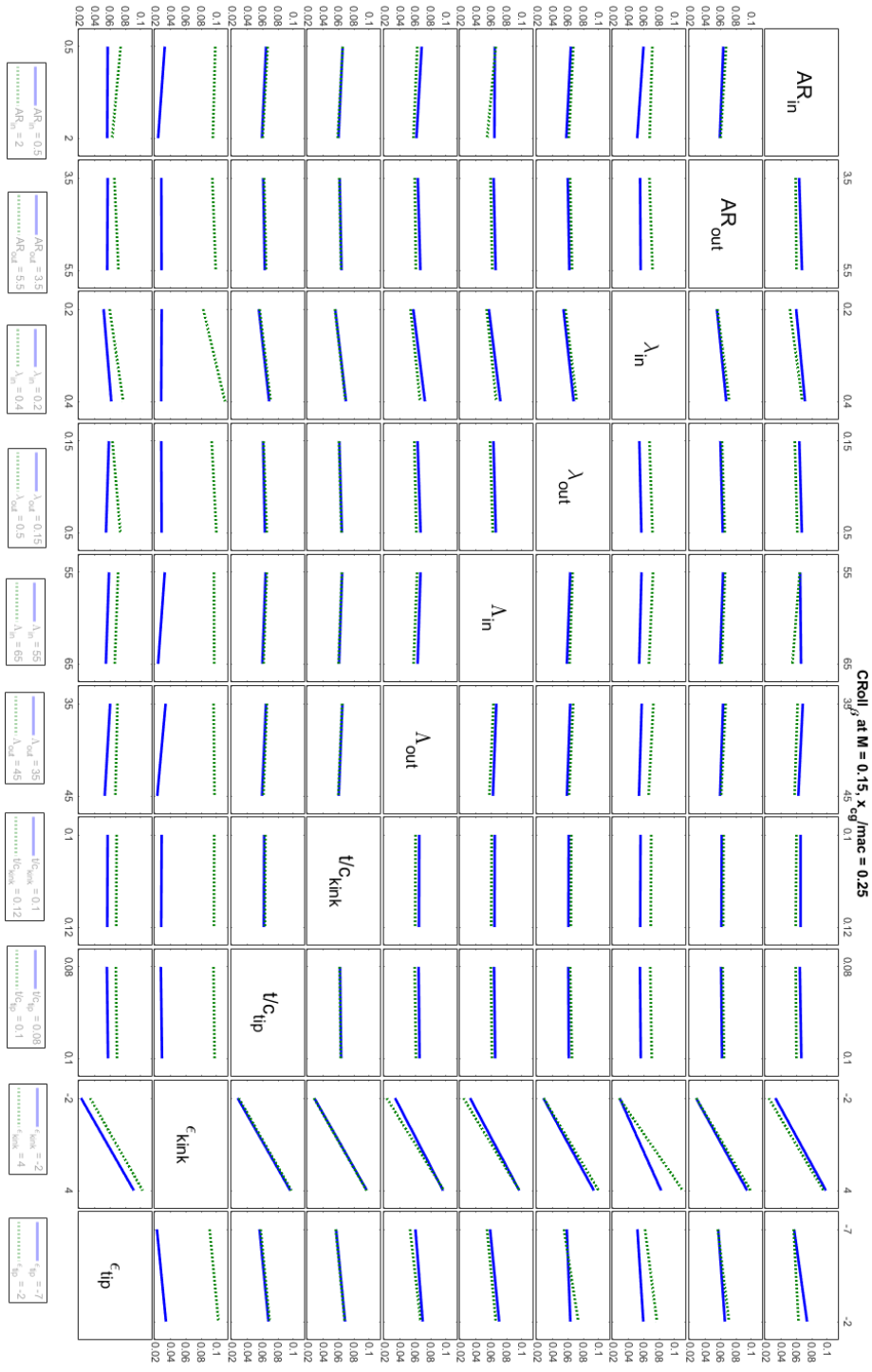

Figure 3.45: DoE interaction plot of the Roll Moment Coefficient gradient respect angle of sideslip ($C_{\mathcal{L}_\beta}$) for the second Design of Experiments at $x_{\text{cg}}/\text{mac} = 0.25$ $M = 0.15$. MATLAB.

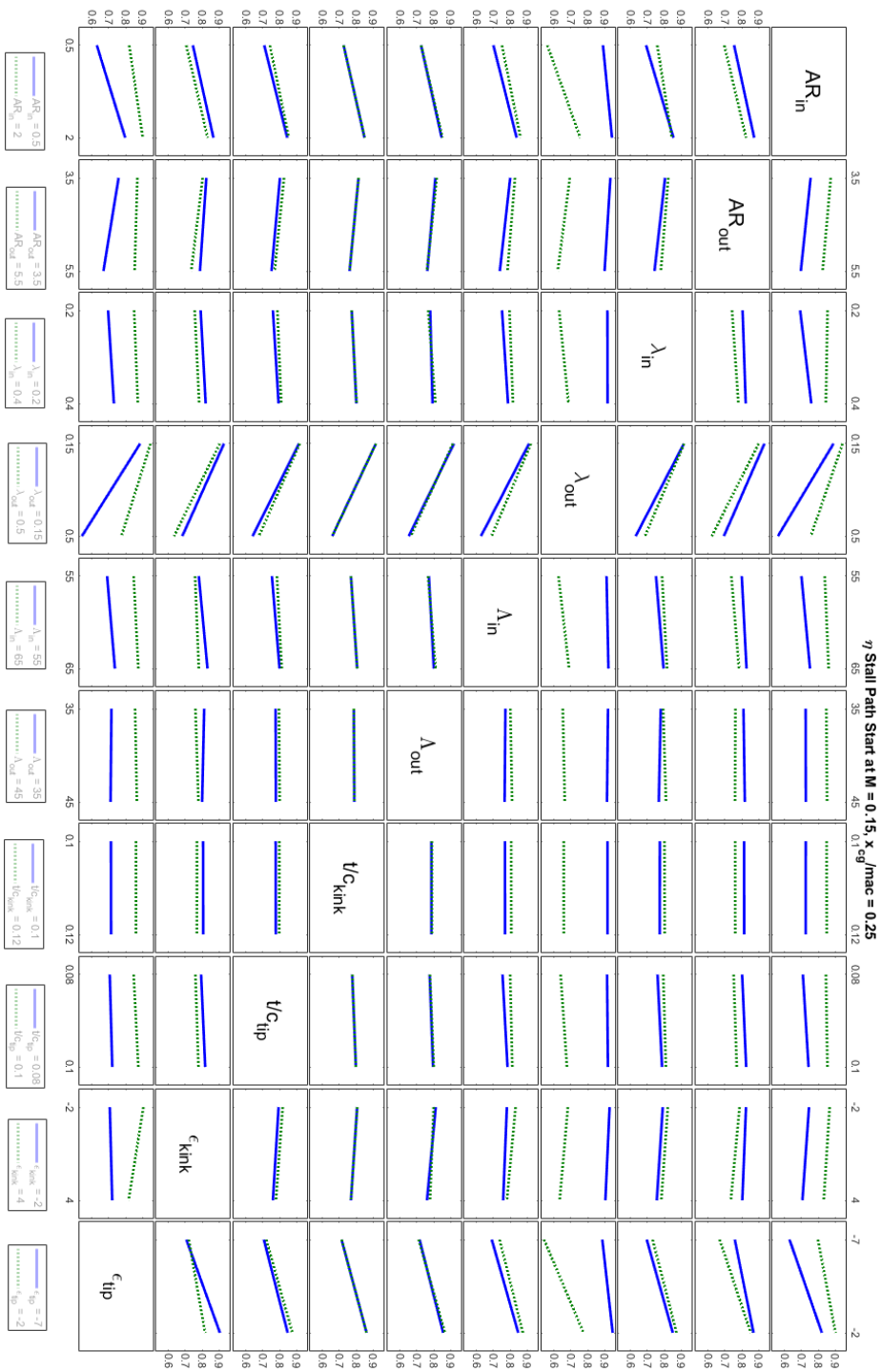

Figure 3.46: DoE interaction plot of the Stall Path section location along the span (η_{SP}) for the second Design of Experiments at $x_{\mathrm{cg}}/\mathrm{mac} = 0.25$ $M = 0.15$. MATLAB.

Centre of gravity at 35% of mac

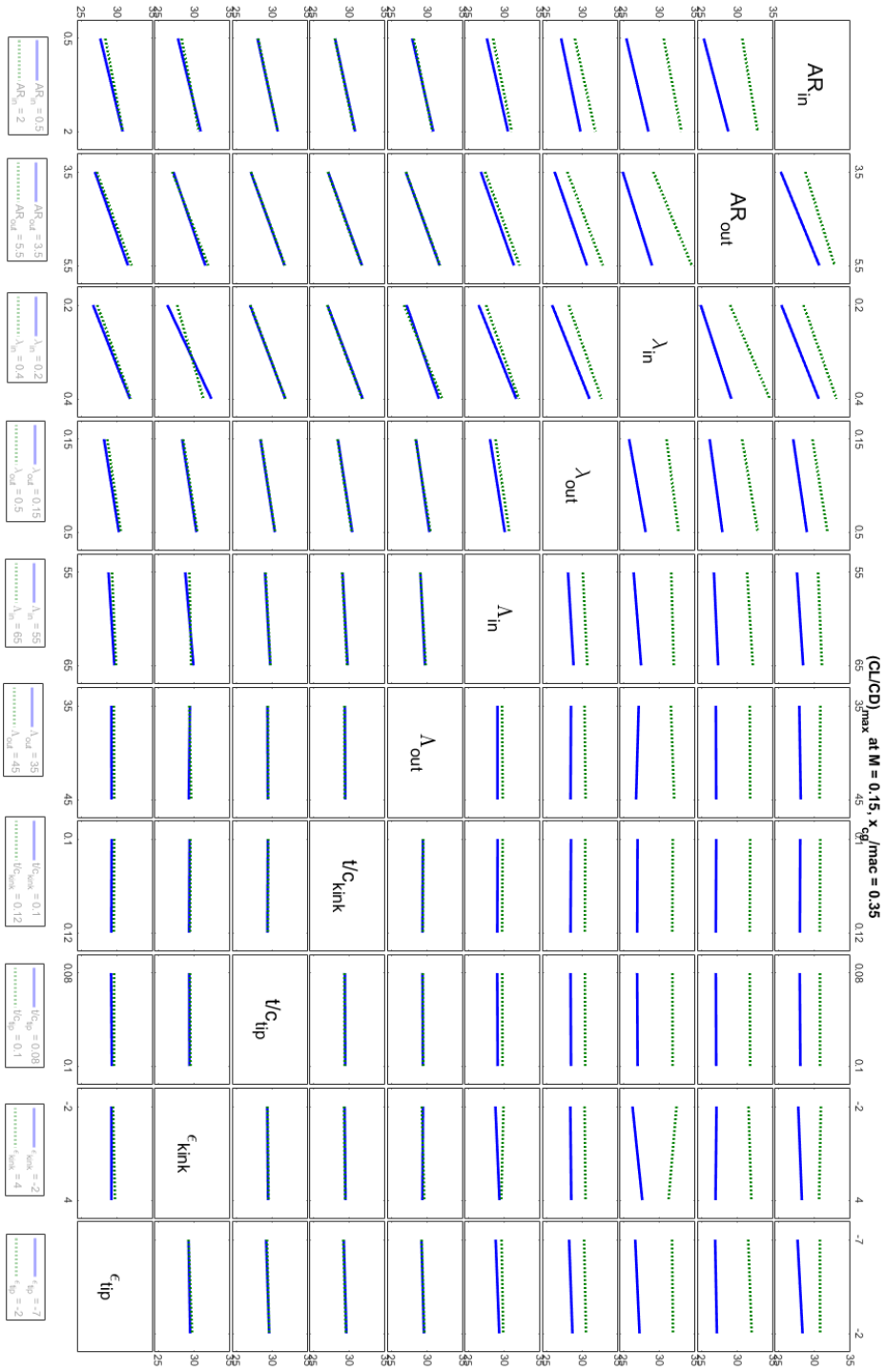

Figure 3.47: DoE interaction plot of the Aerodynamic Efficiency (E) for the second Design of Experiments at $x_{\text{cg}}/\text{mac} = 0.35$ $M = 0.15$. MATLAB.

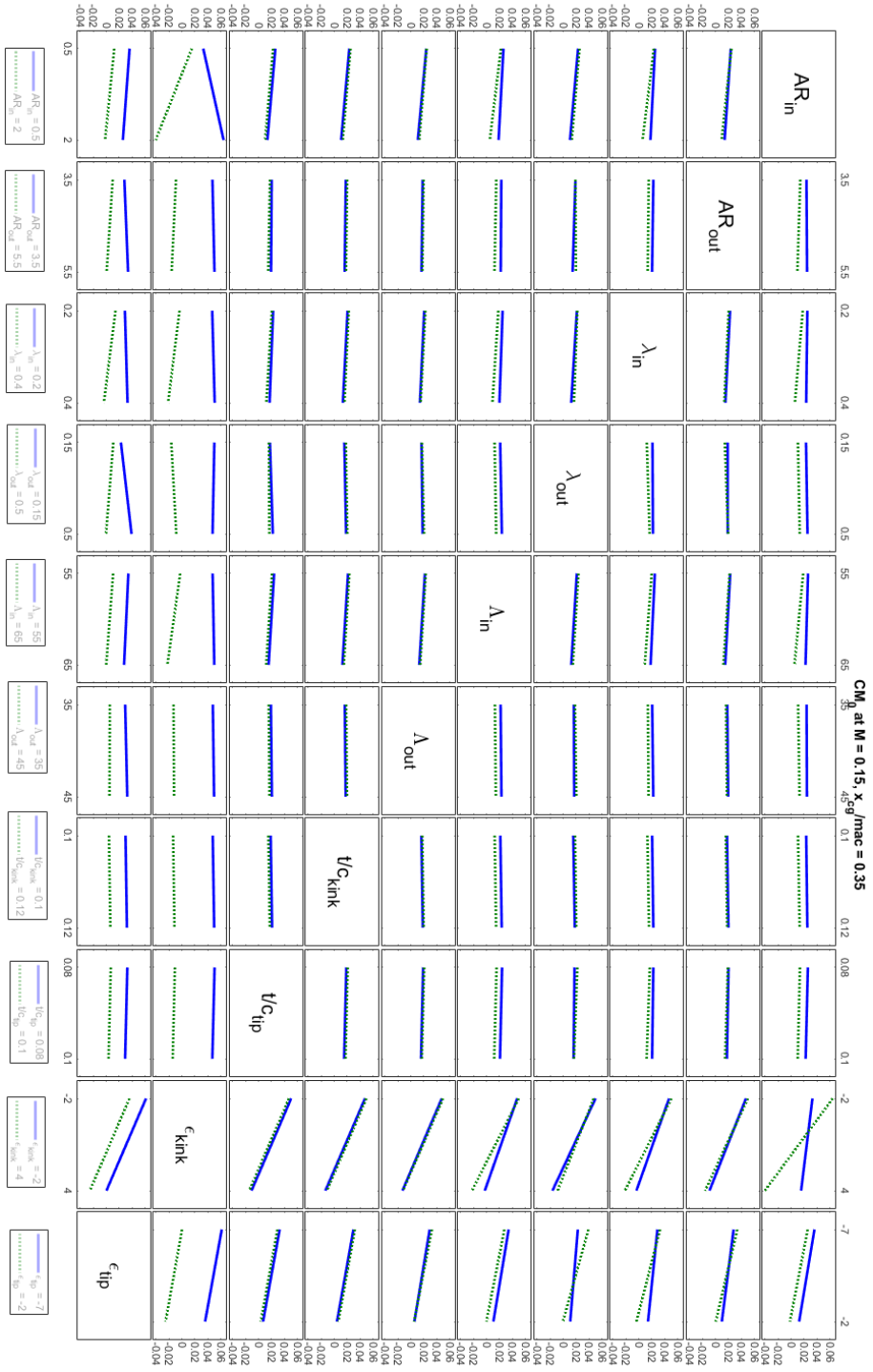

Figure 3.48: DoE interaction plot of the Pitching Moment Coefficient at zero lift angle of attack ($C_{\mathcal{M}_0}$) for the second Design of Experiments at $x_{\text{cg}}/\text{mac} = 0.35$ $M = 0.15$. MATLAB.

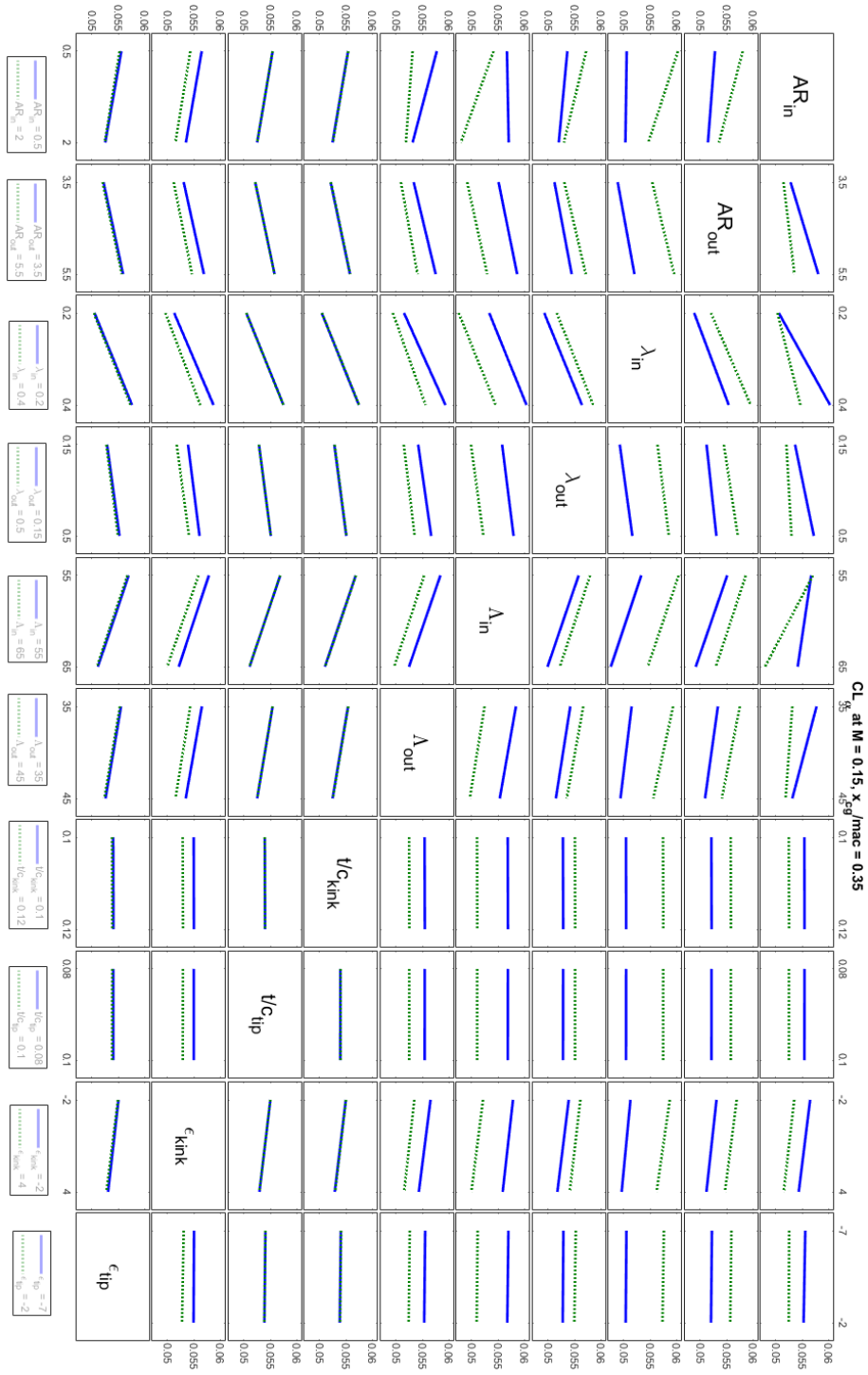

Figure 3.49: DoE interaction plot of the Wing Lift Slope coefficient (C_{L_α}) for the second Design of Experiments at $x_{\text{cg}}/\text{mac} = 0.35$ $M = 0.15$. MATLAB.

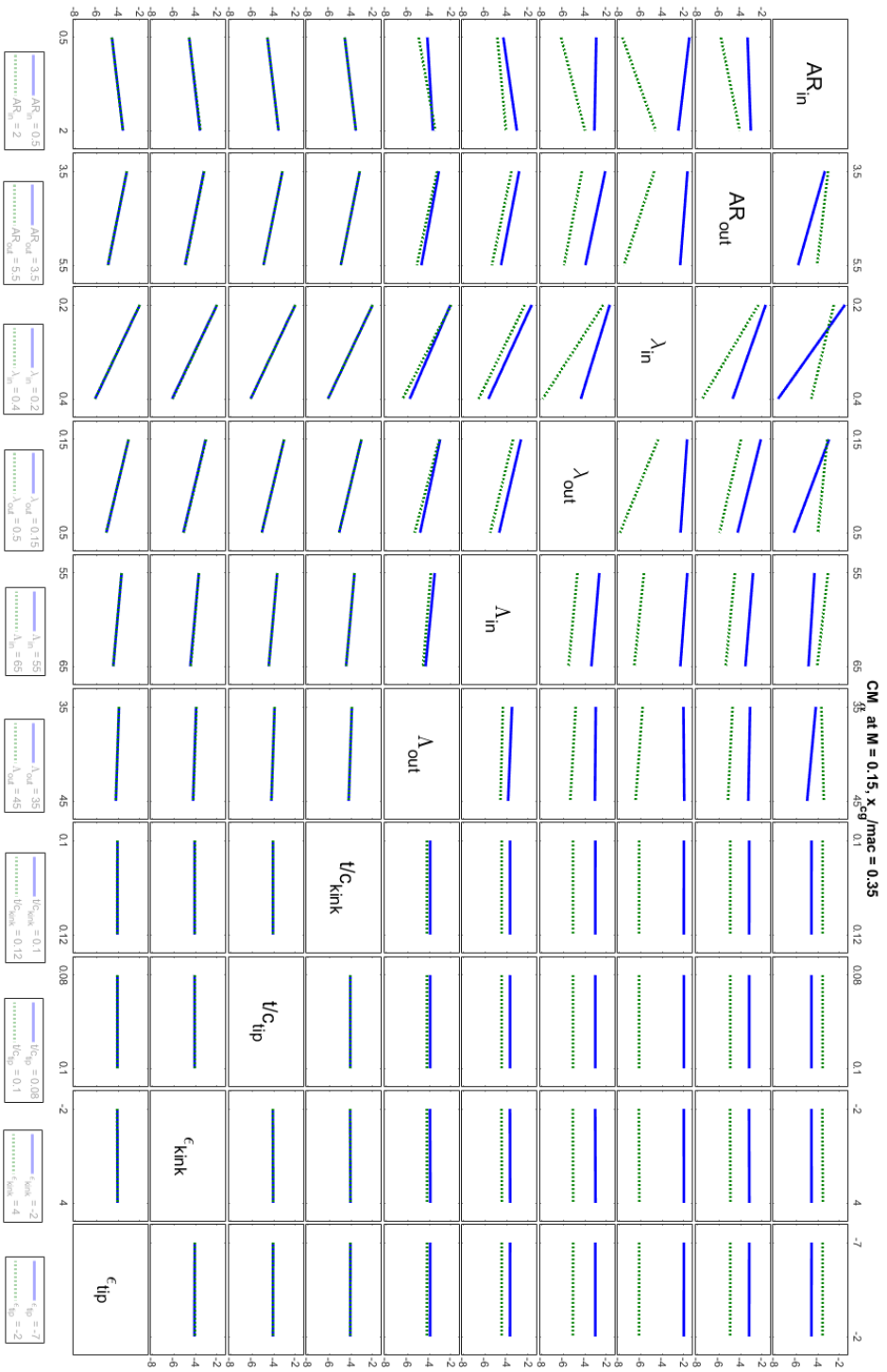

Figure 3.50: DoE interaction plot of the Pitching Moment Coefficient gradient respect angle of attack ($C_{\mathcal{M}_\alpha}$) for the second Design of Experiments at $x_{\text{cg}}/\text{mac} = 0.35$ $M = 0.15$. MATLAB.

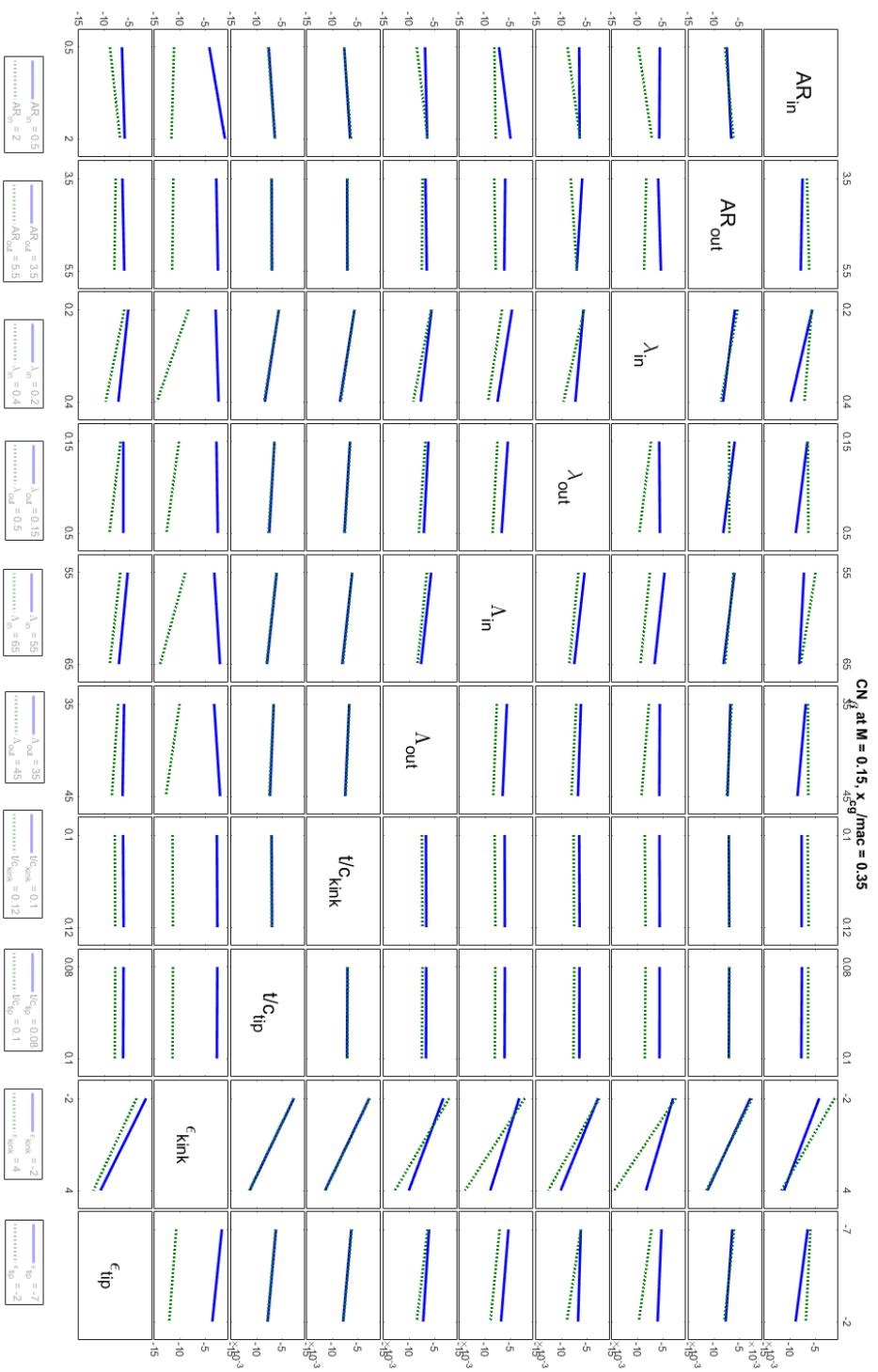

Figure 3.51: DoE interaction plot of the Yaw Moment Coefficient gradient respect angle of sideslip ($C_{\mathcal{N}_\beta}$) for the second Design of Experiments at $x_{\text{cg}}/\text{mac} = 0.35$ $M = 0.15$. MATLAB.

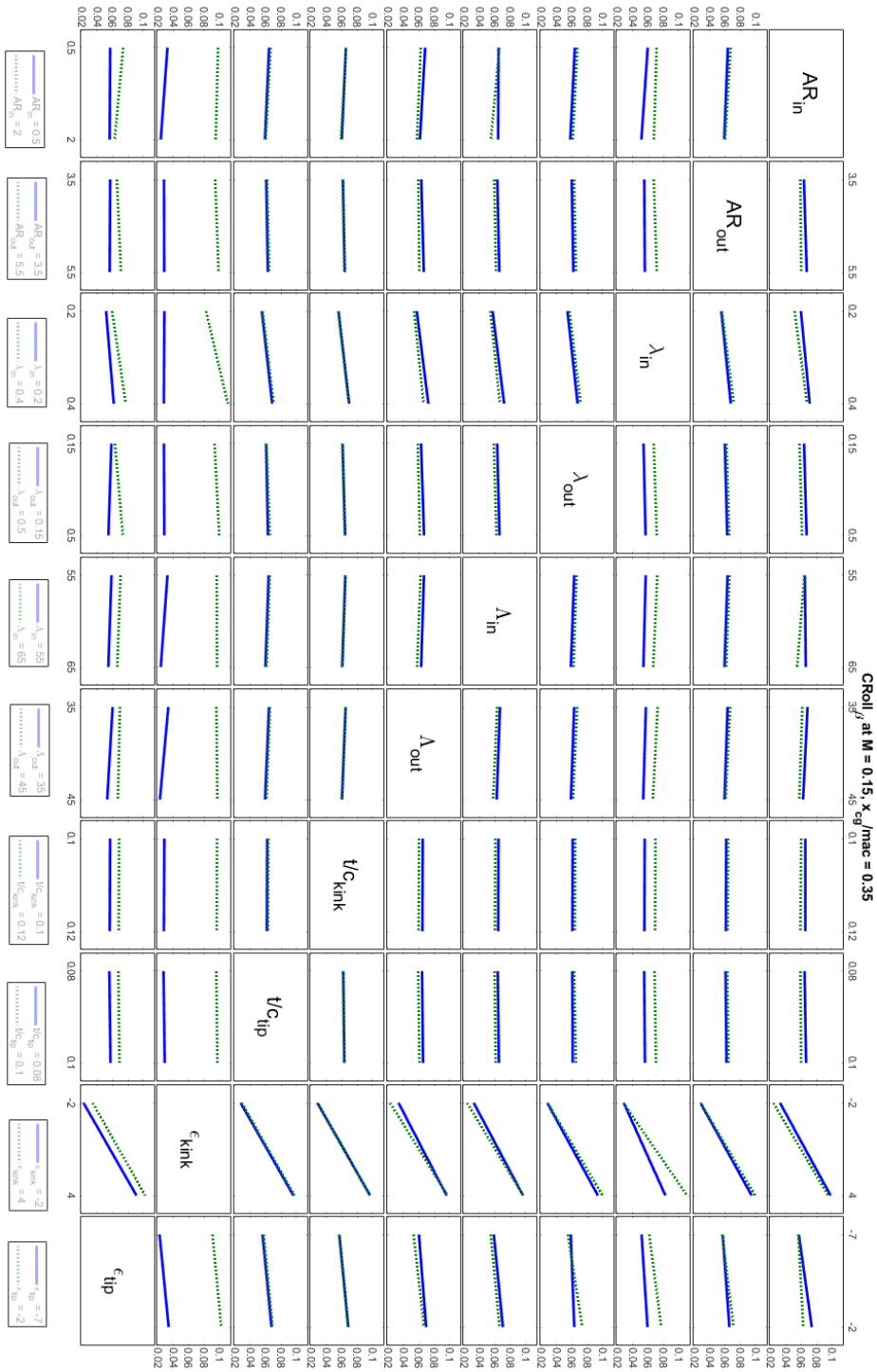

Figure 3.52: DoE interaction plot of the Roll Moment Coefficient gradient respect angle of sideslip ($C_{\mathcal{L}_\beta}$) for the second Design of Experiments at $x_{cg}/\text{mac} = 0.35$ $M = 0.15$. MATLAB.

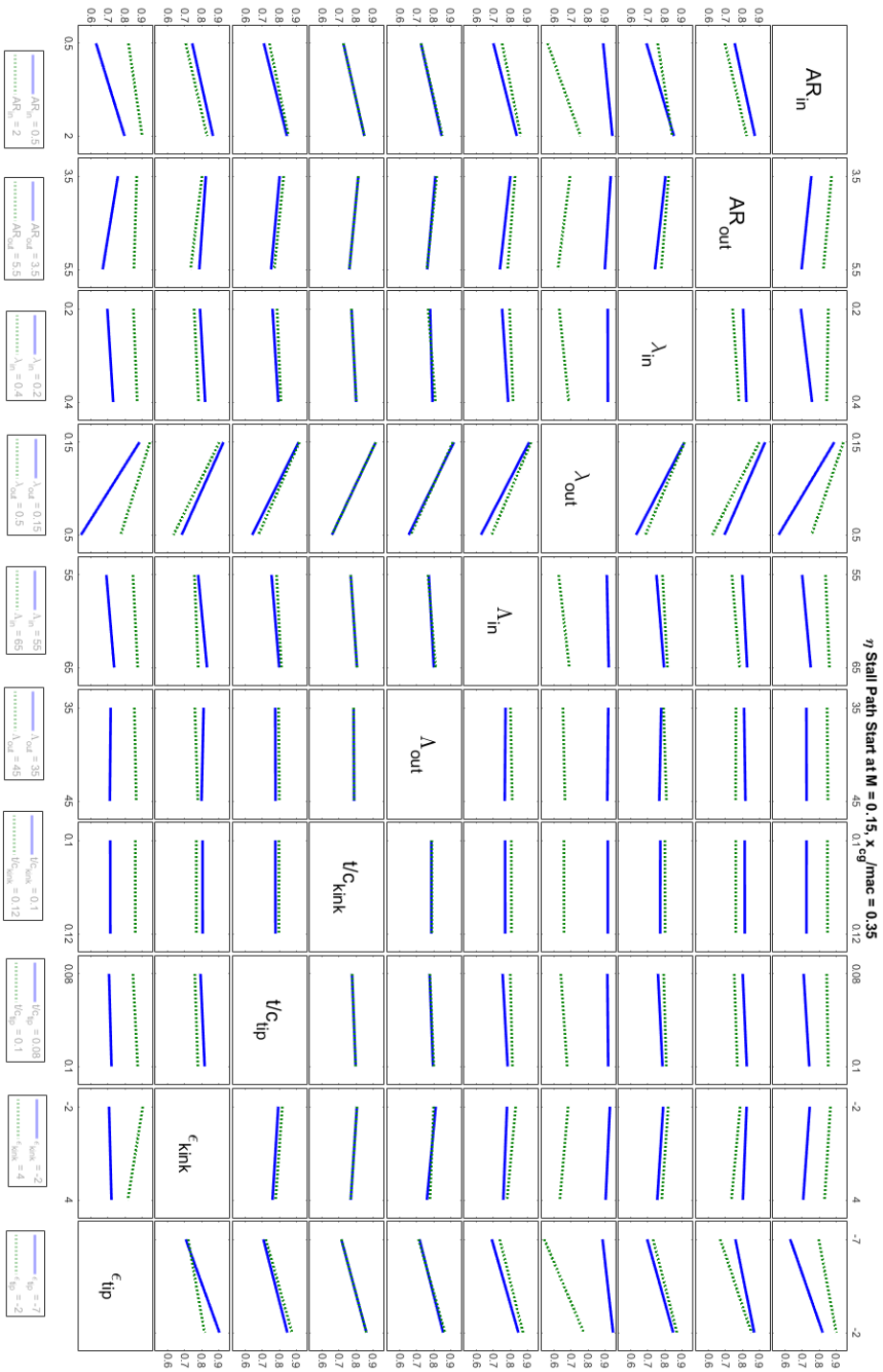

Figure 3.53: DoE interaction plot of the Stall Path section location along the span (η_{SP}) for the second Design of Experiments at $x_{\mathrm{cg}}/\mathrm{mac} = 0.35$ $M = 0.15$. MATLAB.

4
Conclusions

4.1 Results summary

This thesis work was aimed at presenting the research work carried out by the candidate in developing an algorithm for the generation of various BWB geometry planform. In Chapter 1 a general overview on the BWB concept was made, with its most important specifications, positive and negative factors.

In Chapter 2 all the information about the most important BWB projects were gathered in order to obtain a design sweep which generates a series of combinations suitable for a preliminary project phase. The designed algorithm, made in a MATLAB [18] workspace, implements OpenVSP [17] and VSPAERO software in order to generate the geometry planform of each combination yield by the design sweep and subsequently makes a preliminary aerodynamic analysis, which inputs are easily changeable in the algorithm interface.

Finally in Chapter 3 thanks to further algorithm aimed for a DoE post-processing phase, all the results were shown, both for a high subsonic and a low speed regime. The various DoE interaction plots show all the input interaction for a chosen response. The most important result relies in identifying interactions with great relevance, allowing the algorithm user to focus only on a restricted set of input specification, discarding all to specification that not affect a certain responses. Consequently that permits to establish a smaller design sweep, made with only

the most important specification, in which the analysis can be made in lesser time or the specification values can be expanded.

4.2 Future developments

Once the possibility of a static stability for the aircraft was inspected in this thesis work, the first future development is aimed towards the controllability for the BWB. The algorithm has to be expanded in order to take in consideration all the movable surfaces and their effects, starting from the allocation along the external BWB planform to the various rotation excursion. With the implementation of the movable surfaces it will be also important to prove all the results in a trimmed condition, in particular if the aerodynamic efficiency E value can be high as shown in Chapter 3. Then it will be suitable to make use of a FEM (Finite Element Method) model and a CFD (Computational Fluid Dynamics) analysis in order to have an higher degree of fidelity towards reality.

Bibliography

[1] Liebeck RH. Design of the blended wing body subsonic transport. *J Aircraft 2004;41(1):10–25.*

[2] Langley Research Center. Blended Wing Body – A potential new aircraft design: `https://www.nasa.gov/centers/langley/news/factsheets/FS-2003-11-81-LaRC.html`.

[3] Green JE. Greener by design-the technology challenge. *The Aeronautical Journal, Volume 106, Issue 1056, pp. 57 - 113*, February 2002.

[4] P.Roysdon and K.Mahmood. Lateral-directional stability investigation of a blended-wing body. *in: 10th AIAA Aviation Technology, Integration and Operation Conference*, 2010.

[5] R.Martinez-Val, E.Pérez, P.Alfaro, and J.Pérez. Conceptual design of a medium size flying wing. *Proc. Inst. Mech. Eng. Part G: J. Aerosp. Eng. 221(1) 57–66*, 2007.

[6] J.Hileman, Z.Spakovszky, and M.Drela. Airframe design for silent aircraft. *AIAA Paper, pp. 1–15.*, 2007.

[7] J.Hileman, Z.Spakovszky, M.Drela, M.Sargeant, and A.Jones. Airframe design for silent fuel-efficient aircraft. *J. Aircr. 47(3) 956–969*, 2010.

[8] V. Mukhopadhyay, J. Sobieszczansky-Sobieski, I. Kosaka, G. Quinn, and G. N. Vanderplaats. Analysis, design, and optimization of non cylindrical fuselage for blended-wing-body vehicle. *In: Journal of Aircraft 41.4, pp. 925–930*, 2004.

[9] V. Mukhopadhyay. Blended wing body (bwb) fuselage structural design for weight reduction. *In: 16th AIAA/ASME/ASCE/AHS/ASC Structures, Structural Dynamics and Materials Conference. Austin, Texas, USA*, 2005.

[10] G.Hill and R.Thomas. Challenges and opportunities for noise reduction through advanced aircraft propulsion airframe integration and configurations. *In: 8th*

CEAS Workshop: Aeroacoustics of New Aircraft and Engine Configurations, Budapest, Hungary, pp.1–13., 2004.

[11] C.Hall and D.Crichton. Engine and installation configurations for a silent aircraft. *ISABE 1164*.

[12] A.Diedrich, J.Hileman, D.Tan, K.Willcox, and Z.Spakovszky. Multidisciplinary design and optimization of the silent aircraft. *In: 44th AIAA Aerospace Sciences Meeting and Exhibit, Reno, Nevada, 9–12 January,No.1323,2006, pp.1–12.*

[13] Liebeck RH, Page MA, and Rawdon BK. Blended-wing-body subsonic commercial transport. *36th aerospace sciences meeting & exhibit. Reston: AIAA*, 1998.

[14] Potsdam MA, Page AM, and Liebeck RH. Blended wing body analysis and design. *15th applied aerodynamics conference. Reston: AIAA*, 1997.

[15] Hepperle M. The VELA project [Internet]. Cologne: DLR; 2005. Available from: `https://www.dlr.de/as/en/Portaldata/5/Resources/dokumente/projekte/vela/The_VELA_Project.pdf`.

[16] Payam Dehpanaha and Amir Nejat. The aerodynamic design evaluation of a blended-wing-body configuration. *Aerospace Science and Technology*, 2015.

[17] OpenVSP *Official Website*. Avalaible from: `http://openvsp.org/`.

[18] MathWorks, MATLAB, *Official Website*. Avalaible from: `https://it.mathworks.com/products/matlab.html`.

[19] Microsoft Office Excel *Official Website*. Avalaible from: `https://www.microsoft.com/it-it/microsoft-365/excel`.

[20] Modeling for VSPAERO. Avalaible from: `http://openvsp.org/wiki/doku.php?id=vspaeromodeling`.

[21] Rob McDonald, Cal Poly and Joel Belben. Multi-Fidelity, Multi-Physics Analysis Degenerate Geometry. VSP Workshop August 8, 2013. Avalaible from: `http://openvsp.org/wiki/lib/exe/fetch.php?media=degen_geom.pdf`.

[22] Erik D. Olson. Leveraging DegenGeom for Multi-Fidelity Analysis. OpenVSP Workshop 2016 NASA Ames Research Center, August 23-25, 2016. Avalaible from: `https://nari.arc.nasa.gov/sites/default/files/attachments/OpenVSP%20Workshop%202016%20Olson.pdf`.

[23] Documentation for the OpenVSP API. Avalaible from: `http://openvsp.org/api_docs/3.19.0/`.

[24] D.R. Gunasegarama, D.J. Farnsworth, and T.T. Nguyen. Identification of critical factors affecting shrinkage porosity in permanent mold casting using numerical simulations based on design of experiments. *journal of materials processing technology 2 0 9 (2 0 0 9) 1209–1219*, March 2008.

[25] Hilton and W.F. High speed aerodynamics. *Longmans, Green & Co., London, pp. 47-49*, 1952.

[26] Grasmeyer, J.M., A. Naghshineh, Tetrault, P.-A., Grossman, B., Haftka, R.T., Kapania, R.K., Mason, W.H., Schetz, and J.A. Multidisciplinary design optimization of a strut-braced wing aircraft with tip-mounted engines. *MAD Center Report MAD 98-01-01*, January 1998.

[27] XFOIL Software. Avalaible from: `https://web.mit.edu/drela/Public/web/xfoil/`.